The Design of a Two-Element Radio Interferometer using Satellite TV Equipment

A dissertation submitted to the Department of Electrical Engineering,
University of Cape Town, in partial fulfilment of the requirements for the degree of

Master of Science in Electrical Engineering

*a*t the

University of Cape Town

by

Tauriq Latief

Supervised by :
Dr. Simon Winberg
Prof. Amit Mishra

March 16, 2021

Declaration

I know the meaning of plagiarism and declare that all the work in the document, save for that which is properly acknowledged, is my own. This dissertation has been submitted to the Turnitin module (or equivalent similarity and originality checking software) and I confirm that my supervisor has seen my report and any concerns revealed by such have been resolved with my supervisor. This dissertation is being submitted for the degree of **Master of Science** in Electrical Engineering at the University of Cape Town. This work has not been submitted before for any other degree or examination in any other university.

Signature of Author: .... Signed by candidate
University of Cape Town

Cape Town
March 16, 2021

ABSTRACT

This research presents the design of a two-element radio interferometer capable of performing complex correlation. With the development of sophisticated radio astronomy instruments, particularly in South Africa, there is a need to develop an affordable educational instrument which can be used to demonstrate the fundamental concepts of radio interferometry to university students.

The mass production of satellite TV equipment has resulted in relatively sensitive radio frequency (RF) equipment such as parabolic reflector dishes and low-noise block down-converters (LNBs) being available at significantly reduced costs. This served as the front-end of the interferometer which was used to observe the sun between 10.70 GHz - 12.75 GHz (RF). The LNB then down-converted these to an intermediate frequency (IF) between 0.95 GHz - 2.15 GHz.

The LNBs were modified to make use of a common 25 MHz reference, which ensured that the observed fringes were only as a result of the source's geometric time delay. A power detector was also designed since the adding interferometer architecture was chosen. This power detector included the Analog Devices LT 5534 power detector integrated circuit (IC) and a Teensy 3.6 microcontroller. The calibrated power detector could detect signals as weak as - 60 dBm and showed less than 21 mV error in output for input signals in the range [- 50 dBm, -30 dBm].

The modified LNBs experienced issues, in particular the presence of a spurious LO signal, which distorted initial observations of the sun. This was resolved by the design and manufacture of narrowband hairpin filters and quarter-wavelength stub filters which were used to isolate the IF band between 1.05 GHz - 1.15 GHz (corresponding RF between 10.80 GHz - 10.90 GHz). This also improved the interferometer's resolution.

A series of filter-integrated Wilkinson power dividers and branchline couplers were designed to filter and further separate signals into in-phase and quadrature-phase (I-Q) components - these were required for complex correlation. The integrated quarter-wavelength stub filter and Wilkinson power divider achieved a maximum amplitude imbalance of 0.13 dB and phase imbalance of 0.9° between output ports. The integrated quarter-wavelength stub filter and branchline coupler achieved a maximum amplitude imbalance of 0.13 dB and phase imbalance of 91.1° between output ports. These results closely agreed with the simulated performance.

First light was observed on the 5th December 2020 when the sun was successfully detected using the coherent two-element interferometer along a 1.1 m baseline. Other tests included using the observed fringe phase to verify the physical baseline. A theoretical baseline of 1.11 m was calculated for a physical baseline of 1.3 m indicating an error of less than 0.2 m. The sun's fringe frequency and amplitude was also observed for varying baselines - the sun was resolved along a 3 m baseline.

Finally, full-system observations of the sun were conducted. These included observing the sun's cosine and sine fringes, which indicated that the analogue complex correlator was operating correctly. Thus, the primary goal of this project had been fulfilled. Specifically, developing a low-cost, educational two-element radio interferometer capable of detecting the sun.

ACKNOWLEDGEMENTS

All praise is due to the Almighty.

I would like to extend a special thank you to the following people for all their support throughout this project:

- To my supervisor, Dr. Simon Winberg, thank you for all your help in obtaining this thesis topic and for your insightful guidance in the various formal academic practices.
- To my co-supervisor, Prof. Amit Mishra, thank you for your invaluable guidance throughout the various stages of the project. Your continued mentorship has greatly furthered my engineering knowledge and skills.
- I wish to thank Brendon Daniels for assisting me with soldering the various electronics involved in this project. Your craftsmanship, patience and guidance have greatly enhanced my practical skills.
- I would like to thank Dr. Stephen Paine for assisting me with the sub-system measurements and for his knowledgeable input throughout the various testing stages.
- I wish to thank Charlie Lin, Harpreet Singh, and the rest of the team from the UCT Radar Remote Sensing Group for all their help, expertise and camaraderie throughout this project.
- This research would not have been possible without the support of the National Research Foundation (NRF) and the South African Radio Astronomy Observatory (SARAO). The financial assistance of SARAO towards this research is hereby acknowledged (www.ska.ac.za).
- I would like to thank the Hoosain family for generously allowing me to use their yard to conduct my observations during the lockdown.
- To my loving parents, Suraj and Shehnaz, thank you for motivating me to pursue my postgraduate studies and for always supporting me throughout my life.
- To my wonderful sisters, Nishaat and Farhanah, thank you for always looking out for me and encouraging me along my studies. Your hard-work and dedication have been an inspiration to me.
- To my amazing best friend and partner, Zakiyyah, thank you for all your love, care, motivation, and endurance throughout my studies - I would not have been able to achieve this without your support.

Lastly, I would like to would like to express my gratitude to everyone who, no matter how small, has contributed to the success of this project.

"A hero can be anyone. Even a man doing something as simple and reassuring as putting a coat around a little boys shoulders to let him know that the world hadn't ended."
- Batman, The Dark Knight Rises

CONTENTS

LIST OF FIGURES

LIST OF TABLES

LIST OF ABBREVIATIONS

- **ADC** – Analogue-to-Digital Converter
- **ALMA** – Atacama Large Millimeter Array
- **ATP** – Acceptance Test Protocol
- **CMB** – Cosmic Microwave Background
- **COTS** – Commercial Off-The-Shelf
- **DBS** – Direct Broadcast Satellite
- **DC** – Direct Current
- **DDS** – Direct Digital Synthesiser
- **DRO** – Dielectric Resonator Oscillator
- **ECal** – Electronic Calibration
- **ENR** – Excess Noise Ratio
- **FAST** – Five-hundred-meter Aperture Spherical Telescope
- **FBW** – Fractional Bandwidth
- **GPSDO** – Global Positioning System Disciplined Oscillator
- **HartRAO** – Hartebeesthoek Radio Astronomy Observatory
- **IBT** – Itty Bitty radio Telescope
- **IC** – Integrated Circuit
- **IDE** – Integrated Development Environment
- **IF** – Intermediate Frequency
- **I-Q** – In-phase and Quadrature-phase
- **KISS** – Kapteyn Interferometer for Short-baseline Solar observations
- **LO** – Local Oscillator
- **LNB** – Low-noise Block down-converter
- **MIT** – Massachusetts Institute of Technology
- **OCXO** – Oven Controlled Crystal Oscillators
- **PCB** – Printed Circuit Board

- **PDRO** – Phase Locked Dielectric Resonator Oscillator
- **PLL** – Phase-Locked Loop
- **QFN** – Quad-Flat No-leads
- **RF** – Radio Frequency
- **RFI** – Radio Frequency Inteference
- **SARA** – Society of Amateur Radio Astronomers
- **SARAO** – South African Radio Astronomy Observatory
- **SKA** – Square Kilometer Array
- **SMD** – Surface Mounted Device
- **SNR** – Signal-to-Noise Ratio
- **SONA** – State Of the Nation Address
- **STEM** – Science, Technology, Engineering, and Mathematics
- **TV** – Television
- **VCO** – Voltage-Controlled Oscillator
- **VNA** – Vector Network Analyser
- **VSRT** – Very Small Radio Telescope
- **XTAL** – Crystal resonator

CHAPTER 1

INTRODUCTION

This thesis investigates the design and testing of a two-element radio interferometer capable of performing analogue complex correlation. The developed interferometer made use of a combination of commercial off-the-shelf (COTS) satellite television (TV) equipment and specialised printed circuit boards (PCBs). This chapter elaborates on the purpose for having developed such a system, the main objectives of this system, and an overview of the remaining chapters of this thesis.

1.1 BACKGROUND

There are many challenges facing society in various aspects such as health, education, the environment, and the economy. Examples of these include issues such as poverty, depletion of energy resources, increased unemployment and climate change. It has been found that these issues can be addressed by effective investment in science-education and technology [16]. The field of astronomy and its need for highly sensitive instrumentation and superior computing have been a driving factor in technological advancements. These advancements have later been utilised by other sectors such as the medical and energy sectors.

In the 2019 State of the Nation Address (SONA), President Cyril Ramaphosa emphasised the importance of effective investment in science-education and technology, and how the development of the MeerKAT radio telescope has contributed to South Africa's capabilities in space observation and engineering [17]. Additionally, these contributions extend beyond the sciences and contribute to economic growth and sustainable employment.

The field of astronomy allows us to transcend our earth-bound thinking and appreciate the magnificence of the universe. Furthermore, it encourages transcontinental scientific collaborations among various institutes through projects such as the Square Kilometre Array (SKA).

The SKA is a global project aimed at developing one of the world's largest radio telescope, which will be used for imaging and exploration of the universe [18]. It will require expertise from both the scientific and engineering fields over the coming decades, thus it is important to encourage students to pursue careers in these fields, particularly in South Africa, as majority of the SKA infrastructure will be located in Australia and South Africa.

Astronomy can also have a long term benefit if correctly implemented at an educational level. Astronomy can overcome traditional teaching methods and allow students to better engage with content. An example of such an alternative approach would be to allow students to observe the sky with various optical/ radio instrumentation. This allows teaching to physically extend beyond the classroom.

Allowing students to engage in astronomy may also help them in better understanding content taught in other subjects, due to the complex nature of astronomy and its affiliation with mathematics, chemistry and physics. The alternative teaching methods have been found to encourage students to pursue careers in science, technology, engineering and mathematics (STEM) [19].

(a) Five-hundred-meter Aperture Spherical Radio Telescope (FAST), China [20].

(b) MeerKAT Radio Telescope, South Africa [18].

Figure 1.1: Examples of professional radio astronomy observatories.

Considering the aforementioned factors, and the growth of radio astronomy in South Africa, there is a need to develop a hands-on, educational tool for young students which demonstrates both the scientific and engineering aspects of radio astronomy, specifically radio interferometry. In order to minimise educational and economic boundaries, this tool should be inexpensive to replicate and should encourage the repurpose of existing equipment.

1.2 PROBLEM DESCRIPTION

There are various professional radio astronomical observatories across the world which utilise state of the art receivers typically spanning over large areas. Depending on its operation, these observatories may make use of a single antenna such as the Five-hundred-meter Aperture Spherical Radio Telescope (FAST), located in China. It is currently the largest single dish radio telescope in the world [20] with a diameter of 500 m, as per Figure 1.1a. Other observatories may instead use multiple antennas such as MeerKAT (precursor to the SKA) located in South Africa, which currently makes use of sixty-four antennas, each with a diameter of 13.5 m and a a maximum baseline separation distance of 8 km [18], as per Figure 1.1b. These observatories are expensive to construct, require large space, and are located in remote areas. Thus, are not easily accessible to students interested in radio astronomy.

Replicating such facilities, even on a small-scale, may not be feasible due to the need for highly sensitive and expensive radio frequency (RF) equipment. However, the development of satellite TV has led to the availability of moderately sensitive, yet inexpensive RF equipment being suitable alternatives for radio astronomy demonstration purposes. Repurposing satellite TV equipment for amateur radio astronomy observations grew in popularity when satellite TV switched from C-band (3.7 GHz - 4.2 GHz) to X/ Ku-band (10.7 GHz - 12.5 GHz). This widespread change encouraged amateur radio enthusiasts to find creative ways of repurposing large, now redundant, C-band reflector dishes.

There has also been a significant decline in satellite TV users; instead, many users switched to online internet streaming services for a greater variety of content. USA-based satellite TV company, AT&T reported that it had lost in excess of one million satellite TV subscribers but had gained over four-hundred thousand online subscribers in 2018 [21]. This suggests greater availability of smaller, sensitive equipment at further reduced costs, which justifies amateur experimentation with X/ Ku-band equipment.

1.3 FOCUS

The system design revolved around the repurposing and modification of satellite TV equipment such that it was suitable for radio interferometry. Focus was placed on an analogue design as majority of the components were easily available and inexpensive. Furthermore, the various stages of an RF receiver were palpable with analogue RF components whereas this is not the case for a fully/majority digital system. This is an important aspect as the system will be used as an educational tool. With regard to correlation, the radio interferometer was designed to perform complex correlation using the adding (add and square) technique.

1.4 OBJECTIVES

The main goal of this project was to develop a two-element radio interferometer using satellite TV equipment. An important objective was to maintain coherency between the two elements to ensure that the complex correlation was valid.

The interferometer was used for astronomical observations, in particular performing a drift scan of the sun. High-level outputs of the strength of the correlation are required such as graphs and voltmeter readings. As complex correlation was performed, these output requirements applied to both the in-phase (I) and quadrature (Q) outputs of the complex correlation.

1.5 METHODOLOGY OVERVIEW

The system design followed a spiral approach as it provided constant, gradual improvement in performance. The focal stages of the methodology are listed below:

- Modifying of satellite TV equipment to accept an external 25 MHz reference signal.
- Development of suitable power detectors.
- Filtering and separation of signals into I-Q components.
- Performing complex correlation with an adding interferometer.

1.6 SCOPE AND LIMITATIONS

This project focused on the design and implementation of a two element interferometer which made use of satellite TV equipment. This included its modification and the additional RF stages required to obtain the I-Q outputs of the correlation. No further modifications were done to the satellite TV equipment, besides obtaining coherency.

The main tests involved monitoring the sun's fringe pattern during drift-scans observation. These were performed at X/Ku-band while C-band will not be explored. Advanced interferometry techniques such as delay-tracking and imaging are beyond the scope of this project.

The lead-time, cost of components, and Covid-19 pandemic placed limitations on the project development as these resulted in delays and further limited performance/ improvement.

1.7 PLAN OF DEVELOPMENT

This dissertation is comprised of nine chapters which elaborate on existing literature in the field of radio interferometry, the system methodology and design, as well as the various testing stages involved. A brief summary of the remaining chapters is listed below. These are further depicted in the block diagram shown in Figure 1.3 which also links the various chapters of this dissertation.

Chapter 2 presents a literature review of the basic concepts of radio astronomy and interferometry - these assisted in better understanding the purpose of interferometry and the need to develop such a system. It includes an in-depth analysis of the adding and multiplying interferometer architectures, along with their respective benefits and output characteristics. This is then followed by a discussion regarding satellite TV equipment, in particular the function and operation of the low-noise block down-converter (LNB). Thereafter, a few amateur radio astronomy instruments are presented, in particular, instruments comprised of repurposed satellite TV equipment.

Chapter 3 provides an in-depth analysis of the user requirements and corresponding set of functional requirements and test cases. Two crucial user requirements were identified at the beginning of the project:

1. The user requires a two-element radio interferometer capable of detecting and observing the sun's fringes.

2. The developed radio interferometer should perform analogue complex correlation to produce the cosine and sine output fringes.

Another important aspect was that the designed system should largely make use of satellite TV equipment, which would encourage replication and further development by students. Thereafter, the chapter discusses the various constraints faced throughout the project such as cost and time. Finally, it elaborates on the various design stages which ensured gradual but continuous improvement of the system, from a simple single-dish system to a complete coherent radio interferometer capable of performing complex correlation.

Chapters 4 discusses the testing of existing satellite TV equipment - specifically observing how these devices operated and what their limitations were. This assisted in determining what changes needed to be made and what additional components needed to be designed. The chapter also describes how a wire antenna and RF signal generator transmitting a 10.85 GHz signal was used to investigate the LNB's down-converting architecture.

Thereafter, the chapter discusses how the LNBs' internal 25 MHz references were replaced by a common reference to achieve coherency among interferometer elements. This is followed by the design of a suitable RF power detector which fulfilled the squaring requirement of the adding interferometer. Lastly, it discusses the initial observations of the sun - this includes single-dish and interferometer observations. The initial coherent interferometer was unable to detect the sun's fringes due to issues attributed to the LNB modifications.

Chapters 5 describes how the LNB issues presented in Chapter 4 were resolved through the design of additional intermediate frequency (IF) filters, power dividers and quadrature hybrid couplers. Furthermore, two architectures were investigated to separate the LNBs' signals into its I-Q components, namely, a superheterodyne architecture, and a direct separation architecture.

Due to import restrictions, similar components could not be procured from overseas vendor. Instead, these PCBs were manufactured locally. Attention was also placed on having multiple structures integrated onto a single PCB to overcome issues such as amplitude and phase imbalance, as well as to minimise loss. Furthermore, the designed structures are compared to equivalent COTS available from Mini-circuits to evaluate their overall performance.

Chapter 6 focuses on the measurements of the manufactured PCBs initially presented in Chapter 5. These measured results are further compared to their simulated results to assess how well the initial specifications were met. The filtered modified LNBs response is also presented to determine whether the issues discussed in Chapter 4 have been resolved. The results presented in this chapter further indicate that I-Q separation of signals required for analogue complex correlation can be achieved using the manufactured PCBs shown in Figure 1.2.

Chapter 7 describes the testing of the improved coherent two-element radio interferometer. This includes the first successful observations of the sun along a 1.1 m baseline. It further discusses how issues attributed to radio frequency interference (RFI) have been resolved in later drift-scan observations. Other test results presented include observing the changes in fringe output attributed to baseline variation.

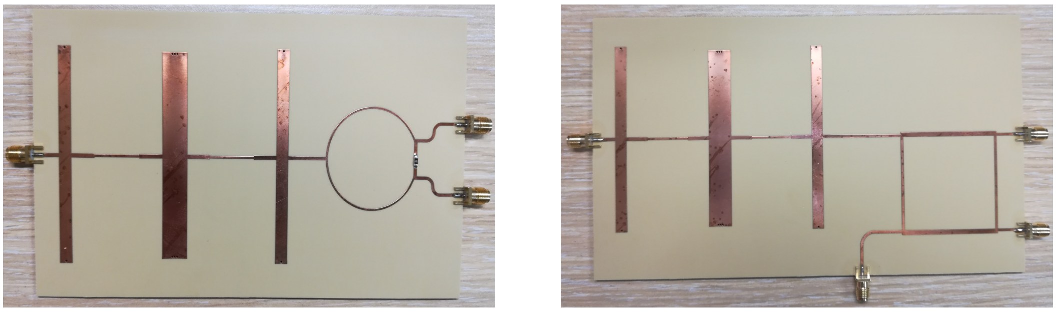

(a) Integrated filter and Wilkinson power divider

(b) Integrated filter and branchline coupler.

Figure 1.2: Manufactured integrated PCBs suited for separating the LNBs' IF signals into I-Q components.

This chapter also presents the hot-cold load tests which were performed in an effort to determine the receiver and system temperatures. Lastly, the chapter describes the testing of the complete system capable of performing complex correlation - in particular, it presents the sun's cosine and sine fringes, which were observed along varying baselines.

Chapter 8 provides a comprehensive summary of the work and the various project stages involved - including how issues relating to the initial interferometer were resolved and how signals were separated into I-Q components. This chapter also presents conclusions based on the extent to which the user requirements were fulfilled. This was evaluated using the criteria initially outlined in Chapter 3.

Chapter 9 being the last chapter in this thesis presents a guideline for future development of this and other similar systems. This includes exploring alternative analogue interferometer techniques compared to the adding interferometer implemented in this project.

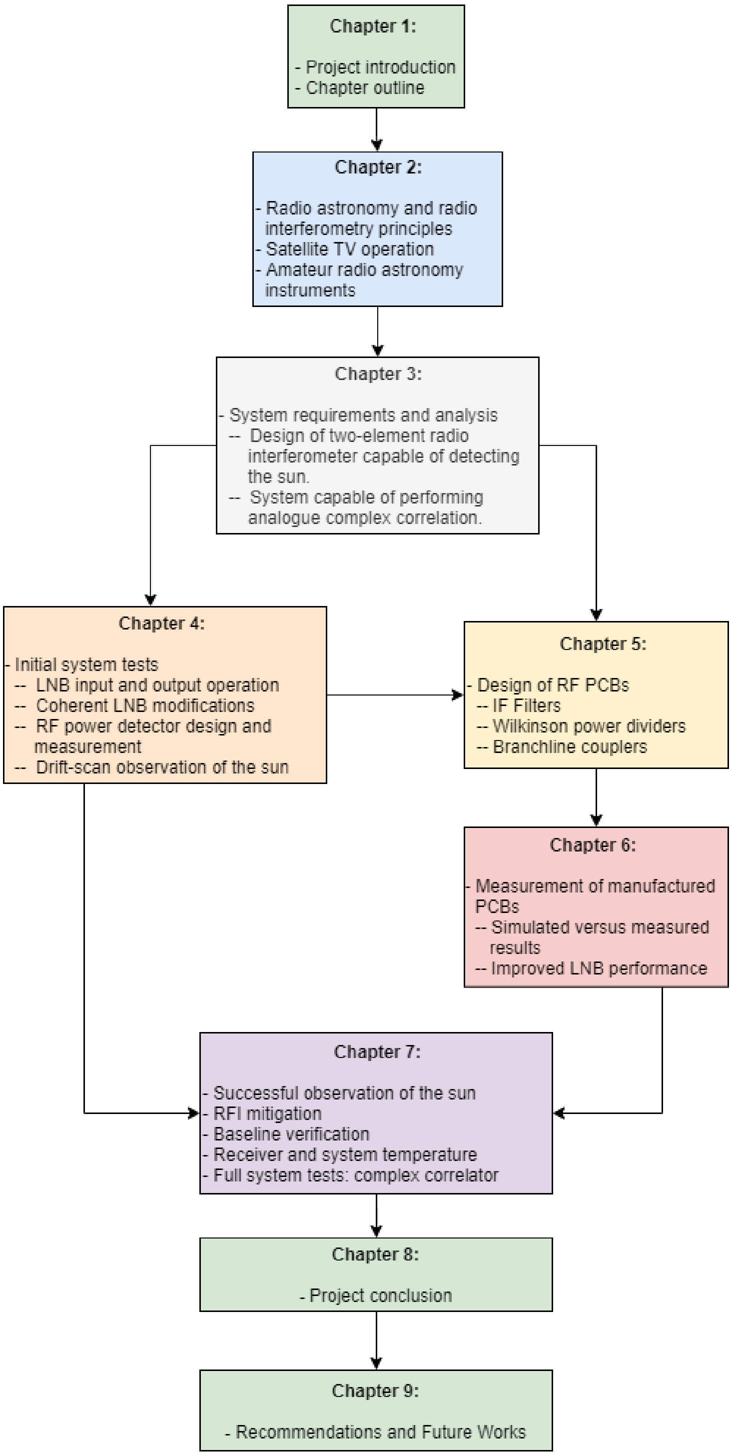

Figure 1.3: Chapter overview

CHAPTER 2

RADIO ASTRONOMY AND INTERFEROMETRY

The designed two-element interferometer will be used for astronomical observations. As such, a better understanding of the fundamental concepts of radio astronomy and interferometry is needed; this chapter presents a review of these underlying concepts. Thereafter, this chapter discusses satellite TV equipment and the modifications implemented by the amateur radio community. The chapter then concludes with a discussion of a few amateur radio and radio astronomy instruments which utilised satellite TV equipment.

2.1 CONCEPTS OF RADIO ASTRONOMY

The first radio astronomical observation was a serendipitous discovery made by engineer, Karl G. Jansky, in the early 1930s. At the time, Jansky was working at Bell Telephone Laboratories and was assigned the task of investigating the source of static interference in their communication systems [22].

Jansky investigated this by developing the merry-go-round antenna shown in Figure 2.1. He discovered that the noise was partially attributed to thunderstorms. Along with this was as an unknown ”steady hiss” sound which recurred every 23 hours and 56 minutes i.e. one sidereal day. This led him to believe that the source was extraterrestrial and determined that it originated from the centre of the Milky Way galaxy [1]. Jansky is honoured by having the unit of flux density named after him - this will be discussed later in this chapter.

2.1.1 Emission Mechanisms in Radio Astronomy

Prior to discussing the mathematical equations involved, it may be more advantageous to initially discuss the emission processes and spectra commonly observed in radio astronomy. These processes are important as they influence the architecture and sensitivity of the instrument. The two main emission types are spectral line and continuum emissions.

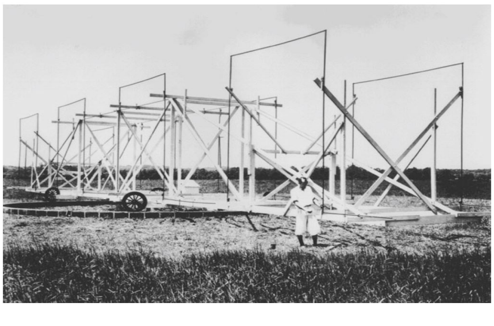

Figure 2.1: Karl G. Jansky’s merry-go-round antenna [1].

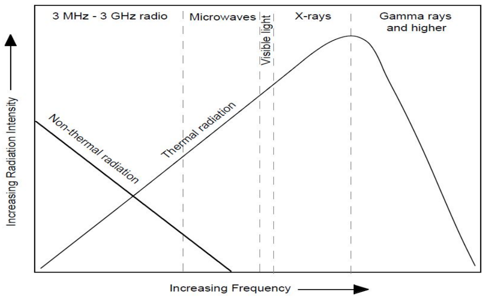

Figure 2.2: Comparison of the spectral brightness behaviour for thermal and non-thermal emission [2]. Non-thermal emission shows a decrease in brightness as frequency increases, while thermal emission increases with frequency (until it reaches its peak). Furthermore, cosmic sources may be thermal, non-thermal, or a combination of these.

The receiver sensitivity is dependent on bandwidth, as will be depicted by the various mathematical equations to follow. Furthermore a cosmic source may radiate over a wide band of frequencies or over a very narrow band. Thus, there needs to be an agreement between the receiver and source bandwidths.

Spectral line radiation is as a result of an atom or molecule's electrons transitioning from a high energy level to a low energy level. In doing so, the atom radiates a discrete amount of energy equivalent to the difference in energy levels which is consequently emitted at a specific frequency [23]. One of the popularly observed spectral line sources is neutral atomic hydrogen at 1.420 GHz. Observing spectral line emissions, particularly at frequencies above 10 GHz, requires high selectivity which may be challenging to achieve using analogue amateur instruments. Instead, focus will be placed on observing continuum sources.

Continuum sources are cosmic sources for which the radiated power gradually changes with frequency [5]. These typically occur over a wide frequency range due to the acceleration of electrons which are from a continuous distribution of energy levels [23]. Continuum emissions are further sub-classified as thermal or non-thermal emission, where for certain sources, it may be a combination of both.

The measured spectral brightness is important in classifying a source's radiation as a function of frequency. The spectral brightness of thermal emission is proportional to frequency (until it reaches a peak), while the spectral brightness of non-thermal emission is inversely proportional to frequency [2]. This difference in behaviour is evident in figure 2.2.

2.1.1.1 ***Thermal Radiation***

The underlying basis of thermal radiation is that the emission is dependent on temperature. All matter at temperatures above absolute zero radiates electromagnetic energy. This radiation is as a result of electrons continuously accelerating. The electrons in warmer sources are constantly colliding, thus continuously accelerating. Thus, the greater the source temperature, the more it radiates [2]. In addition to this, the amount of thermal radiation at a given temperature differs with frequency.

Blackbody Radiation Objects above absolute zero both radiate and absorb electromagnetic radiation. The ideal object capable of absorbing all the incident radiation (across all frequencies) is known as a perfect blackbody [24]. Consequently, the object will radiate a continuous spectra related to its temperature, hence the term, blackbody radiation.

The amount of radiation due to the presence of blackbody increases proportionally to temperature until it peaks. The frequency at which there is a peak in radiation, shifts (increases) as temperature increases. The brightness of a blackbody is governed by Planck's radiation law per 2.1, and is further depicted in Figure 2.3.

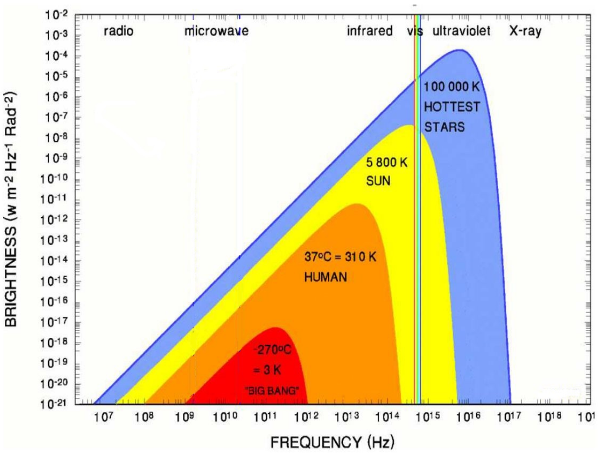

Figure 2.3: The spectral brightness versus frequency of different blackbody temperatures [3]; this shows that at a given frequency, a blackbody at a higher temperature is brighter than one with a lower temperature.

$$B = \frac{2hf^3}{c^2}\frac{1}{e^{\frac{hf}{kT}} - 1} \tag{2.1}$$

Where the constants and variables are as follows:

B:	Spectral Brightness	$(\mathrm{Wm}^{-2}\mathrm{Hz}^{-1}\mathrm{rad}^{-2}$
h:	Planck's Constant	$(6.63\mathrm{x}10^{-3}\mathrm{J.s}^{-1})$
f:	Frequency	(Hz)
c:	Speed of Light	$(3\mathrm{x}10^{8}\ \mathrm{m.s}^{-1})$
k:	Boltzman's constant	$(1.38\mathrm{x}10^{-23}\ \mathrm{J.K}^{-1})$
T:	Physical Temperature	(K)

2.1.1.2 *Non-thermal Emission*

The radiation attributed to non-thermal emissions are not dependent on the physical temperature of a source and instead rely on factors such as magnetic field strength [2], such as synchrotron radiation.

Synchroton Radiation

Synchrotron radiation results from high-energy electrons (travelling at the speed of light) moving through a magnetic field [5]. This results in electrons spiralling around the magnetic field lines. Consequently this accelerating motion of electrons produce electromagnetic radiation. Furthermore, the radiation attributed to this forms a continuous spectra as there is a continuous distribution of electron energies interacting with the magnetic field.

2.1.2 Observing Radio Astronomical Sources

With brief discussion of the different types of radio emissions completed, focus is now shifted to a simplified view of the different astronomical quantities involved during observations. This will then link to the electrical measurements obtained using instruments.

2.1.2.1 *Brightness and Power*

The concept of spectral brightness introduced in the previous section refers to the power emitted per unit area per unit frequency per unit of solid angle subtended by a source, which is required for radio astronomical imaging [5]. For a perfect blackbody, this is given by Planck's radiation law 2.1. Typically this brightness peak is well beyond the operating frequency of a radio telescope. Given this along with the operating temperature, the assumption that

$hv << kT$ can be made [24]. For a given free space wavelength, λ, this simplifies the brightness-temperature relationship in 2.1 to 2.2, known as the Rayleigh-Jeans law.

$$B = \frac{2kT}{\lambda^2} \tag{2.2}$$

The brightness is then linearly proportional to temperature. The power per unit bandwidth, ω (W.Hz^{-1}), received at the antenna is obtained by integrating the source's weighted brightness over the solid angle subtended by the source, Ω_s is given by 2.3.

$$w = \frac{1}{2} A_e \iint_{\Omega_s} B\left(\theta, \phi\right) P_n\left(\theta, \phi\right)\, d\Omega \tag{2.3}$$

Where A$_e$ is the effective aperture area of the antenna and the brightness, B(θ, ϕ), is weighted by the antenna beam pattern, P$_n$ (θ, ϕ). Note that both the brightness and power pattern may both vary with angle. The factor of half assumes that the radio receiver is capable of only receiving in one polarization, while the source is assumed to be unpolarised, hence only of half of the power per unit bandiwdth is obtained [24]. Thus it is more accurate to refer to this as the power per unit bandwidth per polarization.

2.1.2.2 ***Equivalent Blackbody Temperature***

Planck's law simplifies the process of determining a blackbody's brightness from its temperature. Furthermore, if the blackbody brightness at a single frequency is known, it can be used to determine its temperature and, thereafter, the entire blackbody spectra can be determined through the use of 2.1 and 2.2.

However, if the spectra is either partially or completely comprised of non-thermal emission, then it would be inaccurate to reference a brightness measurement to a blackbody temperature. Instead this is referred to as an *equivalent* blackbody temperature, T_E [12].

The measured brightness at a particular frequency is applied to 2.2 to calculate the equivalent blackbody temperature. However, as the source is not a blackbody, this temperature is only applicable to the single frequency at which the brightness was measured and cannot be used to classify the brightness over the remaining spectrum.

Thus, for thermal emissions, the temperature obtained refers to the physical temperature of a source, while for non-thermal sources the temperature obtained refers to an equivalent blackbody temperature.

2.1.2.3 ***Source and Observed Flux Density***

Integrating the brightness over the source solid angle yields the source flux density, S, as shown in 2.4. It is measured in W.m^{-2}Hz^{-1} or Jansky (Jy) in honour of Karl Jansky, where 1 Jy = 10^{-26}W.m^{-2}Hz^{-1} [3].

$$S = \iint_{\Omega_s} B\left(\theta, \phi\right)\, d\Omega \tag{2.4}$$

Since the brightness is related to temperature as per 2.1 and 2.2, the source flux density can be determined using 2.5.

$$S = \frac{2k}{\lambda^2} \iint_{\Omega_s} T\left(\theta, \phi\right)\, d\Omega \tag{2.5}$$

For the special case where the brightness remains uniform over the source solid angle, in particular if the temperature is uniform, then the source flux density is simplified per 2.6.

$$S = \frac{2kT\Omega_s}{\lambda^2} \tag{2.6}$$

However, the antenna measures the source's observed flux density, S_o, which is weighted by the P_n according to 2.7. The source flux density is related to the observed flux density by a correction factor, K_s, which accounts for the source size relative to the beam size such that $S = K_s S_o$. It can be assumed that the beam pattern remains constant if the source extent is small (also assuming that the source is at the centre of the beam, $P_n(\theta, \phi) \approx 1$), then 2.7 simplifies to 2.4 [3].

$$S_o = \iint_{\Omega_s} B(\theta, \phi)\, P_n(\theta, \phi)\; d\Omega \tag{2.7}$$

Furthermore, the observed flux density at the antenna can be attributed to the antenna temperature, T_A, and antenna solid angle, Ω_A. Incorporating this into 2.6 yields 2.8. Thus, the source flux density can be determined if the antenna temperature and solid angle are known/ measurable when observing a source.

$$S = \frac{2kT_A\Omega_A}{\lambda^2} \tag{2.8}$$

2.1.2.4 Antenna Temperature and Flux Density

As previously discussed, the source brightness is related to either a physical or equivalent temperature, however, this does not translate to the physical temperature of the radio antenna. Thus a relationship between the antenna measurement and the source characteristics need to be established. One way of doing this is via the antenna temperature, T_A.

The noise power per unit bandwidth, w, generated by an ideal resistor at a physical temperature, T, is known as Nyquist or Johnson noise [25] given by $w = kT$. The benefit of observing at radio frequency is that the cosmic signals received by the antenna resembles this noise. Specifically, the power per unit bandwidth at the output of a matched antenna in a noisy environment has the same characteristics as a noisy resistor. Thus, it is common practice to reference the noise power output of an antenna to that of a resistor. The antenna temperature refers to the physical temperature at which an ideal resistor would need to be held at in order to produce the same noise power as the antenna.

Using this allows the observed power attributed to a source as per 2.3 to be equated to the noise power of a resistor and consequently the antenna temperature, which is shown in 2.9.

$$w = \frac{1}{2}A_e \iint_{\Omega_s} B(\theta, \phi)\, P_n(\theta, \phi)\; d\Omega = kT_A \tag{2.9}$$

This shows that the antenna temperature is related to observed source flux density (lefthand term in 2.9). Thus, the source flux density can be determined by applying the measured antenna temperature and correction factor to 2.10 [3]:

$$S = \frac{2kT_A K_S}{A_e} \tag{2.10}$$

The antenna solid angle, Ω_A is based on the antenna area at a given wavelength and main beam efficiency, ϵ_m, specifically, $\Omega_A = \lambda^2/A$ [24]. For the special case in which the source extent is small ($K_S = 1$), the source brightness temperature, T_b (physical or equivalent depending on the emission) can be determined from the antenna temperature using 2.11.

$$T_b = \frac{\Omega_A T_A}{\Omega_s \epsilon_m} \tag{2.11}$$

2.1.2.5 *Summary of Concepts of Radio Astronomy*

This section commenced with a discussion of the different source spectra and emission mechanisms involved, followed by a discussion of how cosmic signals can be compared to receiver noise. Finally, it discussed how source properties such as its flux density and brightness can be determined by measuring the antenna's temperature along with the known antenna properties.

2.2 RADIO INTERFEROMETRY

The Arceibo radio observatory, located in Puerto Rico, was the largest single antenna radio telescope with a diameter of 305 m until it was superseded by FAST (diameter of 500 m) in 2016 [26]. The desire to build larger radio telescopes is motivated by the need to obtain a finer resolution to observe smaller source. The approximate resolution of a single antenna is $\theta \propto \frac{\lambda}{d}$, where d is the diameter of the dish. Therefore, to obtain a finer resolution at radio wavelengths requires constructing of large radio telescopes. However, there are limitations in doing this, such as space constraints, accuracy in pointing the antenna, as well as the vast expenses involved. An alternative to this is interferometry which strategically combines the outputs of multiple antennas to improve the resolution.

An interferometer makes use of multiple smaller antennas, known as elements, which are separated by varying distances, known as baselines. This improves the resolution to approximately $\theta \propto \frac{\lambda}{b}$, where b is the maximum baseline between individual elements [27].

Early interferometric techniques date back to the 1890s where it was investigated by Michelson and Pease [5] who used two spaced optical elements in order to achieve finer resolution. This technique was later adapted to the radio regime by Ryle and Vonberg in 1946 who made use of two dipole antenna arrays operating at 175 MHz separated by a maximum baseline of 240 m [28]. This has since vastly developed and has encouraged the construction of large interferometers, such as the Atacama Large Millimeter Array (ALMA), which has 66 elements (each with a maximum diameter of 12 m) separated up to 14 km away from each other [5].

2.2.1 Basics of Radio Interferometry

The basic concepts of interferometry can be understood by examining a two-element interferometer over an east-west baseline, while observing a distant source, as shown in Figure 2.4. The source is assumed to be in the far-field such that the received emissions are plane waves. Furthermore, the source is treated as a point source such that it lies in a single plane [5]. For the initial derivations it is assumed that source is quasi-monochromatic (i.e. emits over a very narrow band centred on, f_0). The effects of a larger finite bandwidth will be discussed further on.

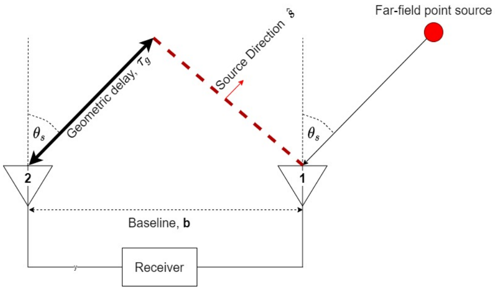

Figure 2.4: Basic layout of a two-element interferometer when observing a distant point source at angle θ_s relative to the interferometer. Source emissions arrive at antenna 2 τ_g seconds later compared to the arrival at antenna 1 - this geometric delay results from the baseline separation, b.

It is assumed that a source is in the far right of Figure 2.4. The plane wave (dotted red line in Figure 2.4) first arrives at antenna 1 (right) and as it is treated as being quasi-monochromatic. The electric field attributed to the source induces a voltage at the antenna terminals which takes an almost sinusoidal form:

$$V_1 = V\sin(2\pi f_0 t) \tag{2.12}$$

The same voltage signal is available at antenna 2 (left), however, is delayed due to the baseline separation. This is known as the geometric time delay (thick black arrow in Figure 2.4), τ_g. The voltage at antenna 2 is thus:

$$V_2 = V\sin(2\pi f_0(t-\tau_g)) \tag{2.13}$$

Considering that the signal travels at the speed of light, c, from the source to the antenna, the geometric time delay can be derived from the configuration shown in Figure 2.4:

$$\tau_g = \frac{\overrightarrow{b}\cdot\hat{\mathbf{s}}}{c} \tag{2.14a}$$

$$\tau_g = \frac{b\sin\theta_s}{c} \tag{2.14b}$$

The signals are then strategically combined at the receiver depending on the interferometry architecture being implemented. The two most common analogue approaches are the adding interferometer and multiplying interferometer.

2.2.2 System Temperature and Sensitivity

It is important to discuss the concept of a receiver's sensitivity as the desired cosmic signals resemble the noise generated by the receiver electronics. In the context of this report, noise refers to any unwanted signals (internal or external to the receiver) which may worsen the system sensitivity and conceal the desired cosmic signals (referred to as signals). Typically, these signals are much weaker than the noise and great effort is put into reducing noise in professional instruments. This section discusses the various internal and external noise sources, the system temperature, as well as the sensitivity of the adding and multiplying interferometer.

2.2.2.1 System Temperature

Section 2.1.2.4 discussed how the signal power is related to a physical or equivalent temperature; similarly, the noise can be related to an equivalent temperature. The combined signal and noise temperatures form the system temperature, T_{sys}, which determines the receiver sensitivity as per $T_{sys} = T_A + T_R$, where T_A is the antenna temperature and T_R is the receiver temperature.

Antenna Temperature Composition
A temperature is attributed to the contribution by antenna, T_A, which comprises of noise contributions such as remnants from the big bang, namely, the cosmic microwave background noise (CMB). It has a blackbody spectrum corresponding to a temperature T_{CMB} of 2.73 K in almost all directions (nearly isotropic characteristic) [1]. Other contributions include radiation from water vapour in the atmosphere, T_{WV} and radiation from the ground, T_g entering via the antenna sidelobes. An approximate value of T_A is obtained by summing of all these cosmic and noise sources as per $T_A = T_{CMB} + T_{WV} + T_g$.

Receiver Temperature Composition
The receiver noise temperature, T_R, is attributed to the noise generated by the cascade of electronics found between the individual antennas and the central detector circuitry (such as the add and square circuitry or multiplying circuitry). Among others, these electronics serve the purpose of isolating (filtering) the desired band of signals,

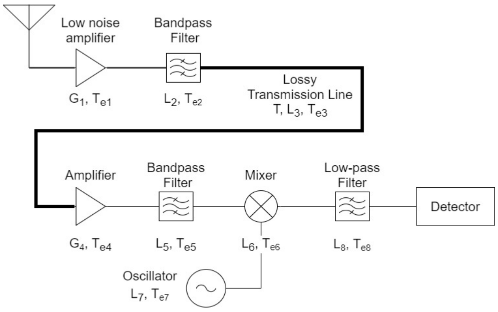

Figure 2.5: Typical cascade of receiver electronics for a single antenna receiver. Typically, components except the central detector would be replicated if it was extended to a two-element interferometer.

shifting the band down to a lower centre frequency for further processing, as well as amplifying signals to sufficient levels, as per Figure 2.5.

The components shown in Figure 2.5 have corresponding gains, G and equivalent temperature, T_e. Typically, these components' datasheets provide a noise figure, NF, measured in dB instead of an equivalent temperature. The noise figure describes the degradation of a signal as it moves through a component due to the additional noise the component introduces into the system. Specifically, it is the ratio of the signal-to-noise ratio (SNR) at the output of a component relative to the SNR at the input [14]. For a component at room temperature, $T_0 = 290K$, the conversion from noise figure to equivalent temperature is $T_e = (10^{NF(dB)/10} - 1)T_0$.

It has been shown in [14] that the receiver temperature of a cascade of N components, such as that shown in Figure 2.5, can be determined as per:

$$T_R = T_{e1} + \frac{T_{e2}}{G_1} + \frac{T_{e3}}{G_1 G_2} + ... \frac{T_{eN}}{G_1 G_2 .. G_{N-1}} \tag{2.15}$$

This shows that the first component in the receiver chain dominates the overall receiver temperature. Typically, the receiver chain commences with a low-noise amplifier to keep the overall receiver temperature as low as possible with noisy components only placed further along the receiver chain.

Certain components may be lossy which introduces more noise and further raises the cascaded receiver temperature. The equivalent temperature of a lossy component at physical temperature, T, with loss, L is given $T_e = (L - 1)T$. This is particularly of concern when using long lengths of lossy transmission line to connect a remote antenna to a receiver. Thus, the overall design should promote the use of short, low-loss transmission lines, and ensure sufficient amplification before the transmission lines.

2.2.2.2 *Sensitivity*

The receiver sensitivity determines the minimum detectable signal. Due to the noise-like behaviour of the signal it was important to first define the various temperatures present at the input of the receiver before defining its (receiver) sensitivity.

A radiometer is used for measuring the power of an incoming signal, the simplest example being a total power receiver. Since the signal into the radiometer resembles noise, the output of the radiometer will fluctuate. The minimum change in temperature, ΔT_{min}, detectable by a radiometer observing a finite bandwidth, ΔB and averaging over a finite integration time, τ, is derived in [24] and the final outcome is as per 2.16

$$\Delta T_{min} = K_{sen} \frac{T_{sys}}{\sqrt{\Delta B \tau}} \tag{2.16}$$

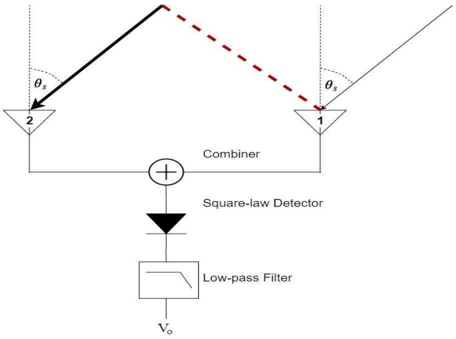

Figure 2.6: Basic layout of a two element adding interferometer.

The result shown in 2.16 is known as the ideal radiometer equation. K_{sen} is the sensitivity constant of the receiver; for the simple total power radiometer, $K_{sen} = 1$. The discussion in [3] suggest that the weakest detectable cosmic signal, ΔT of a simple radiometer is not simply $\Delta T = \Delta T_{min}$, but is greater due to factors such as gain variation. Instead, [3] suggests that realistically $\Delta T = 3\Delta T_{min}$, while [1] suggest that the weakest detectable cosmic signal is $\Delta T = 5\Delta T_{min}$.

The ideal radiometer equation is used to determine the sensitivity of the adding and multiplying interferometer as certain aspects of their operation can be derived from the total power radiometer. These interferometers sensitivity will thus correspond to different values of K_{sen} and will be discussed in their respective sections.

2.2.3 Adding Interferometer

The first radio interferometer investigated by Ryle and Vonberg was the adding interferometer [28]. Due to its simple configuration, it is commonly referred to as a simple interferometer, as shown in Figure 2.6.

The individual element voltages, V_1 and V_2 are added using a combiner and thereafter squared using a square-law detector. The output voltage of the square-law detector is thus $V_o = V^2[\sin(2\pi f_0 t) + \sin(2\pi f_0(t - \tau_g))]^2$:

The detector output voltage is proportional to power as a result of its square-law behaviour. Time averaging is done using a low-pass filter to remove high frequency terms containing multiples of $f_0 t$. The corresponding output power, P, given in 2.17 is proportional to the power of a single antenna, P_0, and is a function of the geometric time delay. The geometric time delay varies slowly as the earth rotates and θ_s, changes, thus terms including $f_0\tau$ are not removed by the filter [5]. The cosine term in the output of the adding interferometer is related to the blackbody temperature [28] and consequently the observed brightness of the source for a given baseline.

$$P = P_0[1 + \cos(2\pi f_0 \tau_g)] \tag{2.17a}$$

$$P = P_0\left[1 + \cos\left(\frac{2\pi f_0 b \sin\theta_s}{c}\right)\right] \tag{2.17b}$$

2.2.3.1 Susceptibility to Noise and Sensitivity

The signal from each antenna passes through its own chain of electrical components such as, amplifiers, mixers, and filters, before the add and square process. The chains introduces additive noise, which degrades the overall performance. This section discusses the adding interferometer's noise as well as its sensitivity.

Susceptibility to Noise
Even though the chains may have the same components and sequence, the chains' noise are uncorrelated. The signals reaching the combiner per 2.18 can be modelled as having a source component, V, and their individual

receiver chain noise, V_{RN}.

$$V_1 = V + V_{R1} \tag{2.18a}$$

$$V_2 = V + V_{R2} \tag{2.18b}$$

The output of the combiner and square law detector is thus:

$$(V_1 + V_2)^2 = V_1^2 + 2V_1V_2 + V_2^2 \tag{2.19a}$$

$$(V_1 + V_2)^2 = 4V^2 + V_{R1}^2 + V_{R2}^2 + 4V.V_{R1} + 4V.V_{R2} + V_{R1}V_{R2} \tag{2.19b}$$

Since the chains' noise are uncorrelated to the source and one another, terms in 2.19b such as $4V.V_{R1}$ and $V_{R1}V_{R2}$ are uncorrelated. By time-averaging over longer than a single period ($T = \frac{1}{f_0}$), these terms reduce to zero. The time-averaged output in 2.20 includes $4V^2$, which represents the desired correlation of the source signal received by both elements.

$$\langle V_1.V_2 \rangle = 4V^2 + V_{R1}^2 + V_{R2}^2 \tag{2.20}$$

However, the final output also includes the time-averaged noise introduced by the chain of receiver electronics. The effect of this noise is also evident in the output power and is represented by the constant term in 2.17.

Sensitivity
The adding interferometer resembles the simple total power radiometer (introduced in Section 2.2.2.2) since the combined signals are input into a power detector, thus it shares the same minimum detectable temperature repeated here for convenience:

$$\Delta T_{min} = \frac{T_{sys}}{\sqrt{\Delta B \tau}} \tag{2.21}$$

The total power receiver output, and consequently the adding interferometer output, are directly proportional to the total receiver gain, G; thus if the gain is not constant, its fluctuations, ΔG, will undesirably contribute to the fluctuations in the output voltage which may incorrectly be regarded as a signal [1]. The gain fluctuation thus raise the overall realistic minimum detectable temperature according to:

$$\Delta T_{min} = T_{sys} \sqrt{\left[\frac{1}{\Delta B \tau} + \left(\frac{\Delta G}{G} \right)^2 \right]} \tag{2.22}$$

This justifies the discussion in [1] and [3] which suggest that the realistic minimum detectable source temperature is three to five times greater than the minimum temperature in 2.21. The consequence of this is that it limits the maximum gain that can be added to the receiver.

2.2.4 Multiplying Interferometer

Modern interferometers overcome the limitations of the adding interferometer by instead using a digital correlator. The digitised element signals are effectively multiplied together and time averaged to reduce the effects of noise. The time-averaged output is the correlation between the two elements.

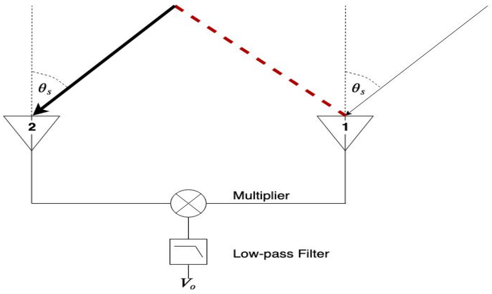

Figure 2.7: Basic layout of a two element multiplying interferometer. The elements' signals and noises are multiplied. By time averaging, any uncorrelated signal-noise products are removed, which reduces the effects of the receiver noise.

One of the first analogue implementations of this was the phase-switching interferometer developed by Ryle in 1952 [29]. It used a similar architecture as the adding interferometer, but periodically switched one element's signal between 0° and 180° relative to the other element's before adding and squaring. The square-law output, thus, switched between the sum-squared and difference-squared. An additional synchronous detector took the difference between these two outputs and the final time-averaged output was proportional to the product of the elements' signals [5]. This effectively removed the individual elements' noise contributions, which aided in designing longer baselines.

There are challenges involved in implementing a phase-switching interferometer for amateur purposes such as accurately switching a band of frequencies (instead of single frequency) between 0° and 180°. This technique also requires a switch signal generator for periodically switching the phase of the element and the later synchronous detection. As such, the phase-switching interferometer will not further be considered for this design.

An alternative way of obtaining a similarly appealing output, is through the use of a multiplying interferometer. From an analogue perspective, this multiplying action is achieved using a mixer as per Figure 2.7. The output of the mixer is then time averaged using a low-pass filter.

Similar to the adding interferometer, the multiplying interferometer can be analysed using the individual monochromatic signals V_1 and V_2 from 2.12 and 2.13, respectively. The multiplier effectively multiplies these signals to produce:

$$V_1 V_2 = V^2 \sin(2\pi f_0 t) \sin[2\pi f_0 (t - \tau_g)] \tag{2.23a}$$

$$V_1 V_2 = V^2 [\sin^2(t) \cos(\tau_g) + \cos(t) \sin(\tau_g) \sin(t)] \tag{2.23b}$$

Time averaging reduces $\sin^2(2\pi f_0 t) = \frac{1}{2}$, while the $\cos(2\pi f_0 t)$ and $\sin(2\pi f_0 t)$ reduce to zero. However, since the $\cos(2\pi f_0 \tau_g)$ term varies slower than these terms, it does not simplify to zero. Thus, time averaging can be seen as removing the higher frequency terms, which is typically achieved using a low-pass filter as per Figure 2.7. The output after the low-pass filter simplifies to:

$$V_o = \frac{V^2}{2} \cos(2\pi f_0 \tau_g) \tag{2.24}$$

2.2.4.1 Susceptibility to Noise and Sensitivity

The adding interferometer suffered from additional receiver noise as well gain fluctuations which were particularly evident in 2.17 and 2.22. This section discusses the multiplying interferometer's susceptibility to noise as well the influence of gain.

Susceptibility to Noise

The influence of noise in the adding interferometer was better analysed using the simplified signals in 2.18. Similarly, it can be applied to the multiplying interferometer according to:

$$V_1.V_2 = V^2 + V.V_{R1} + V.V_{R_2} + V_{R_1}V_{R_2} \tag{2.25}$$

The uncorrelated terms are removed after sufficient time-averaging and the output consists of only the correlation of the source signal received by both elements as per 2.26. The multiplying architecture is therefore less susceptible to receiver noise and gain fluctuations when compared to the adding architecture.

$$\langle V_1.V_2\rangle = V^2 \tag{2.26}$$

Sensitivity

The ideal radiometer equation of a single antenna receiver from 2.16 serves as basis for determining the minimum temperature detectable by a two-element interferometer as the square-law operation resmebles a correlator which multiplies two identical signals [1]. However, where the square-law detector output includes the noise contribution from each of the receivers, the correlator (multiplying interferometer) output only includes contribution from the source being observed. This is due to the noise in each of the receivers being uncorrelated to one another. The sensitivity of a multiplying interferometer shown in 2.27 shows an increase in sensitivity as the number of elements, N, increases.

$$\Delta T_{min} = \frac{T_{sys}}{\sqrt{N(N-1)\Delta B\tau}} \tag{2.27}$$

Thus, the sensitivity of a two-element multiplying interferometer is $\sqrt{2}$ more sensitive than the adding interferometer (assuming no gain fluctuations are present in the adding interferometer). The minimum detectable flux density, ΔS, can be determined by applying the minimum detectable temperature, ΔT, to 2.10. The ideal radiometer using a single antenna will have a minimum detectable flux density of:

$$\Delta S = \frac{2k}{A_e}\frac{T_{sys}}{\sqrt{\Delta B\tau}} \tag{2.28}$$

Whereas a two-element multiplying interferometer will have a minimum flux density shown in 2.29, which $\sqrt{2}$ better than a single antenna.

$$\Delta S = \frac{kT_{sys}}{A_e\sqrt{2\Delta B\tau}} \tag{2.29}$$

Combining the result in 2.27 with 2.10 importantly shows that for large values of N, the term $\sqrt{N[N-1]} \to N$. Thus, for large values of N, the sensitivity of the multiplying interferometer comprised of N elements each with effective area, A_e, will tend to the sensitivity of a large antenna with an effective area NA_e; the derivation of this can be found in [1, 24]. This substantiates the need to have more elements in professional systems.

2.2.5 Fringes and Visibility

One of the advantages of large interferometers is their ability image minute cosmic sources. This is possible by varying baselines and relating the signal observed by the interferometer to the source brightness. The task of imaging is well beyond the scope of this project, however, a few of the underlying principles are introduced here to justify the significance of the previously discussed interferometer outputs. A more in-depth analysis of these topics can be found in [1, 5].

2.2.5.1 *Interferometer Fringes*

The source being observed in Figure 2.4 moves across the sky due to the earth's rotation and the source angle relative to the interferometer changes accordingly. The sinusoidal outputs of the the adding and multiplying interferometer, referred to as fringes, with the fringe phase, ϕ, dependent on θ_s [1] as per:

$$\phi = 2\pi\tau_g \tag{2.30a}$$

$$\phi = \frac{2\pi b\cos\theta}{c} \tag{2.30b}$$

The fringe period, $d\phi$, as a function of angular shift, $d\theta_s$ is given by 2.31 [1]. This can be rewritten as a function of time by noting that the angle varies in time as a result of the earth's rotations ($\omega_e = 7.29 * 10^{-5}$ rad.s^{-1} is the earth's sidereal rate - this is known as the fringe frequency given by 2.32.

$$\frac{d\phi}{d\theta_s} = \frac{2\pi b\sin\theta_s}{\lambda} \tag{2.31}$$

$$\frac{d\phi}{dt} = 2\pi\omega_e\frac{b\sin\theta_s}{\lambda} \tag{2.32}$$

From a more qualitative point of view, this can be understood by considering a source moving across the interferometer's sinusoidal fringes. The sinusoidal fringes can be represented graphically as an intensity map of dark (peak) and light (trough) bands as per Figure 2.8. The output fringes are the superposition of the various peak and trough bands crossed by the source.

Figure 2.8a shows a source (star) much smaller than the spacing between two adjacent bands. There is no superposition of bands crossed by the source, thus, the output fringes are not attenuated relative to the interferometer fringes. The source is said to be unresolved [5].

When the source is similar in size to the spacing between the bands as per Figure 2.8b, the output is the superposition of the various bands crossed by the star resulting in constructive and destructive interference of the initial interferometer fringes. The source is said to be partially or completely resolved [5].

The output fringes of these two sources are shown in 2.9. The source size can be determined once the output fringes reduce to zero. This requires multiple crossing of bands with the source similar to that shown in Figure

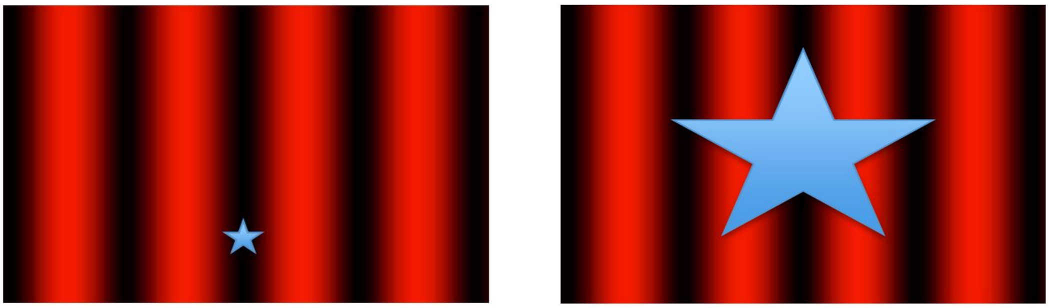

(a) Unresolved source. (b) Partially resolved source.

Figure 2.8: Interferometer fringes/ bands crossed with different source (star-shape) sizes [4]. Smaller sources (relative to the fringe spacing) are crossed by fewer/only one band and are unresolved. Larger sources are crossed by more bands allowing it to be either partially or completely resolved.

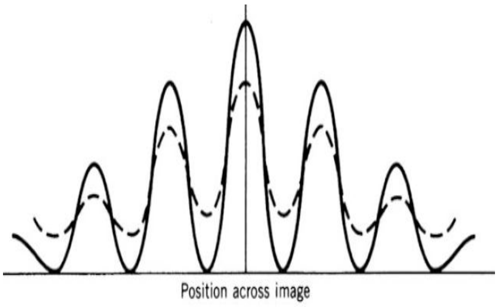

Figure 2.9: The output fringes of different source sizes for a given baseline. The solid line represents a source significantly smaller than the baseline spacing and is unresolved (Figure 2.8a), while the dotted line represents a source comparable in size to the baseline spacing and is partially resolved (Figure 2.8b) [5].

2.8b. The fringe spacing can be decreased by increasing the baseline which justifies the construction of long baseline interferometers.

2.2.5.2 ***Visibility and Brightness***

The interferometer's output (i.e. the correlation of the source signals received by the element) is known as the complex visibility, $\mathcal{V}$ and its units is W.m^{-2}.Hz^{-1}, the same as flux density [5]. A Fourier transform directly relates the complex visibility measured by the interferometer to the source brightness in the sky. This is known as the Van Cittert-Zernicke Theorem as per 2.33, which relates a cosmic source's brightness to a measurable quantity obtained by the interferometer.

$$\mathcal{V}(u,v) = \iint B(x,y)e^{j2\pi(ux+vy)}dxdy \tag{2.33a}$$

$$\mathcal{B}(u,v) = \iint V(x,y)e^{-j2\pi(ux+vy)}dudv \tag{2.33b}$$

Multiple Baselines
The sinusoidal correlator output of a two-element interferometer responds to a single angular frequencies of $\frac{b\sin\theta_s}{\lambda}$, which relates to a single Fourier component of the brightness [1]. Thus, a range of angular frequencies are required to reconstruct the brightness; this can be achieved by regularly varying the baseline of the two-element interferometer when making measurements. However, this is impractical when working with large elements.

Instead, modern interferometers comprise of multiple elements (more than two) over different baselines - these can be modelled as groups of two-element pairs. Thus, an interferometer with N elements has $\frac{N(N-1)}{2}$ two-element pairs. The output of each pair produces a unique visibility which corresponds to a specific component of the brightness [27]. Thus, more baselines allow for a better reconstruction of the source brightness and consequently improved imaging. The benefit of more elements has also previously been shown to improve the sensitivity of the multiplying interferometer.

Complex Cross-Correlation
One of the primary objectives of this project was to design a complex cross-correlator. The need for correlation has already been discussed however, the "complex" aspect has not been.

This can be understood by treating the source brightness as being the sum of its even, B_E, and odd, B_O, components such that $B = B_E + B_O$. The adding and multiplying interferometer outputs provide a cosine correlator output when observing a point source with isotropic interferometer elements. Applying this to a slighly extended source by treating it as a sum of point sources [1] with brightness distribution, $B(\hat{s})$ which yields a correlator output:

$$R_c = \iint_{\Omega_s} B(\hat{s}) \cos(2\pi f_0 \tau_g) d\Omega \tag{2.34}$$

This shows that the correlator output only responds to the even (symmetric) component of the brightness. The odd (asymmetric) component can be obtained by using a sine correlator [1]. One way of obtaining the odd component is to include an additional correlator circuit in which one of the element inputs are phase shifted by 90° since $\sin(2\pi f_0 \tau_g) = \cos(2\pi f_0 \tau_g - 90°)$, thus the sine correlator output is:

$$R_s = \iint_{\Omega_s} B(\hat{s}) \sin(2\pi f_0 \tau_g) d\Omega \tag{2.35}$$

Combined, the circuitry which obtains both these cosine and sine components is known as a complex correlator and a basic outline of its functionality is shown in Figure 2.10. Euler's formula allows a complex exponential to be written as a sum of cosine and sine terms; as the visibility is a complex value, it can be applied here. Specifically, the outputs of the complex correlator are combined to fully describe the complex visibility as per 2.36.

$$\mathcal{V} = R_c - jR_s \tag{2.36}$$

This can be written in the complex exponential form as per 2.37c comprised of an amplitude, $|\mathcal{V}|$, and phase, ϕ_v given by 2.37a and 2.37b, respectively.

$$|\mathcal{V}| = \sqrt{R_c^2 + R_s^2} \tag{2.37a}$$

$$\phi_v = \arctan(\frac{R_s}{R_c}) \tag{2.37b}$$

$$\mathcal{V} = |\mathcal{V}|e^{-j\phi_v} \tag{2.37c}$$

Similar to the earlier analysis in which the observed flux density was as a result of the brightness weighted by antenna's power pattern in 2.7, the complex visibility observed by the interferometer is weighted by the antenna's effective area in the direction of the source, $A(\hat{s})$ [5]. Thus, the complex visibility can be related to the source brightness as per 2.38.

$$\mathcal{V} = \iint A(\hat{s})B(\hat{s})e^{-j2\pi f_0 \tau_g} d\Omega \tag{2.38}$$

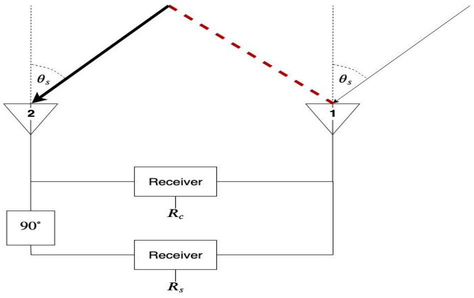

Figure 2.10: Complex correlator showing the additonal 90° phase shift and correlator circuitry required to obtain both the even and odd components of the brightness.

Thus, the above explanation justifies the need for a complex correlator to fully characterise the visibility and determine the source brightness.

2.2.5.3 ***Finite Bandwidth Effects***

The operation of the both the adding and multiplying interferometers were derived assuming a quasi-monochromatic source and a receiver perfectly centred on f_0. However, the interferometer's antennas and receiver electronics typically operate over a finite bandwidth, ΔB, centred on f_0.

This can be accounted for by integrating the behaviour of the interferometer over this finite bandwidth. If the source brightness remains constant over this band, the output further weighted by $sinc(\tau_g \Delta B)$ function [1] and the complex visibility related to the source brightness becomes:

$$\mathcal{V} = sinc(\tau_g \Delta B) \iint A(\hat{s}) B(\hat{s}) e^{-j2\pi f_0 \tau_g} d\Omega \tag{2.39}$$

As $\tau_g \Delta B << \tau_g f_0$, the interferometer output over a finite bandwidth resembles the sinusoidal fringes obtained from the quasi-monchromatic derivation, with its envelope modulated by a sinc function. For a given bandwidth and baseline, this sinc function attenuates the desired fringes and eventually produces nulls in the fringe pattern.

The effects of the sinc function can be reduced by either reducing the bandwidth and/or the geometric time delay. Reducing the bandwidth is a simpler solution, however, the interferometer sensitivity is dependent on the bandwidth as previously shown.

Instead, the interferometer in Figure 2.4 can be modified to include a compensating delay, τ_0, to remove the effects of the geometric delay and consequently the sinc function. Implementing this is challenging particularly at an analogue level since the compensating delay needs to be regularly adjusted to track the relative motion between the source and the interferometer. As such this, compensation technique will not be implemented in this project. However, this discussion has been included to justify the expected results from the two-element interferometer.

2.2.6 **Summary of Radio Interferometry**

This section focused on the fundamental concepts of radio interferometry derived from a simple two-element interferometer. These concepts include the voltages present at the outputs of each antenna and the geometric delay resulting from the spacing between elements. Thereafter it relates the different sources of noise (both internal and external to the receiver) to their respective temperatures, which determines the sensitivity.

Thereafter, this section discussed two analogue interferometer architectures, namely the adding interferometer and the multiplying interferometer, both of which were compared to a total power radiometer. The characteristics compared included their output forms, susceptibility to noise, and consequently their overall sensitivity.

As has been shown, the total power radiometer and consequently the adding interferometer is susceptible to issues such as gain fluctuations attributed to power supply stability and changes in environmental conditions - these result in a deteriorated sensitivity. The Dicke radiometer is an alternative to the total power radiometer and relies on switching between the antenna output and a known noise source [30]. This results in a minimum detectable temperature, ΔT_{min}, of twice that of the ideal total power radiometer, however, unlike the total power radiometer, the Dicke radiometer does not suffer from gain fluctuations. The effect of environmental conditions on temperature and gain further justify the need to have cooled receivers in professional instruments [31].

The concept of fringes was then introduced which was related to the typical sinusoidal outputs of an interferometer. The visibility was then discussed which is related to the source brightness, and that to fully characterise the source brightness, a complex correlator with varying baselines would be required.

2.3 SATELLITE TELEVISION

The first transatlantic televison broadcast between Europe and North American was made on 23 July 1962 using the Telestar satellite [32]. This provided viewers with a larger variety of content as well as granted access to viewers in remote/ rural areas, who had previously not had access to cable television. Since then, it has greatly developed and further been standardised, with majority of these transmissions occurring between 10.7 - 12.7 GHz.

The viewer's receiver system generally comprises of an outdooor parabolic reflector (commonly referred to as dish) and a low-noise block down-converter (LNB) which then connects to an indoor decoder. A core aspect of this project was to repurpose various commercially available satellite TV equipment for radio astronomy observations; in particular the dish and LNB. This chapter will elaborate on their operation as well as existing modifications which have been done by users.

2.3.1 Parabolic Reflectors

Repurposing satellite TV equipment grew in popularity when mainstream TV broadcast shifted from C-band (3.7 - 4.2 GHz) to X/Ku-band (10.7- 12.75 GHz - commonly only referred to as Ku-band satellite TV). This resulted in large C-band dishes, typically with diamters greater than 2 m now being obsolete. These were then repurposed for both amateur radio and amateur radio astronomy.

The shift to Ku-band, allowed a for physically smaller dish. This reduced the space needed as well as the cost of the system - this further encouraged its repurposing by amateur radio enthusiasts (discussed later in this section). The topic of dishes will be limited as the available dishes were not be modified nor were there a wide variety of brands available in South Africa.

A common supplier of satellite TV equipment in South Africa is Ellies Holdings, who sells satellite TV equipment under its Elsat brand. This includes 0.40 m and 0.75 m diameter dishes rated for Ku-band satellite TV.

2.3.2 Low-noise Block Down Converter

The LNB is a crucial, multi-functional, component in the digital broadcast satellite (DBS) TV receiver. As the name suggests, the LNB is a low-noise device which down converts the block of RF frequencies from 10.7 - 12.75 GHz down to an intermediate frequency (IF) of 0.95 - 2.15 GHz [33]. Thereafter, the IF signals are typically transmitted via coaxial cable to the decoder.

The coaxial cable not only carries the IF signal from the LNB to the decoder, but also carries a DC supply from the decoder to the LNB to provide power to the LNB electronics; the decoder also provides a tone signal to vary the LNB operation [34]. A bias tee internal to the LNB is used to separate the IF signal from the DC and tone. Figure 2.11 shows the typical layout of an LNB, while Figure 2.12 shows a dual output LNB available in South Africa [6].

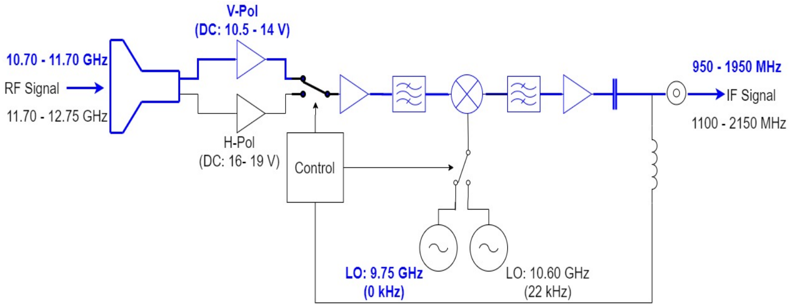

Figure 2.11: Block diagram showing the main components of the LNB. The LNB down-converts the RF signals to an IF stage which can then be transmitted via coaxial cable. The coaxial cable also carries a power and control signals to the LNB.

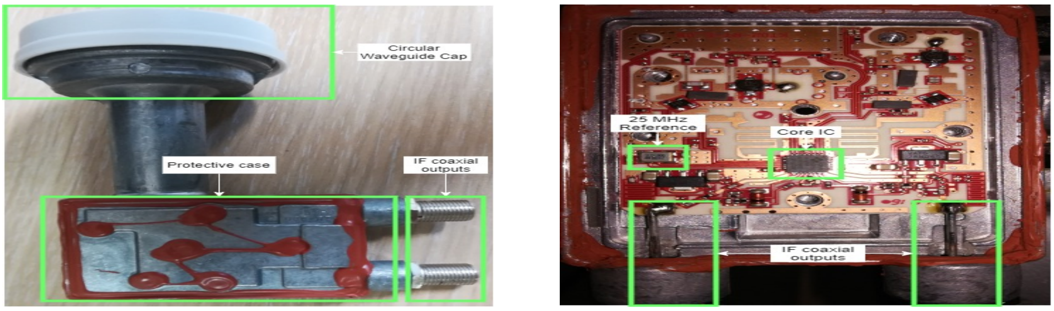

(a) LNB Metallic Enclosure

(b) LNB Electronics

Figure 2.12: Dual output Elsat LNB availabe in South Africa [6].

2.3.2.1 Waveguide, Filtering and Amplification

The circular cap shown in Figure 2.12a houses the circular waveguide located at the front of the LNB which captures the radio signals reflected by the dish. The circular waveguide is capable of receiving both vertically and horizontally polarised signals, however, only one polarisation is processed at any given instance. Typically, the polarisation depends on the voltage received from the decoder. The Elsat LNBs available in South Africa require 10.5 - 14.0 V for vertical polarisation and 16.0 - 19.0 V for horizontal polarisation [6].

Thereafter the RF signal is amplified using a low-noise amplifier which assists in reducing the devices noise figure. Due to the proprietary nature of the LNB designs, manufacturer's do not include an in-depth datasheet of the individual components. However, this LNB's overall gain is specified as 53 - 63 dB with a gain flatness of ± 0.5 dB/ 26 MHz [6].

The amplified signal is then passed to an image reject filter which has a rated minimum rejection of 40 dB. The following section elaborates on the down-conversion scheme used in the LNBs, which includes two local oscillators (LO) at 9.75 GHz and 10.6 GHz to down-convert the RF signals to 0.95 GHz - 2.15 GHz. Using 2.40 obtained from [14], the image frequency, f_{IM}, can be calculated using based on the LO frequency, f_{LO} and IF frequency, f_{IF}.

$$f_{IM} = f_{LO} - f_{IF} \tag{2.40}$$

Low-side injection ($f_{RF} > f_{LO}$) of the oscillators is used for both the 9.75 GHz and 10.6 GHz oscillators. This corresponds to an image band ranging between 7.80 GHz - 8.80 GHz, which is 1.9 GHz away from the desired RF band and should be well attenuated by its internal filter.

2.3.3 Down-conversion and Core Integrated Circuit

The desired RF band is first down-converted before transmission over the coaxial cable. This reduces cost as the cost of electronics near 1 GHz -2 GHz (IF) is notably cheaper than electronics above 10 GHz (RF). An integrated circuit (IC) is at the core of most modern LNBs which performs the core functionality of the LNB. The IC includes two voltage controlled oscillators (VCO), a phase-locked loop (PLL), mixer, and additional filtering and amplification. Popular IC manufacturers include RDA Microelectronics and Rafael Micro, with chip models differing depending on the number of LNB outputs - this includes single, dual, quad, and octo outputs. The choice depends on the number of independent decoders the LNB would need to supply.

As mentioned earlier, the LNB includes two local oscillators (LO), a low-band at 9.75 GHz and a high-band at 10.6 GHz. The PLL present in the IC is used to improve frequency stability and phase noise, and typically use a 25 MHz or 27 MHz reference quartz crystal resonator (XTAL) as per Figure 2.12b. Older LNBs used a dielectric resonator (DRO) to generate the LO frequencies [34].

The low-band LO is used to down-convert the RF band in the range of 10.7 GHz - 11.7 GHz, while the high-band down-converts the RF band in the range of 11.7 - 12.75 GHz. The tone signal supplied from the receiver to the LNB is used to switch between the two bands - a 0 kHz (i.e. no tone supplied) tone selects the low-band, while a 22 kHz tone selects the high band.

2.3.4 LNB External Reference Oscillator

Es'hailSat, a Qatar satellite company, launched its Es'hail-2 satellite into space in November 2018. Its main purpose is telecommunication and digital TV broadcast to the Middle East and Africa, but also includes an amateur radio repeater for amateur broadcast and communication [35].

This repeater broadcasts over a very narrow band centred on 10.4 GHz, which is relatively close to the lower edge of the LNB RF passband and should not necessarily be excessively attenuated. This, along with the other attractive features of the LNB such as high gain and low cost (the LNB shown in Figure 2.12 costs less than ZAR 250) has made it appealing to amateur radio enthusiasts. However, the reference XTAL suffers from frequency stability issues which is problematic when dealing with a narrow bandwidth.

A common amateur solution is to remove the XTAL and provide a more stable reference signal - this was particularly of interest to the project as a common reference needed to be supplied to both elements to ensure coherency. As previously discussed, the interferometer fringes are as a result of the geometric time delay attributed to the baseline separation. If the elements made use of separate LOs, the output fringes would be distorted/ unreliable as the fringe phase would be include an indiscernible beat frequency attributed to the difference in phase of the separate LOs. This section discusses a few examples of LNB reference modifications.

2.3.4.1 External Reference for the Octagon PLL LNB

The Octagon LNB is commonly used by radio amateurs and operates in a similar fashion as discussed above. This particular example is a dual-port output LNB with two 27 MHz references. Radio amateur G4JNT [7] desoldered one XTAL and fed in an external reference via an additional coaxial cable (a hole was also drilled into the LNB's metallic enclosure to make provision for this). The centre pin of the coaxial cable was soldered onto the initial XTAL input pad and a DC blocking capacitor (10 nF) was then fed into the RDA Microelectronics IC. A 62Ω resistor to ground was included for better matching; Figure 2.13 shows the initial and modified LNB circuitry.

A 5 dBm external reference was supplied. An AD9852 direct digital synthesiser (DDS) with a 10 MHz master reference was used as G4JNT wanted to observe the LNB performance with obscured valued references (e.g. 26.496 MHz and 28.312 MHz) - a reference between 25.64 - 32.30 MHz was sufficient to lock the PLL.

Observing an RF of 10.368 GHz with the 27.000 MHz reference (LO at 9.750 GHz) yield an IF of 618.0 MHz with output power of 8 dBm while the image was rejected by 40 dB. Furthermore, the phase noise at 2 kHz from the carrier was -72 dBc/Hz.

(a) Original

(b) Modified

Figure 2.13: Octagon LNB Modifications done by radio amateur G4JNT [7].

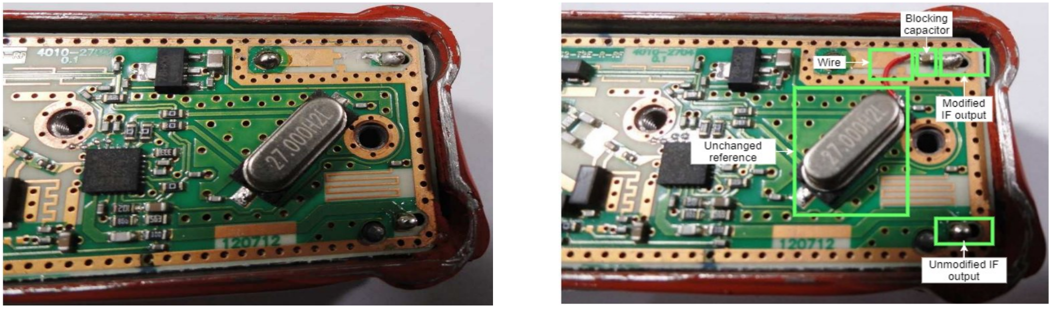

(a) Original

(b) Modified

Figure 2.14: LNB Modifications done by radio amateur DF9NP [8].

2.3.4.2 10 MHz External Reference Oscillator

The LNB was again an inexpensive solution for receiving amateur radio transmissions near 10 GHz, however, the standard LO would drift due to temperature variations, thus, a more stable reference was needed. Amateur radio enthusiast, DF9NP, addressed this by using an external PLL circuit also referenced to a 10 MHz master [8].

The dual-port LNB was used, in which one of the output coaxial ports was modified to only carry this external reference. The PCB traces connecting to the coaxial pin was disconnected by cutting/ scrapping away the traces. Thereafter a DC blocking capacitor (1 nF) along with a wire was used to connect the reference coaxial pin to the existing reference (27 MHz). Unlike the previous example in which the initial XTAL reference was removed, this design attempted to use injection-locking to obtain the desired reference - this is shown in Figure 2.14. The external PLL circuitry maintained the external VCO's 27 MHz using a 10 MHz master reference which was shown to improve stability. This master reference could be an oven-controlled crystal oscillator (OCXO) or a global positioning system disciplined oscillator (GPSDO).

2.3.4.3 LNB-based Interferometer for Sensing

The use of LNB-based, two-element interferometer was investigated in [9], due its (LNB) quoted high performance yet low cost appeal of LNBs. The main aim was to determine whether it would be feasible to use LNBs as sensors for future imaging systems. The brand of LNBs used was not mentioned, however, based on the discussion, the LNBs operated in a similar manner as discussed. The noteable difference is that the LNBs made use of two DROs instead of a PLL. To ensure coherency between the LNBs and improve phase noise , an external LO was supplied via the coaxial cable shown in Figure 2.15a; this is similar to the modification done in section 2.3.4.1.

The IC traces of one of the LOs were broken and replaced by a direct coaxial cable carrying the external 10 GHz oscillator, which was generated by a phase-locked dielectric resonator oscillator (PDRO) and a phase stable 10

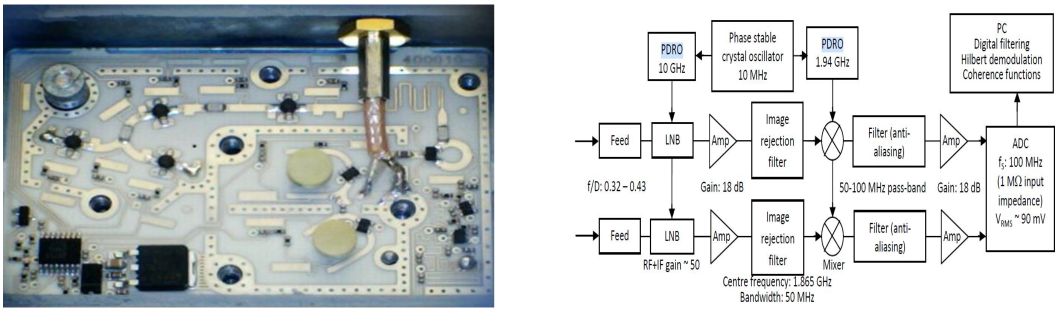

(a) LNB-based modification - the two round disks left of the coaxial cable are the original DROs.

(b) Block diagram of receiver front-end and sampling

Figure 2.15: LNB-based sensor development tested in [9].

MHz crystal oscillator (master reference). A master LO of 10 dBm yielded the lowest noise temperature. Further details of the LO generation were not provided. The RF band was centred at 11.865 GHz, which corresponded to an IF of 1.865 GHz. The output IF signal was then filtered, amplified and down-converted, after which, it was sampled and digitally correlated, as per Figure 2.15b.

The LNB noise temperature was determined using the Y-factor method and was found to range between 170 - 300 K, which was significantly larger than the quoted range of 7.5 - 23.5 K. This may be attributed to the frequency at which the LNBs were tested or the test conditions for which the manufacturer rated these LNBs. This large discrepancy is concerning as it largely influences the sensitivity of the interferometer.

2.3.5 Summary of Satellite TV

This section discussed the main components required in the reception of digital satellite TV, specifically the dishes and LNBs. Great attention was paid to the internal operations of the LNB and how the LNB control voltage/ signals can be used to adjust the LNB output. Thereafter the functioning of the central IC present in modern LNBs were discussed and how its internal PLL typically uses an XTAL reference. Finally, existing LNB modifications were discussed, particularly the adaptation to use an externally supplied reference. This is important, as this project requires coherency between LNBs, which can be achieved using a common reference signal.

2.4 AMATEUR RADIO ASTRONOMY INSTRUMENTS

The aim of this project was to design a two-element interferometer which replicates some of the fundamental features of professional interferometers such as MeerKAT and the ALMA. However, this interferometer will much less sensitive due to the equipment being used, reduced cost and significantly smaller size. Thus, focus will now be placed in analysing amateur radio astronomy instruments which have been implemented. This includes single dish receivers as well as two-element interferometers.

2.4.1 Single Dish Radio Astronomy Receiver

It is beneficial to start this discussion with amateur implementations of the single dish receiver, as many simple examples make use of the total-power detector architecture, like that found in the adding interferometer. The educational instrument developed by the Hartbeesthoek Radio Astronomy Observatory (HartRAO) is one such instrument, and in addition, made use of the conventional satellite TV dish and LNB, as discussed in [3].

Figure 2.16 shows the receiver block diagram as well the built receiver. The LNBs served to down-convert the RF signals. The sun was the main source under observation and based on the IF filter used, it (sun) was observed at an RF between 10.75 - 11.25 GHz (1.00 GHz < IF < 1.50 GHz).

The receiver was calibrated by pointing the dish toward the sky (cold load approximated as 10 K) and the ground (hot load approximated as 300 K). The calculated receiver temperature was 135 K. Other tests done with this system include measuring the sun's brightness temperature and observing the positions of geosynchronous satellites.

(a) Block Diagram

(b) Completed Receiver

Figure 2.16: Single dish, LNB-based radio astronomy receiver developed by HartRAO [3].

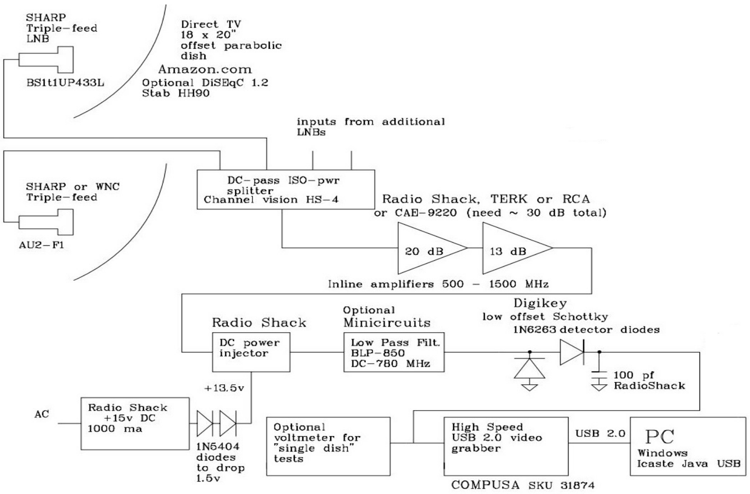

Figure 2.17: Two-element VSRT developed by MIT Haystack Observatory using Ku-band LNBs [10]. The system uses the adding technique, however, does not use a common reference between LNBs.

2.4.2 **Very Small Radio Telescope Interferometer**

The Very Small Radio Telescope (VSRT) is a two-element interferometer developed by the Massachusetts Institute of Technology (MIT) Haystack Observatory [10]. It is a well-documented guide intended for college and undergraduate student observations with an approximate cost of \$500. The resources available include the guidelines in building, testing, and performing observations with a two-element interferometer. The interferometer follows the adding principle previously discussed and makes use of Ku-band LNBs to down-convert the RF signals before adding; Figure 2.17 shows a block diagram of this system.

As can be seen in the block diagram, the LNBs do not share a common reference/ internal LO, thus lacks coherency. Furthermore, only the in-phase (cosine) component was accounted for. As a consequence of both of these attributes, the visibility is not fully recoverable with this system. Nonetheless, the fringes are still present and the power output closely follows the adding interferometer output in 2.17, however now includes a beat frequency as per $P = P_o\left[1 + cos\left(2\pi f_0 \tau_g\right) + 2\pi(v_b - v_a)t)\right]$.

The beat frequency is the difference between the LNBs' LOs (v_b and v_a) which result in slightly different IF frequencies. Thus the squared output now also varies with time, instead of only on the geometric delay. The output is then sampled using a USB video grabber (typically used to convert analogue video for digital viewing on a computer), and VSRT-developed software is used to display the observed fringes.

2.4.3 **Kapteyn Interferometer for Short Baseline Solar Observation**

The Kapteyn Interferometer for Short Baseline Solar Observation (KISS) is a two-elemenet radio interferometer developed at the University of Groningen, which makes use of satellite TV equipment [11]. Its development included the front-end dish modelling, the back-end interferometer construction, and data processing. The back-end implementation is in particular relevant as it follows a similar procedure as proposed by this thesis, particularly in modifying LNBs for radio astronomy observations.

The interferometer made use of PLL-based EVO LNBs, which are designed to use an external 25 MHz crystal. The LNB operation was tested using a wire antenna transmitted at 11.255 GHz (further details of the antenna or RF signal were omitted). The IF output showed a distinguishing peak near 1.505 GHz -this suggests a LO near 9.75 GHz which agrees with the manufacturer's data.

The standard XTAL output power was measured and found to be approximately -2 dBm under standard operation. The XTALs were then removed and a common 25 MHz reference (of equivalent power) was supplied using a

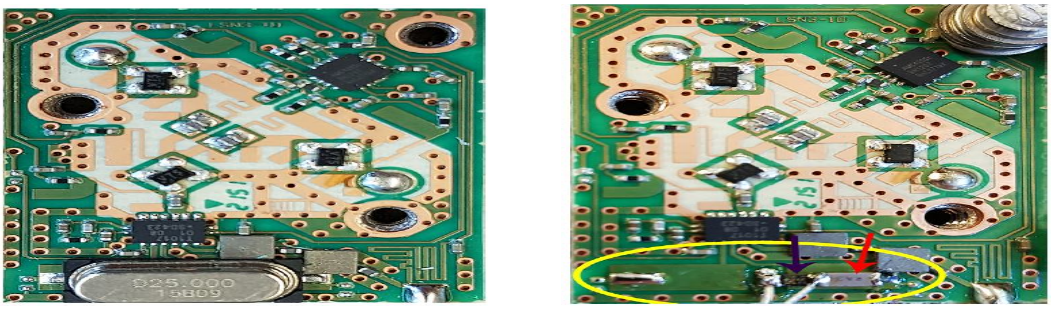

(a) Standard EVO LNB including its 25 MHz XTAL.

(b) Modified EVO LNB with the common 25 MHz reference supplied over coaxial cable. A DC blocking capacitor and 50 Ω resistor were included to block DC and improve matching, respectively.

Figure 2.18: Modifying the EVO LNB to use an externally fed reference [11].

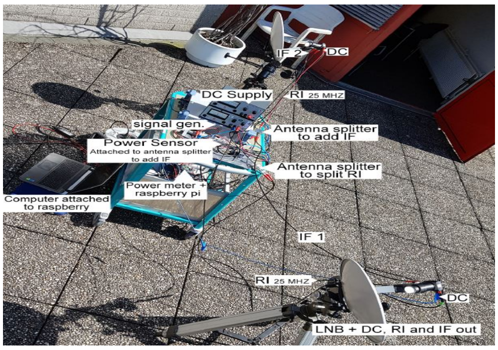

Figure 2.19: Complete setup of KISS - a two-element interferometer which makes use of coherent LNBs [11].

signal generator via a coaxial cable as per Figure 2.18b.

The modified LNBs were tested using the same wire antenna method and a distinguishing output was measured at 1.505 GHz indicating that the LNB was still functioning correctly. Similar to the previous VSRT, the KISS interferometer is an adding interferometer, which adds the signals using a commercial TV splitter (in reverse operation), however KISS is coherent. KISS performs the squaring operation using a power-meter connected to a Raspberry Pi, which continuously logs the measurements.

The KISS configuration shown in Figure 2.19 has a pre-detection bandwidth of 40 MHz (using a tunable bandpass filter), and a post-detection integration time of 40 ms. Only a portion of the LNB bandwidth was utilised to improve the system's resolution. The sun was the main astronomical source observed using KISS and successfully resolved the sun's fringes using a baseline of 2.88 m. This corresponds to an angular size of 0.54 °, which closely agrees with other literature.

2.4.4 4 GHz Correlation Radio Interferometer

In an effort to repurpose (by then obsolete) C-band satellite TV dishes, astronomer, Kenneth Tapping, explored building a two-element multiplying (correlating) interferometer [12]. The initial estimations were based on a simple radiometer suggested that a minimum sensitivity of 1 Jy was theoretically possible, however, this was unlikely to be realised due to gain instability and radio frequency interference (RFI); instead, the multiplying interferometer was chosen. C-band satellite TV also use LNBs, however, these were not used in this design due to needing a common LO for the LNBs. Instead, low-noise amplifiers with a waveguide input and N-type coaxial output were used. Two main designs were considered in which there was a trade-off between sensitivity and susceptibility to RFI - these are shown in Figure 2.20. The first design was centred at 4 GHz with a 500 MHz bandwidth, which multiplied the RF signals using a double-balanced mixer. Unlike the previous discussions which used a low-pass filter, the mixer output is filtered using a band-pass-like filter. The lower cut-off was used to remove

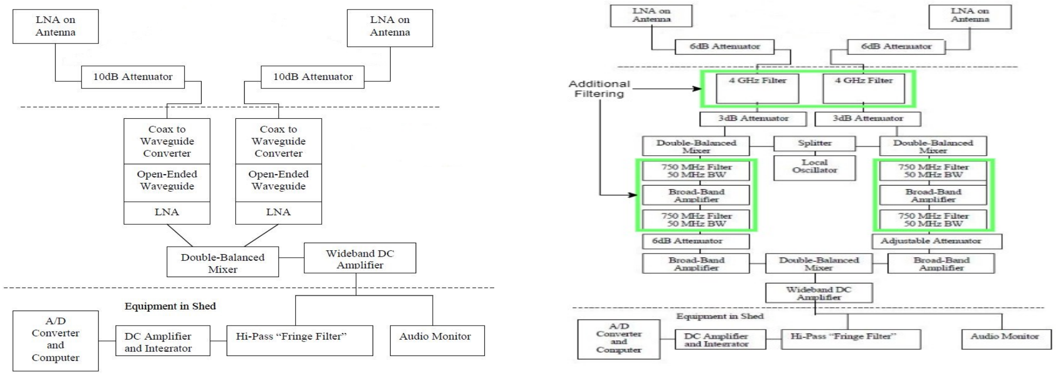

(a) Initial design with a 500 MHz bandwidth.

(b) Improved design with a 50 MHz bandwidth.

Figure 2.20: Two designs of the 4GHz Interferometer with a tradeoff between sensitivity and RFI mitigation [12].

any slow varying RFI from satellites, while the upper cut-off was used to remove higher frequency mixer products. The system temperature was approximated as 100 K yielding a 10 mK minimum detectable temperature and corresponding minimum flux density of 28 Jy. It is to be noted that external sources of noise were not considered in estimating the system temperature. Thus, the true sensitivity would be notably less.

The initial design still struggled in terms of interference due to the limited filtering. The second design instead down-converted the RF signals to 750 MHz with a 50 MHz bandwidth - this is ten-times smaller and worsens the sensitivity by a factor of 3.16. Furthermore, the additional filtering and mixing stages raised the receiver temperature, which also reduces the sensitivity. However, an estimate of this raised temperature and worsened sensitivity was not provided. Regardless of this reduced sensitivity, the new design performed better with the source fringes clearly visible. Observed sources include Cygnus A, Cassiopeia A, and Taurus A.

2.4.5 **408 MHz Cross-Correlation Radio Interferometer**

The two-element correlating interferometer was once again explored by the same author [12] as the previous example, however, with two key differences. Firstly, this interferometer used arrays of Yagi-Uda antennas (referred to as yagis) as elements, and secondly, where the previous example only produced the correlator cosine fringes, this example also produced the sine output.

Again, two designs were explored, trading between sensitivity and interference mitigation. The interferometer operated at 408 MHz with a 1 MHz bandwidth. Each element was an array of two, 14-element yagis (two yagis additively combined to form a single element), totalling to four antennas. Due to the smaller gain and bandwidth, the 408 MHz interferometer had a poorer theoretical sensitivity of 1600 Jy. A baseline of 15 m was used to observe the sun; the RF signals were filtered and down-converted to an IF at 30 MHz with a 1 MHz bandwidth (later reduced to 500 kHz for reduced RFI), and thereafter multiplied with one another, as per Figure 2.21.

Attention should be paid to the IF signals before being multiplied - each IF signal is split equally into three parts. One part is fed to a power detector (for pointing/ adjusting the system), while the remaining two feed into double-balanced mixers for the multiplication stage. Part of element 1's IF signal (Figure 2.21) is transmitted via an additional quarter-wavelength of transmission line to approximate a 90° phase-shift, while element 2 is unshifted. The cosine and sine components of their correlation can then be obtained by multiplying the shifted and unshifted components as shown in the figure. This technique used to obtain the sine component is not accurate when considering that the quarter-wavelength of transmission line corresponds to a 90° at only a single frequency, and provides limiting modelling of amplitude and phase imbalance over a given bandwidth.

2.4.6 **Summary of Radio Astronomy Instruments**

This section discussed the architecture of but a few of the amateur radio instruments which have been developed. It commenced with a discussion of a single dish radio astronomy receiver which demonstrated the basic con-

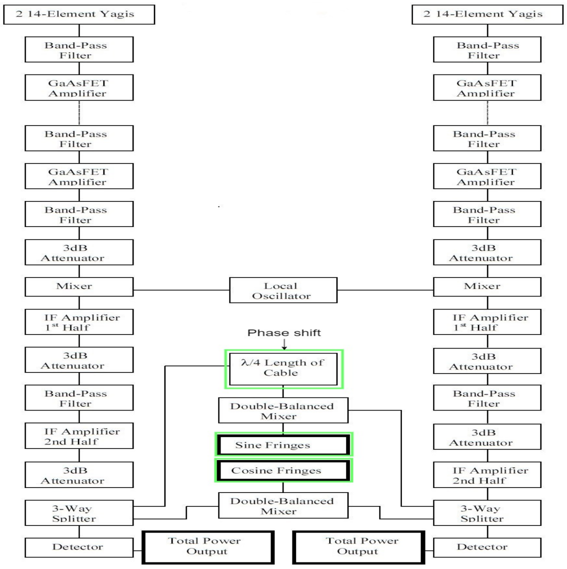

Figure 2.21: Two-element interferometer operating at 408 MHz, which produces both the cosine and sine fringes by introducing an additional 90° phase shift [12].

cepts of repurposing satellite TV equipment for radio astronomy. Thereafter, it discussed adding interferometer implementations such as the VSRT and KISS, the latter making use of coherent LNBs.

This was followed by the 4 GHz interferometer which made use of satellite TV dishes along with waveguide-to-coaxial low-noise amplifiers. This example performed the correlation using multiplication, but focused only on the cosine components. The final interferometer example produced both the cosine and sine fringes, using arrays of yagis and emulating a 90° phase-shift with a quarter-wavelength of transmission line. This concludes the section on amateur instrumentation, as well as the chapter on radio astronomy and interferometry, as a whole.

Analysis of these various amateur radio astronomy instruments have further served as a guide in determining the various components needed to develop the two-element radio interferometer. Specifically, the RF front-end would be comprised of a satellite TV dish and LNB. Thereafter, the output IF signal would require additional filtering to improve the fringe resolution and minimise interference. The filtered signal would then need to be separated into I-Q components and further strategically combined to form the I-I and I-Q pairs of the complex correlation. In-depth discussion, design, and testing of these various components and aspects are discussed in Chapters 4-6.

CHAPTER 3

REQUIREMENT ANALYSIS AND METHODOLOGY

This chapter analyses the various project requirements and commences by identifying a set of user and functional requirements. These are then used to develop a corresponding set of design requirements, along with a suitable set of acceptance test protocols (ATPs). Following this is an in-depth analysis of the project constraints.

The chapter then discusses the design methodology used - specifically the spiral model - which allowed for quicker prototyping and testing with regular improvement. The chapter then concludes with an overview of the overall system development.

3.1 USER AND FUNCTIONAL REQUIREMENTS

The core requirement of this project was to implement a simple radio interferometer to be used for amateur astronomical observations. In consideration of the continued growth of radio astronomy and interferometry in South Africa, it is imperative that the underlying principles of these sophisticated instruments be taught to the current and future generation of students - particularly in the fields of science and engineering. In this regard, factors such as being low-cost, and simple to implement were prioritised over high precision and accuracy. Bearing this in mind, the following user requirements and functional requirements were identified and are later summarised as per Table 3.1.

Analysis of R.U.01
The user requires the front-end design and implementation of a two-element radio interferometer to be used for astronomical observations.

A radio interferometer needed to be designed and built, which would comprise of the conventional front-end stages involved in the capturing and processing of the RF signals. These include the antenna and feed, as well as various stages of amplification, filtering and down-converting.

The sensitivity was limited due to sensitivity of the equipment available and the physical size of the system. The receiver front-end made use of satellite TV equipment due to its advertised low-noise properties, local availability, and relatively inexpensive price. Focus was placed on observing and resolving the sun at X/Ku band frequencies, as this equipment primarily operates between 10.7 GHz - 12.75 GHz.

An adding interferometer comprised of two-elements with an adjustable baseline was used. Resolving the sun near X/Ku band frequencies required a baseline of approximately 3 m.

Analysis of R.U.02
The system should serve as an introductory, educational tool for radio interferometry.

The main purpose of the system was to demonstrate the fundamental concepts of radio astronomy and interferometry to astronomy and engineering students. This further portrayed the advantages of interferometry over single antenna receivers as well as the typical challenges faced with interferometry.

The data captured during an observation needed to be stored. High level outputs such as intensity versus time and voltage versus time plots were also required for further student analysis.

Analysis of R.U.03
Correlation of received RF signals must be performed in the analogue domain and should encourage further development.

Instead of immediately digitising the RF signals and subsequently performing digital correlation, the individual elements' signals were correlated with one another using the analogue techniques identified in Section 2. This included the use of RF electronics such as amplifiers, filters, combiners, power dividers, and hyrbid couplers, which were required to produce the I-Q output fringes.

In furtherance of the educational aspect of the system, the configuration should encourage subsequent development and improvement, as well as be low cost. Individual stages of the system could more easily be improved by connecting discrete RF electronic components/blocks to one another. The use of discrete components also allowed for better explanation to students unfamiliar with the front-end's operation.

Analysis of R.U.04
Coherency among elements in the interferometer needs to be established.

Ideally the delay in signal between elements would be solely due to the geometric configuration and corresponding geometric time delay. In order to ensure that the correlation correctly reflects this, all heterodyne stages were performed using a common reference oscillator between the elements.

Analysis of R.U.05
Receiver electronics need to be protected against adverse weather conditions and radio frequency interference (RFI).

Certain receiver electronics were placed relatively close to the antennas to minimise losses and improve performance. As such, the electronics were exposed to various environmental effects. A housing structure was be built to store and protect these electronics. In addition to protection against adverse weather conditions, the housing also needed to protect electronics from interference.

Table 3.1: Summary of user requirements and functional requirements for the simple radio interferometer implementation.

Index	User Requirement	Index	Functional Requirement
R.U.01	Front-end design and implementation of a radio interferometer to be used for astronomical observations.	R.F.01	Observe sources such as the sun for a finite duration (drift scan).
		R.F.02	Front-end comprised of repurposed satellite TV equipment.
		R.F.03	Adjustable interferometer baseline.
R.U.02	The system should serve as an introductory, educational tool for radio interferometry.	R.F.04	Sampling and storing of observed data for further processing using a microcontroller.
		R.F.05	High level system outputs such as voltage/ power meters, and fringe curves.
R.U.03	Correlation of the received RF signals should be performed in the analogue domain and should encourage later development.	R.F.06	Analogue correlation performed using modular RF electronics.
		R.F.07	Ability to produce I-Q output fringes (complex correlation).
		R.F.08	Low-cost implementation.
R.U.04	Coherency among elements in the interferometer needs to be established.	R.F.09	Perform down-conversion with a common reference oscillator.
R.U.05	Receiver electronics need to be protected against weather and radio frequency interference (RFI).	R.F.10	Shielding and enclosure for cables and front-end electronics.

3.2 DESIGN REQUIREMENTS

Using the user and functional requirements identified in the previous section, a set of design requirements were developed and is listed in Table 3.2. As the primary source under observation would be the sun, the design specifications can be quantified based on various performance metrics, specifically for this observation. The following target specifications were outlined, based on the findings presented in Chapter 2.

- Operating RF frequency of 10.85 GHz, across a 100 MHz bandwidth (elaborated further in Chapter 4).
- Minimum detectable flux density, ΔS, of less than 500 Jy.
- Minimum radiometric resolution, ΔT, of less than 10 mK.
- Bandwidth integration time product, $\Delta B\tau$, of at least $550 * 10^6$.
- A receiver temperature, T_R, below 200 K, largely due to gain fluctuations, and inaccurate claimed LNB noise figures.

3.3 ACCEPTANCE TEST PROTOCOLS

In order to ensure that the various user, functional and design requirements were fulfilled, a set of acceptance test protocols (ATPs) had been devised which were be assessed throughout the development of the system. These ATPs are listed in Table 3.3

Table 3.2: Design requirements for the simple radio interferometer implementation.

Index	Design Requirement	Reference
R.D.01	The system will repurpose satellite TV LNBs, amplifiers, combiners, and satellite finders.	R.F.01, R.F.02, RF.06, R.F.07, RF.08
R.D.02	Specialised RF PCBs should be designed to overcome the limitations of COTS satellite TV equipment.	R.F.06, R.F.07,
R.D.03	The design must include a dedicated 3.3 V - 18 V power supply.	R.F.02, RF.06
R.D.04	Portable system with at least 6 m of shielded coaxial cables.	R.F.03, R.F.11
R.D.05	A Teensy 3.6 microcontroller and RF power detector must be used.	R.F.04, R.F.05, R.F.06, R.F.07
R.D.06	Further data processing will be done on a separate computer.	R.F.04, RF.05
R.D.07	The system must include a common external 25 MHz reference for the LNBs.	R.F.09
R.D.08	The design must include a metal enclosure for the exposed RF equipment.	R.F.10

Table 3.3: The set of ATPs were performed to determine whether the various user and functional requirements were achieved.

Index	Test Procedure	Reference
A.01	A known source (sun) will drift across the elements and the output fringes will be observed. The measured fringe phase and corresponding theoretical baseline will be compared to the physical baseline.	R.F.01, RF.09
A.02	The sun will be observed across varying baselines. As the baseline is increased, the fringe frequency is expected to increase, while the fringe amplitude should decrease. The baseline for which the fringe amplitude reduces to approximately zero will be compared to the theoretical baseline required to resolve the sun.	R.F.03, R.F.04, R.F.05
A.03	While observing the sun, one element will continuously be rotated resulting in an increase and decrease in correlation. The correlation should decrease when the elements are pointing in opposite directions.	R.F.04, R.F.06, R.F.07
A.04	Custom manufactured RF components will be measured individually using a Vector Network Analyser (VNA). The measured results will be compared to the corresponding simulated results to examine how well signals are separated into I-Q components.	R.F.06, R.F.07
A.05	Measure both modified LNBs response (power and IF frequency) when in the presence of a wire antenna transmitting at 10.85 GHz. This result will be compared to the unmodified LNBs response to verify that the modified LNBs' PLLs are locking correctly.	R.F.02, R.F.09
A.06	The designed RF power detectors will be calibrated at 1.10 GHz using a calibrated RF signal generator. Thereafter the calibrated power detectors response to varying (known) RF levels will be measured. The error (difference between measured and expected outcome) should be less than 30 mV.	R.F.04, R.F.05

3.4 CONSTRAINTS

With any system there are set of constraints which limit the extent of its development. This section outlines the constraints, which were imposed on the development of this two-element radio interferometer.

3.4.1 Budget

Although a generous budget of of R 26 000 was allocated to this project by the South African Radio Astronomy Observatory (SARAO), the final implementation should cost ideally less than R 10 000 to replicate. This was to encourage further replication and development by students.

3.4.2 Availability of Components

Although a large majority of the components are commonly used for the viewing of satellite TV content, there were certain infrequently used components such as filters and bias tees, which were more challenging to procure - some of which needed to be imported, while others needed to be manufactured locally (albeit more expensive).

3.4.3 Time

A time frame of 10 - 12 months was allocated to the development of the system. This was challenging as certain components were purchased or manufactured (such as the PCBs) overseas and import times extended to weeks in certain cases.

Furthermore, the SARS-CoV-2 pandemic imposed severe lockdowns across the world during 2020, which further restricted access to equipment needed for testing.

3.5 DESIGN METHODOLOGY

With the main systems requirements identified, this section moves on to describe the design process implemented throughout the project. As previously mentioned, the spiral model was followed, as it allowed for regular prototyping and testing of the system. This section outlines the major developments in each stage of prototyping, of which there were four; these are then summarised in Figure 3.1. It is to be noted that the output of each stage resulted in progression toward the final goal of developing a two-element radio interferometer capable of complex correlation.

3.5.1 Initial Testing

The first stage of testing focused around operating the standard LNB without using a decoder. This included supplying DC power to the LNB and measuring the IF outputs. This was followed by the design of RF power detectors to overcome the limitations of standard satellite finders. Thereafter, a single dish receiver was developed to evaluate the feasibility of using satellite TV equipment for radio astronomy. Lastly, an incoherent two-element adding interferometer was developed using the unmodified LNBs.

3.5.2 Coherency between Elements

The main purpose of this stage was to measure the performance of the standard XTAL present in the LNB, remove it (XTAL), and replace it with an equivalent reference that could be used in both LNBs. An adding interferometer was then constructed using the modified LNBs.

3.5.3 Filtering, In-phase and Quadrature Outputs

The third stage of the of development focused on separating the LNB outputs into its I-Q components such that complex correlation could be performed. Two techniques were investigated: introducing a second heterodyne stage or direct separation of signals into I-Q components - the latter was more feasible. The corresponding network of PCBs were then designed and manufactured.

3.5.4 Complete System Testing

The final stage of the system development focused on the complete system implementation and tests. This included the use of modified LNBs along with the specialised PCBs. Tests performed included drift scan observations of the sun as well as performing complex correlation of RF signals.

3.6 SUMMARY OF REQUIREMENTS AND METHODOLOGY

This chapter commenced by identifying a set of user and functional requirements which served as the basis for the project's development. The main requirement was the development of a two-element radio interferometer which would be used as an educational tool. Furthermore, the system would repurpose satellite TV equipment.

A corresponding set of design requirements and ATPs were generated to ensure that these requirements were fulfilled. Thereafter, the main project constraints were identified, namely: cost, availability of components, and time.

The chapter then concluded by discussing the design methodology, which was comprised of the initial testing stages, realising coherency, separating IF signals into I-Q components required by the complex correlator, and lastly, full-system testing.

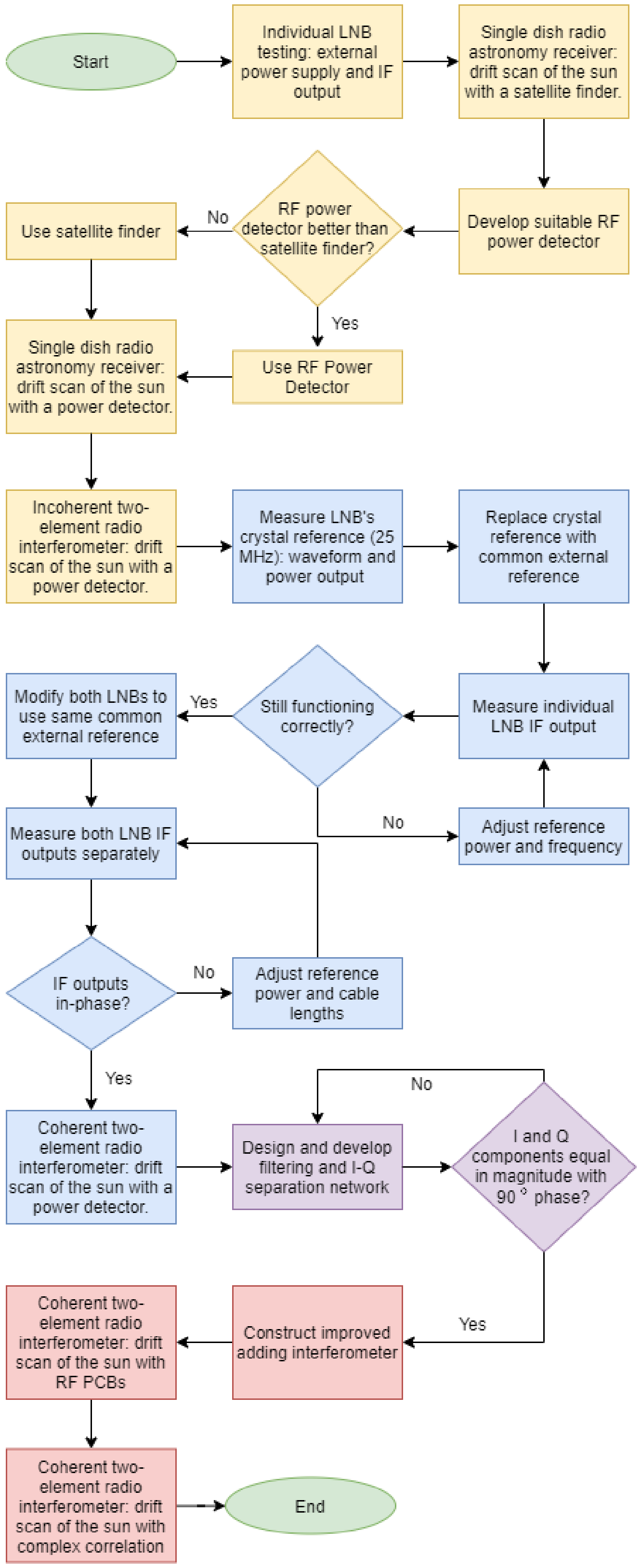

Figure 3.1: Overview of the design process followed - blocks of the same colour indicate the main aspects associated with a particular stage/ prototype.

CHAPTER 4

INITIAL INTERFEROMETER TESTING

Initial testing of the available satellite TV equipment was conducted in order to obtain a better understanding of its operation and to determine which aspects needed to be improved upon. This was an important task as one of the functional requirements identified in Chapter 3 was that the system should make use of repurposed satellite TV equipment. These tests include lab-based measurements of the standard LNB, single-dish astronomy observations, as well as two-element interferometer observations.

Furthermore, it is to noted that the various design and testing stages discussed in this chapter as well as Chapters 5 and 6 followed the scope of minimising cost, repurposing as many components as possible, reducing compatibility issues, and minimising the number of components required to develop the two-element radio interferometer.

This chapter describes how these initial tests were conducted, what modifications were made to existing equipment, and the design of additional hardware to partially fulfil the user requirements outlined in Chapter 3. Modifications include establishing coherency between LNBs, while additional power detector PCBs were designed for data-logging purposes. The chapter then concludes by discussing the challenges and limitations of the existing hardware as well as how these would be addressed in subsequent chapters.

4.1 TESTING AND OBSERVATIONS USING COMMERCIAL EQUIPMENT

As previously discussed, the LNB performs a crucial role in the reception of digital satellite TV. Its low-cost, compact integrated structure, comprised of among others, a Low-Noise Amplifier (LNA), bandpass filter, down-converter, and IF amplifier, made it a viable solution for the front-end of the receiver. There are a variety of commercially available LNBs, however in South Africa the most commonly used LNBs are manufactured by Ellies Elsat (Figures 4.1a and 4.1b) and Aerial King (Figures 4.2a and 4.2b).

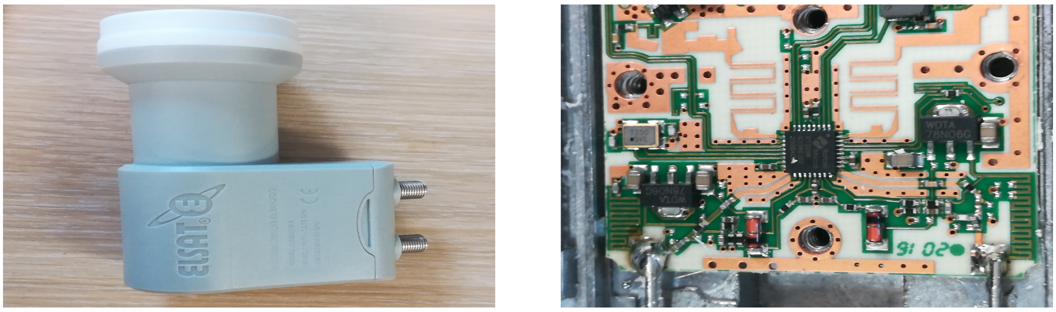

(a) Outer package

(b) Internal Circuitry.

Figure 4.1: Ellies Elsat Twin LNB

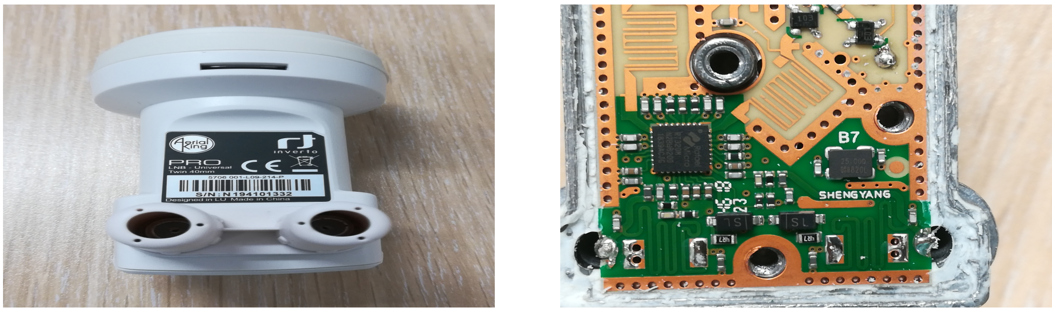

(a) Outer package

(b) Internal Circuitry.

Figure 4.2: Aerial King Twin LNB

At the core of both these examples is a Rafeal Micro IC which downconverts the 10.75 GHz - 12.75 GHz RF band to 0.95 GHz - 2.150 GHz. Both devices offer a similar rated performance for a similar price, but the Aerial King equivalent is physically smaller, which would make modifications challenging. As a result of this, it was decided to make use of the Ellies Elsat equivalent.

4.1.1 **LNB RF Input and IF Output**

A simple wire antenna was used to verify the stated typical operation of the LNB. The wire antenna was connected to a Rhode and Schwarz SMF 100A Signal Generator which together formed the RF test transmitter. The signal generator was configured for an RF output of -20 dBm at 10.85 GHz.

Initial lab-based tests indicated that along with its larger size, the twin LNB (two IF outputs) has the added advantage that if only one IF output was required, the unused IF-port could solely be used for supplying the LNB with its DC power. This would ensure that the DC voltage and IF signal are on separate coaxial cables, which reduces the need for an external bias tee.

However, this technique was not entirely correct, as it did not provide DC power to all components within the LNB. This was a prominent issue when attempting to observe the sun and resulted in considerable errors and delays in testing. This issue as well as how it was resolved will be discussed in Section 4.4. Regardless of this issue, the lab-based tests described below were still valid in determining the overall operation of the LNB.

In typical satellite TV receivers, the LNB receives its DC power from the decoder via the same coaxial cable which carries the IF signal. However, since a decoder was not used in this project, the DC power was supplied from a Hewlett Packard E3630A power supply set to 12 V which fed into one of the LNB IF ports.

Based on its rated operation, the 12 V DC supply should trigger the use of the LNB's 9.75 GHz LO and the corresponding IF output should be at 1.10 GHz. The LNB output was connected to a Keysight E4407B spectrum analyser configured for a centre frequency of 1.10 GHz and 0.1 GHz span, to observe the IF output spectrum. The entire equipment setup used to conduct this test is shown in Figure 4.3.

Figure 4.4 shows the difference in the output spectrum between when the RF signal generator was switched off and when the RF signal generator was switched on. With the RF signal generator switch on, there was a distinguishable peak in output of approximately - 36 dBm centred at 1.10 GHz.

The magnitude of the output power was significantly lower than the transmitted power, which was unexpected given the rated high-gain of the device. This issue was related to the LNB's DC power supply previously mentioned. Regardless of this, the output was still well above the noise floor and importantly, the output was at 1.10 GHz. This verified the initial understanding of the LNBs operation and specifically verified the use of the internal 9.75 GHz LO for down-conversion when with a 12 V DC supply.

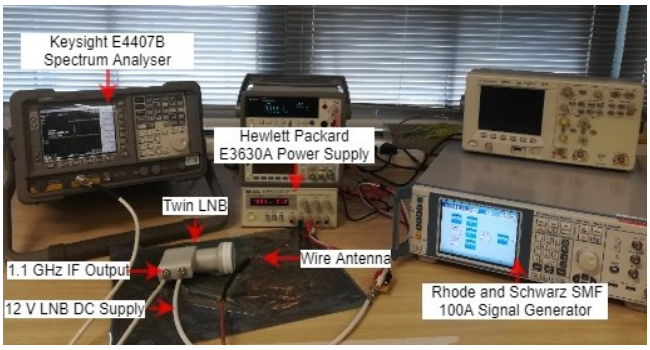

Figure 4.3: Equipment setup used to test the functionality of a twin LNB. The LNB was powered by a DC power supply fed into an unused IF port. The signal generator along with a wire antenna transmitted a 10.85 GHz RF signal, which was received by the LNB. The output 1.10 GHz IF signal was then displayed on the spectrum analyser.

(a) RF signal generator switched on

(b) RF signal generator switched off

Figure 4.4: Change in output IF output spectrum with and without the presence of a 10.85 GHz RF signal.

4.1.2 Satellite Finder

As previously discussed, the adding interferometer required a square-law operation which is typically obtained using a RF power detector. A satellite finder is commonly used for aligning TV dishes with their respective satellite transmitter. A RF power detector lies at the core of such a device and its output varies depending on the received power levels. Thus, the satellite finder was one of the initial detector techniques explored.

There are a variety of devices available with capabilities and sensitivity varying depending on price - the most common features include a meter display and speaker, such as the device used for testing shown in Figure 4.5. Typically, the device is connected between the LNB and decoder during installation. The satellite finder's meter and speaker responds as the dish's alignment with the transmitter improves. A greater meter deflection and louder ”squeal” indicates improved alignment.

Since the satellite finder responds to all RF signals within the LNB's band, it too has previously been repurposed for radio astronomy observations such as Itty Bitty Radio Telescope (IBT) developed by the Society of Amateur Radio Astronomers (SARA) [36].

Similar tests to those described in Section 4.1.1 were conducted using the satellite signal finder instead of a spectrum analyser, as shown in Figure 4.6. A greater meter deflection and louder ”squeal” was observed as the transmitted power was increased or as the wire antenna was brought closer to the LNB, as per Figure 4.6a. The output then decreases when the wire antenna is removed or the transmitter is switched off as per Figure 4.6b. These results indicated that the satellite signal finder was operating correctly. This device also included a potentiometer to adjust the detector gain which could be used for observing weaker signals.

Figure 4.5: Common satellite finder used to align satellite TV dishes with their respective satellite transmitters.

(a) RF signal state: on (transmitting).

(b) RF signal generator switched off (not transmitting).

Figure 4.6: Change in satellite finder output with and without the presence of a 10.85 GHz RF signal. The signal generator allows the RF signal state (red circle) to be switched on/off without needing to power-down the device.

4.1.3 Limitations of Existing Hardware

These initial tests indicated that existing commercial hardware could be used for radio astronomy observations, however, with limited capabilities.

The LNB's 9.75 GHz LO was generated using a XTAL specific to each individual LNB. Thus, the LNB's needed to be modified to obtain coherency between a pair of LNBs such that they share a common reference.

While the satellite finder is capable of detecting RF signals, it provides limited data-capturing functionality. The coarse scale and increments of the analogue meter along with the instability of the galvanometer limits the accuracy and precision of measurements. Instead, dedicated RF power detectors capable of being calibrated were designed. These detectors were also designed to include data-logging and data-storage functionality.

Both performance issues/ improvements relating to the LNBs and RF power detectors are addressed throughout the remainder of this chapter.

4.2 LNB Reference Measurements and Modifications

As previously discussed, each LNB comprised of two LOs, one at 9.75 GHz and one at 10.60 GHz. These were generated by a PLL internal to the Rafael IC and made use of an external (to the IC) 25 MHz reference. The 25 MHz XTAL resonator along with the two adjacent capacitors (Figure 4.7) form the 25 MHz crystal oscillator circuit which serves as a reference to the IC's PLL. As the PLL itself could not be dismantled/ modified, the only way to obtain coherency (as required for interferometry) between two LNBs was to replace the individual crystal oscillators with a common 25 MHz reference.

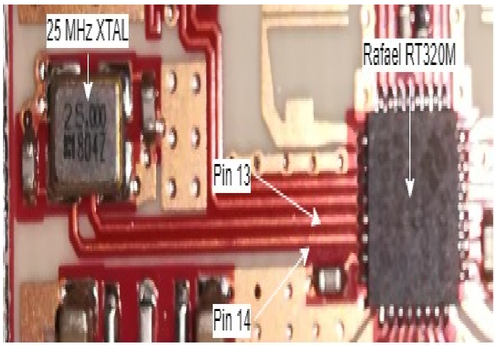

Figure 4.7: Enlarged view of the internal LNB circuitry which shows the external 25 MHz reference oscillator along with its traces which are supplied to pin 13 and pin 14 of the RT320M. The external 25 MHz oscillator comprised of a 25 MHz crystal resonator as well as two capacitors.

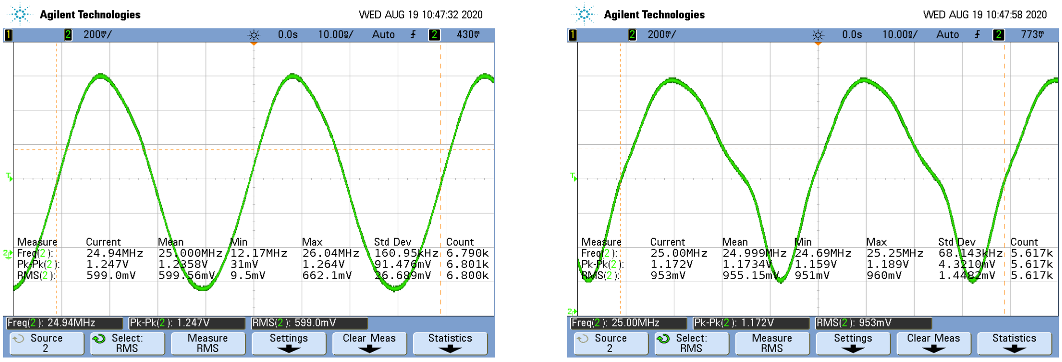

```
Measure      Current    Mean        Min        Max        Std Dev     Count
Freq(2 ):    24.94MHz   25.000MHz   12.17MHz   26.04MHz   160.95kHz   6.790k
Pk-Pk(2 ):   1.247V     1.2358V     31mV       1.264V     91.476mV    6.801k
RMS(2 ):     599.0mV    599.56mV    9.5mV      662.1mV    26.689mV    6.800k

Freq(2 ): 24.94MHz   Pk-Pk(2 ): 1.247V   RMS(2 ): 599.0mV
```

(a) Signal measured at pin 13

```
Measure      Current    Mean        Min        Max        Std Dev     Count
Freq(2 ):    25.00MHz   24.999MHz   24.69MHz   25.25MHz   68.143kHz   5.617k
Pk-Pk(2 ):   1.172V     1.1734V     1.159V     1.189V     4.3210mV    5.617k
RMS(2 ):     953mV      955.15mV    951mV      960mV      1.4482mV    5.617k

Freq(2 ): 25.00MHz   Pk-Pk(2 ): 1.172V   RMS(2 ): 953mV
```

(b) Signal measured at pin 14

Figure 4.8: Measured input and output waveforms of the 25 MHz XTAL. Pin 13 showed a smoother sinusoidal waveform which verified that it was indeed the XTAL input pin of the RT320M.

4.2.1 External 25 MHz Reference

The unmodified LNB was once again connected to the DC power supply in order to measure the input and output signals of the XTAL. This was necessary as the common source replacing the XTAL needed to provide sufficient power for the PLL to lock. As can be seen by the PCB traces in Figure 4.7, the IC features two pins for the XTAL, however it is unclear which pin/pad matches to the input and output of the XTAL.

Both XTAL pads corresponding to these traces were measured using a Keysight DS05012A oscilloscope. Pin 13 (Figure 4.8a) showed a less distorted 25 MHz sinusoidal signal compared to pin 14 (Figure 4.8b) - this indicated that pin 13 must be be the input. Measurements further found the remaining two XTAL pads to be grounded. These results all correspond to the information provided in the datasheet. Due to proprietary reasons, the Rafael Micro RT320M schematic and datasheet could not be included in this report.

The power supplied by the XTAL, P_{XTAL}, was determined using 4.1, where V_{RMS} is the measured root-mean-square (RMS) voltage of the XTAL, R, the impedance, and α the probe attenuation. Upon measurement, $V_{RMS} = 0.599V$, $R = 50\Omega$, and as a 10:1 probe attenuation was used, thus $\alpha = 10$. The resulting XTAL power was -1.44 dBm.

$$P_{Ref} = 10\log_{10}(\frac{{V_{rms}}^2 * 10^3}{R\alpha})\ dBm \tag{4.1}$$

The XTAL was then removed, which revealed the XTAL pads shown in Figure 4.9a. Based on the LNB modifica-

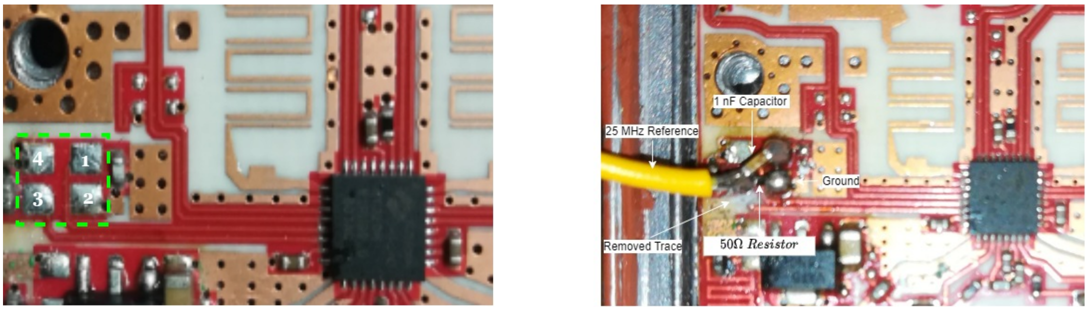

(a) Removal of the 25 MHz XTAL and exposed pads

(b) Replacement 25MHz referece and modifications.

Figure 4.9: Removal of the 25 MHz XTAL revealed which pads served as the crystal input and output of the RT320M. Pad one served as the input, pad three served as the output, and pad two and four were grounded. The 25 MHz reference from the signal generator was supplied to pad three, which was then connected to pad one (input) via a DC blocking capacitor. An additional 50 Ω resistor was included for improved matching

(a) Equipment setup.

(b) IF output spectrum.

Figure 4.10: Equipment setup and IF output spectrum of the modified LNB when in the presence of a 10.85 GHz RF signal. The same test conditions were used as previously conducted for the unmodified LNB. The modified LNB still showed a distinguishable peak of approximately -35.8 dBm at 1.10 GHz.

tion guidelines recommended by [7, 8], the following modifications were done in order to accommodate a different 25 MHz reference, all of which are also shown in Figure 4.9b:

- Removal of capacitors adjacent to pad one and pad three (initially formed part of the crystal oscillator circuit).
- Removal of trace connecting pad three to pin fourteen.
- Inserting 50 Ω matching resistor between pad two (ground) and pad three.
- Inserting a 1 nF DC blocking capacitor between pad one and three.
- Supply of an external 25 MHz reference to pad three.

The Keysight 33522A function generator was used to replicate the XTAL's 25 MHz sinusoidal input signal - this replicated signal was supplied to the modified LNB along the wire shown soldered to pad 3 in Figure 4.9b. To be able to supply the equivalent amount of power as the XTAL, the function generator was configured to output an RMS voltage of 0.189 V instead of 0.599 V as no probe attenuation was used.

The now modified LNB was tested under the same conditions as the unmodified LNB descibed in Section 4.1.1. The equipment setup and performance of the modified LNB is shown in Figure 4.10.

These results indicate that the modified LNB still performs as expected: the PLL adequately locked to a 25 MHz reference which was needed to generate the 9.75 GHz LO; this then downconverts the 10.75 GHz RF signal.

Figure 4.11: The modifed LNB included a BNC panel mount bulkhead connector. Upon completion of the modifactions, the LNB's plastic cover was reattached along with a small cavity to cater for the BNC connector. The modified LNB (left) is shown alongside the standard LNB (right).

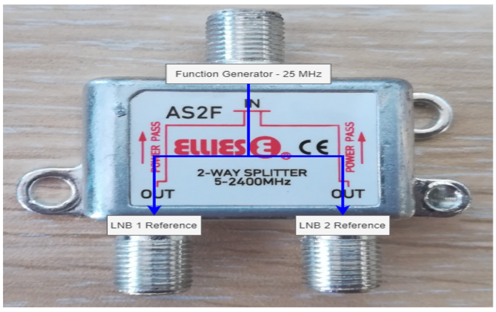

Figure 4.12: Repurposing a commercial TV two-way power-splitter to split the 25 MHz between two LNBs.

The modified LNB's IF output shows a distinguishable peak of approximately -35.8 dBm at 1.10 GHz, similar to unmodified LNB.

With the modifications done to the LNB proving to be successful, the LNB lid was reattached and the centre-pin of a BNC panel mount bulkhead connector was soldered to the wire connected to pad 3. As the overall LNB casing was grounded, the BNC connector was grounded against the LNB lid. Thereafter, the plastic casing was reattached to protect the overall LNB structure, while a small cavity was made to accommodate the BNC connector - Figure 4.11 shows the modified LNB alongside a standard LNB.

4.2.2 Coherent Local Oscillators

Upon successful testing of the first modified LNB, the above described modification was repeated for a second LNB, as at least two elements were needed to form the interferometer. Similar tests as conducted with the first modified LNB verified that the second modified LNB still performed as expected.

To maintain coherency among elements, the 25 MHz reference signal supplied by the function generator needed to be equally split between the two modified LNBs. As there was a large focus on repurposing commercial satellite TV equipment for this project, this splitting was done using the two-way power-splitter shown in Figure 4.12. Generally it is used for splitting a single LNB among two separate decoders for viewing, however, these power splitters have a rated operating frequency of 5 - 2400 MHz, which could be utilised for this purpose.

It was important that the power-splitter equally separated the input signal among the output ports with minimal distortion. This was tested by supplying a 25 MHz sinusoidal signal at the input and measuring the signal at the output ports. The input supplied by the function generator, was configured such that each output of the power-splitter resembled the standard XTAL's behaviour initially shown in Figure 4.8a.

As previously discussed, the measured XTAL power was -1.44 dBm. Thus the signal generator was configured to 1.59 dBm (just more than 3dB i.e. double the power of a single XTAL). This would ensure that the power of each

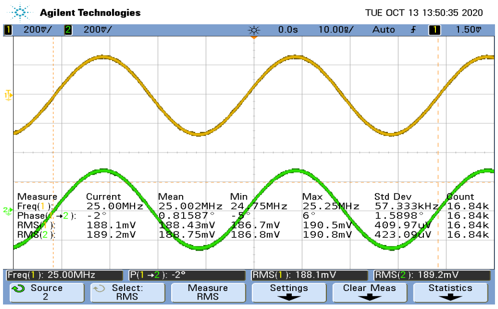

```
Measure      Current    Mean        Min        Max        Std Dev     Count
Freq(1 ):    25.00MHz   25.002MHz   24.75MHz   25.25MHz   57.333kHz   16.84k
Phase(1 →2 ): -2°       0.81587°    -5°        6°         1.5898°     16.84k
RMS(1 ):     188.1mV    188.43mV    186.7mV    190.5mV    409.97uV    16.84k
RMS(2 ):     189.2mV    188.75mV    186.8mV    190.8mV    423.09uV    16.84k

Freq(1 ): 25.00MHz   P(1 →2 ): -2°   RMS(1 ): 188.1mV   RMS(2 ): 189.2mV
```

Figure 4.13: Measured performance of the two output ports of the TV two-way power-splitter. These results indicate minimal amplitude and phase imbalance at 25 MHz between the two output ports.

LNB's reference matched that of the original XTAL. The two outputs were measured using both channels of the oscilloscope and are shown in Figure 4.13.

The results show that both output ports are almost identical in terms of frequency and amplitude. Applying the measured RMS voltages of 188.1 mV and 189.2 mV to 4.1 (noting a 1:1 probe attenuation) results in a reference power of - 1.50 dBm and - 1.45 dBm, respectively, which were slightly below that of the XTAL, but was found to be sufficient in locking the individual PLLs.

It is also to be noted that the power-splitter outputs were closely in-phase with one another with a standard deviation of 1.59°. This implied that the power-splitter did not introduce any significant phase distortion and would be suitable for maintaining coherency between the LNBs' 25 MHz reference signals. This concludes the LNB modifications required to obtain coherency between elements of the interferometer.

4.3 RF POWER DETECTOR

The next issue raised in Section 4.1.3 was the limitations of the satellite finder as the system's detector. This motivated the design of a PCB centred around an Analog Devices' LT 5534 RF power detector, which offered a linear-in-dB relationship between the output voltage and input power. Thus, the measured output voltage and linear transfer function was used to determine the input power - this fulfilled the squaring aspect of the adding interferometer.

The added advantage of a PCB alternative was that the IC output voltage could be sampled using an ADC. The Teensy 3.6 microcontroller was selected as it included two 13-bit ADCs, which would be important in expanding the system to perform complex correlation. It also included a built-in micro SD card reader which made it suitable for remote data-logging.

The PCB was designed to include two power detectors per board, one for the I-component and one for the Q-component - these were necessary for complex correlation. These ICs could also be calibrated which improved accuracy and precision in measurements, and reduced errors between the I-Q measurements. The PCB was designed in KiCad EDA, while JLCPCB was used for PCB manufacturing on a two-layer, 1 mm thick, FR-4 substrate.

4.3.1 Initial Solution: Analog Devices LTC 5596

Initially, the Analog Devices LTC 5596 was selected as the power detector IC as it offered a 35 dB dynamic range, 0.1 GHz - 40 GHz bandwidth, and simplified biasing setup. The manufactured and populated PCB is shown in Figure 4.14. However, there were challenges in using this IC, which were only identified later in the system's development.

Firstly, its quad-flat no-leads (QFN) package meant that it could not be soldered using a standard soldering iron and instead needed to be soldered using a hot-air station. However, delays in accessing such equipment was experienced due to the strict Covid-19 lockdown regulations.

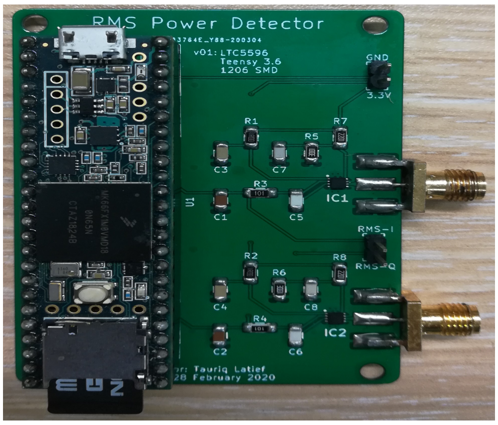

Figure 4.14: Manufactured RF power detector PCB based on the Analog Devices' LTC 5596 and DC 2870A Demonstration Board.

There were also performance issues experienced with the populated PCB - a common issue was that the PCB would perform as expected, but would intermittently shutdown. After several investigations into both the PCB design and soldering techniques, it was found that the issue was attributed to the use of solder paste (used to assist in soldering the IC onto the PCB). Typically, the device would switch-on again if heat was reapplied. Later boards which were populated without solder paste did not experience this issue, thus validating this claim.

Initially, this intermittent issue was thought to be attributed to the PCB design and layout. This prompted the redesign of the power detector sub-system to instead make use of the Analog Devices LT 5534 Power Detector IC. Theses newer PCBs had already been manufactured and populated once the above discussed solder paste issue had been identified and resolved.

However, this section largely raised the iterative design process, debugging issues, and noteworthy time delays experienced in developing the RF power detector.

4.3.2 Improved Solution: Analog Devices LT 5534

The LT 5534 offered a larger dynamic range of 60 dB, however, its operating band was significantly narrower, between 0.05 GHz - 3 GHz - this still catered for the LNB's entire operating bandwidth. The LT 5534 is significantly cheaper compared to the the LTC 5596, the former being $5.34, while the latter being $35.00.

Furthermore, the LT 5534 has a rated a linear response for signals as weak as - 63 dBm at 1.9 GHz. Thus, making it more suitable for detecting weaker radio astronomy signals which were observed by the LNB - this would typically require an additional IF amplifier if the LTC 5596 was to be used.

4.3.2.1 PCB Design and Layout

The DC 748A Demonstration Board was used as guideline for this implementation of the LT 5534 RF Power Detector PCB - the corresponding circuit schematic and PCB layout are shown in Figures 4.15 and 4.16, respectively. As there was a large focus on complex correlation, two power detector ICs were included onto a single PCB, one for the I-component and another for the Q-component of the complex correlation. Furthermore, the board layout and traces were replicated to minimise errors and imbalance between the I-Q measurements.

The PCB design also included female header pins into which the Teensy 3.6 microcontroller could be placed. As previously mentioned, the Teensy 3.6 includes two independent 13-bit analogue-to-digital converters (ADCs) which was configured to synchronously sample the outputs of each of the two power detectors. This would minimise timing errors between the I-Q components. A trace connected the output of top power detector to pin 16 (ADC 0) of the Teensy 3.6, while a separate trace connected the output of the bottom power detector to pin 36 (ADC 1) of the Teensy 3.6.

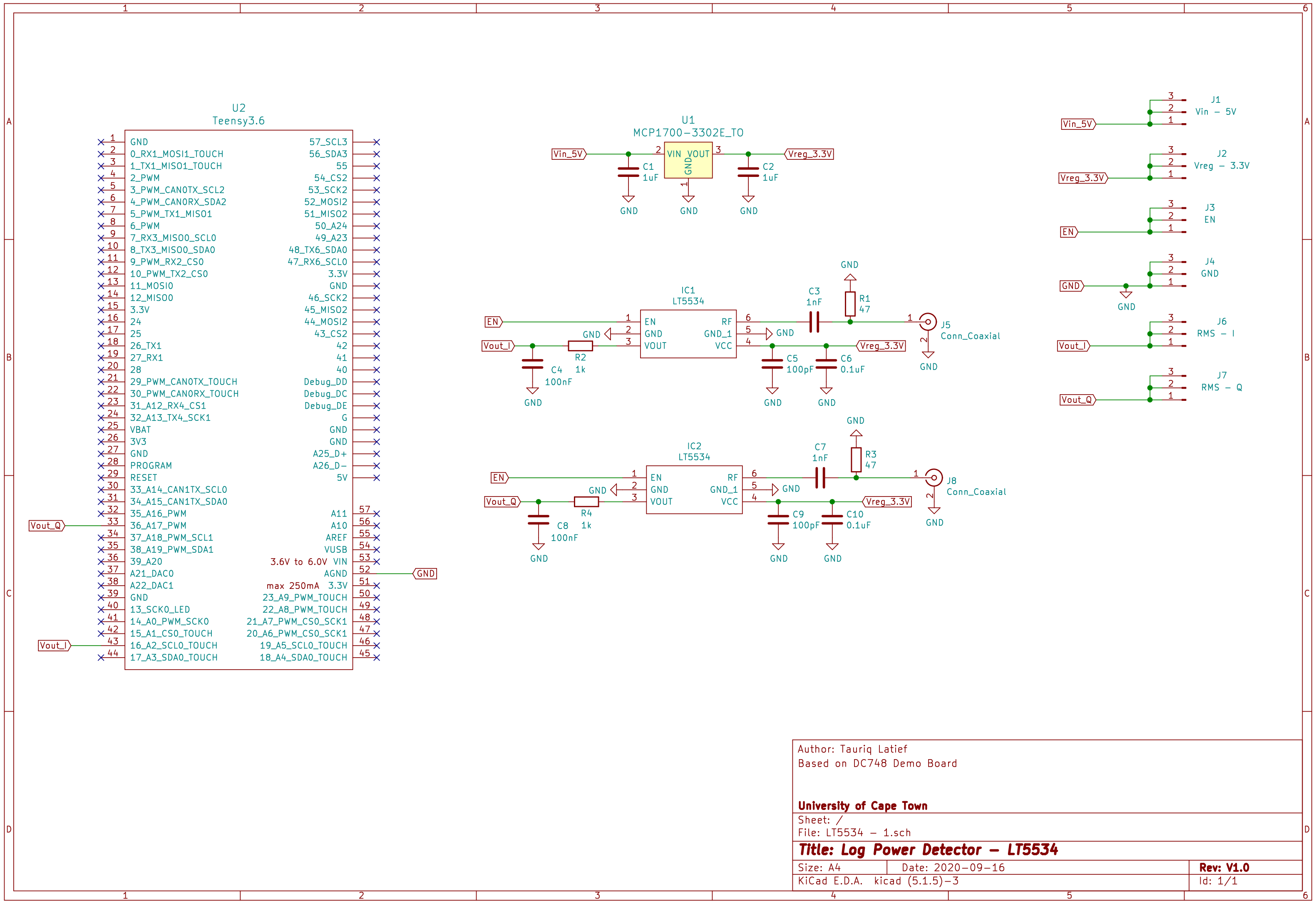

Figure 4.15: Circuit schematic of the RF power detectors based on the Analog Devices LT 5534 and DC 748A demonstration board.

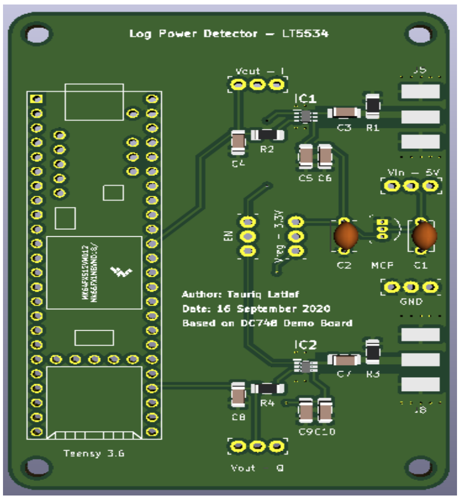

Figure 4.16: 3D model of the RF power detector PCB based on the Analog Devices LT 5534 and DC 748A Demonstration Board.

The PCB design also included other features such as:

- MCP1700-3302E T0-92 3.3V regulator capable of a maximum current of 250 mA.
- Male header pins for the power and ground connections (maximum input of 6V).
- Male header pins to enable/ disable the power detectors - connecting ”EN” to ”V-reg - 3.3V” enables both power detectors.
- Male header pins to directly measure the I-Q outputs of each power detector using a voltmeter.

The Teensy 3.6 was configured to be powered via a male USB micro B connection independent of that used by the power detectors. Under normal conditions, each LT 5534 has a rated current consumption between 5 mA - 9 mA, which was supplied using a power supply. This was largely done to ensure that issues experienced by the LTC 5596 were not going undetected during the LT 5534’s tests. Fortunately, both detectors operated without such issue and a combined current of 14 mA was typically drawn by the power detectors during the testing stages. Having proven that the power detectors operated correctly, future design changes could be made such that the Teensy 3.6 could directly power the power detectors, as it (Teensy 3.6) is capable of providing 3.3V, 250 mA (maximum) to external circuitry. This is well above the requirements of both power detectors.

4.3.2.2 Initial Measurements and Calibration

The manufactured RF power detector PCB is shown in Figure 4.17, which included two SMA edge-mount connectors, one for each of the I-Q components. Also included was the Teensy 3.6 microcontroller and a micro SD card used for data-logging. The manufactured PCB was tested by applying controlled RF signals of varying power to each of the inputs and measuring the output voltages using a voltmeter (later directly sampled using the Teensy 3.6).

Initial tests were conducted using the Rhodes and Schwarz signal generator previously used for the LNB tests. These were conducted at 1.9 GHz so that the measured outputs could be compared to the results available in the datasheet - this is shown in Table 4.1. While the datasheet did not provide exact output values, this close agreement between the measured results and datasheet indicate that both ICs were operating correctly with an almost linear output response.

A further advantage of the Teensy 3.6 microcontroller was that it could be programmed using the Arduino Integrated Development Environment (IDE) and was compatible with various Arduino libraries. This aided in config-

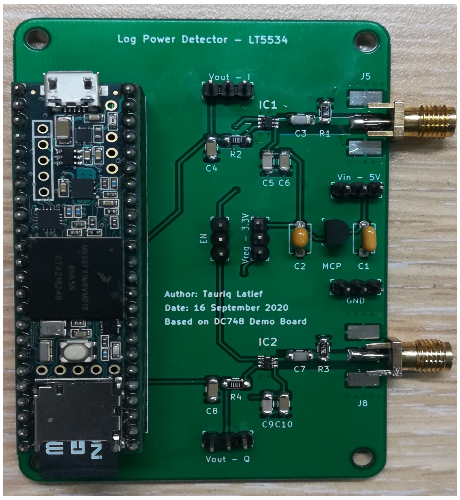

Figure 4.17: Manufactured and populated RF power detector based on the Analog Devices LT 5534 and DC 748A Demonstration Board. The PCB included two SMA connectors for the I-Q inputs along with a Teensy 3.6 and micro SD card for data-logging purposes.

Table 4.1: Measured outputs for each of the power detectors for varying input power levels, compared to the approximate values per the datasheet. Test were conducted at 1.9 GHz and outputs were measured using a voltmeter.

Power Level (dBm)	Measured Output (V)		Datasheet Output (V)
	IC1 (Top)	IC2 (Bottom)	
No RF Input	0.17	0.15	0 - 0.38
-50	0.59	0.61	0.6
-40	0.94	0.96	0.9
-30	1.29	1.32	1.3

uring the ADCs for synchronous sampling as well as offered debugging tools such as printing data to the serial monitor. The Teensy 3.6's ADCs were configured for a 13-bit resolution set to synchronously sample both pin 16 (ADC 0) and pin 36 (ADC 1) at 0.5 s intervals. The measured results were then written to a .CSV file stored on the micro SD card, which could later be viewed and processed. The data could either be stored as a bit value (during calibration) or as a output power level (measured power in dBm once calibration had been completed). The implemented code can be found in Appendix A.

As discussed in Section 2.2.3, specifically 2.20, the output of the squaring operation present in the adding interferometer includes the desired correlated signal along with various uncorrelated components - the latter of which can be removed by time-averaging. In the analogue domain this is achieved using the low-pass filter present at the output of the power detector in Figure 4.15. The filter has a cut-off frequency of 1.59 kHz and corresponding time constant of 100 μs. This time constant relates to the integration time, τ, present in 2.21.

This integration time may not have been sufficient to fulfil the resolution and sensitivity requirements, thus the integration was increased by increasing the sample rate to two samples per second and averaging 1000 readings per sample as evident in Appendix A. This resulted in an overall integration time of 500 s.

As the LT 5534 offers a linear output response for inputs typically in the range of [- 60 dBm, - 0 dBm], the output voltage, V_{out} is related to the input power, P_{in}, as per $V_{out} = m * P_{in} + c$. Thus, only a two-point calibration is needed to determine the gradient, m, and y-intercept, c. In doing so, all later measured output voltages could be related to its corresponding input power levels, which fulfilled the squaring requirement of the adding interferometer. Two-point calibration was conducted on both power detectors similar to the procedure performed during the initial PCB tests.

Table 4.2: Gradient and y-intercept values of both power detectors determined using a two-point calibration conducted at 1.1 GHz with test signals of - 45 dBm and - 35 dBm.

Power Detector	Gradient (V/dB)	Intercept (V)
IC 1 (Top)	0.0349	2.302
IC 2 (Bottom)	0.0361	2.359

Table 4.3: Comparison of measured output voltages relative to the expected voltages of both power detectors once calibration had been completed.

Input	IC 1 (Top) − (V)			IC 2 (Bottom) − (V)		
Signal (dBm)	Measured	Expected	Error	Measured	Expected	Error
- 50	0.5361	0.5550	0.0136	0.5333	0.5539	0.0133
- 40	0.9024	0.9043	0.0019	0.9140	0.9150	0.0009
- 30	1.2672	1.2536	0.0189	1.2894	1.2760	0.0206

Calibration was performed using input signals of - 45 dBm and - 35 dBm at 1.1 GHz. The choice of calibration frequency will be discussed in Chapter 5. Table 4.2 lists the gradient and y-intercept values of both detectors while Table 4.3 shows the error in results after calibration had been performed. These results indicate that both power detectors are operating correctly, with an error in output less than 0.021 V over the 20 dB input range.

4.4 INITIAL RADIO ASTRONOMY OBSERVATIONS

Having successfully developed each of the individual sub-systems, this section focuses on observations of the sun. This includes single-dish observations as well as incoherent and coherent two-element interferometry.

4.4.1 Single-dish Observations

As previously discussed, one of the most basic forms of radio astronomy observations can be conducted using a single dish, LNB, satellite finder, and power supply. Similar observations were conducted, however, the satellite finder was replaced by the LT 5534 RF power detector discussed in the previous section. The block-diagram showing the setup for single-dish observations is shown in Figure 4.18.

The smaller, 0.38 m diameter parabolic reflector dishes, typically used for caravan homes, were used during observations of the sun. While these offer a reduced gain compared to the larger 0.75 m diameter dishes, its (0.38 m) smaller size, larger beamwidth, and built-in steering adjustment made it more manageable to point toward the sun. Figure 4.19 shows the setup of the smaller dish and LNB, while Figure 4.20 shows how the dish was correctly aligned with the sun.

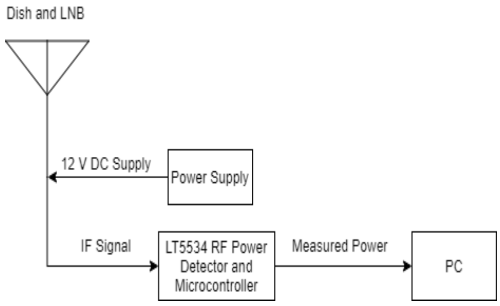

Figure 4.18: Block diagram of the initial setup required for single-dish observations of the sun. The satellite finder was replaced by the LT 5534 power detector which allowed for stable, accurate measurements along with data-logging functionality.

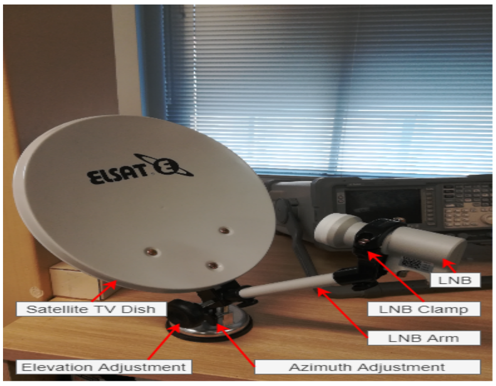

Figure 4.19: Smaller 0.38 m diameter caravan satellite TV dish and LNB. The smaller dish size and adjustment knobs allowed for improved alignment with sources during observations.

(a) LNB misaligned with the sun.

(b) LNB aligned with the sun.

Figure 4.20: Alignment of the satellite TV dish with the sun. By utilising the adjustment knobs on the dish and the suns visible reflection on the LNB, the dish could be rotated in azimuth and elevation such that the sun's reflection could be aligned at the centre of the LNB.

4.4.1.1 LNB IF Amplifier Issues

The initial setup for observing the sun resembled the setup used for testing the LNB dscussed in Section 4.1.1, however, the wire antenna and signal generator was replaced by the sun, while the spectrum analyser was replaced by the power detector. The dish and LNB was then aligned with the sun as per Figure 4.20b. However, the power detector output fluctuated between [- 48.77 dBm, - -48.81 dBm] throughout this initial drift scan of the sun indicating that no RF signal was being observed and the power detector was only measuring noise from the LNB.

Upon further investigation, it was found that the IF amplifier was not enabled. Figure 4.21 shows how the LNB was initially operated: DC power was supplied to port 2, while the IF output was measured on port 1 (discussed in Section 4.1.1). This technique would only enable the LNB's LNA, Rafael Micro IC, and port 2's IF amplifier, but would not enable port 1's IF amplifier. Thus, no signal was observed during observations of the sun.

This further explains the notably lower LNB IF output of - 36 dBm when in the presence of a - 20 dBm RF signal, observed during the lab-based experiments (see Figure 4.4).

4.4.1.2 IF Amplifier Solution: Bias Tees

Two techniques were identified to resolve this issue. The first being a more coarse solution would be to continue to supply the LNBs with DC as per Figure 4.21, but also to permanently link the input of both voltage regulators to one another. This would ensure that both IF amplifiers were enabled, but would require a DC block be placed at the output of port 1 to prevent damage to the RF power detector.

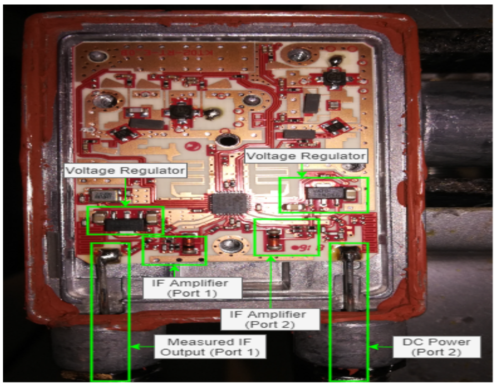

Figure 4.21: Initial LNB setup for lab-based and drift scan observations. DC power is supplied along port 2, while the output IF signal is measured along port 1. This technique proved to be incorrect as it did not enable port 1's IF amplifier.

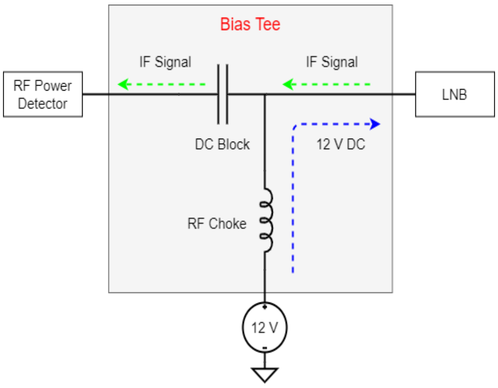

Figure 4.22: Connection of the bias tee between the LNB and RF power detector. The DC blocking capacitor protects the RF power detector from the 12 V DC, while the RF choke isolates the power supply from the IF signal. The bias tee ensures that the 12 V DC supply and IF signal both flow to and from the LNB, respectively.

The second solution would be to make use of an external bias tee, which would provide the LNB with the necessary DC power on port 1, while ensuring that only the IF signal is transmitted to the power detector. This is typically accomplished using a network of RF chokes and DC blocking capacitors, as explained in Figure 4.22.

The second solution was selected to prevent disturbing the LNB modifications (including the BNC connectors mounted onto the LNB cases) which had already been successfully completed when this issue was discovered. Furthermore, suitable inexpensive ($6 each, excluding shipping costs) bias tees had already been procured at the earlier stages of the project, but were not deemed necessary until this issue was identified. The purchased bias tee is shown in Figure 4.23.

LNB tests similar to those shown in Figure 4.10a were once again conducted to verify that the modified LNB was still functioning correctly with the addition of the bias tee. Indeed, the LNB still functioned as previously discussed, however, there were two noteworthy changes as shown in Figure 4.24. The noise was now raised to approximately - 38 dBm (without the bias tee it had been approximately - 58 dBm). More importantly, the LNB output had increased to approximately -11 dBm, when the signal generator was transmitting a weaker - 60 dBm signal. This shows vast improvement in amplification compared to the earlier LNB output of approximately - 36 dBm when in the presence of a - 20 dBm RF signal. These results indicated that the LNB IF amplifier was now functioning correctly with the aid of the bias tee.

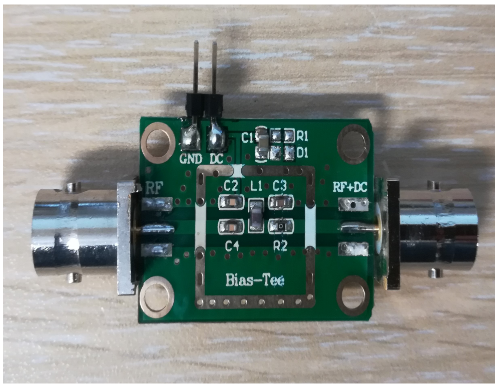

Figure 4.23: Bias tee used to resolve the LNB IF amplifier issues, which had been purchased from DIY More for $6 each (excluding shipping). This resembles the structure discussed by Figure 4.22.

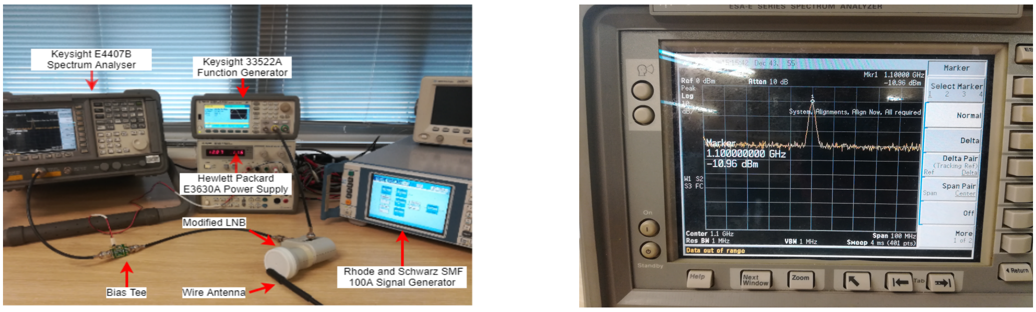

(a) Equipment Setup

(b) IF output spectrum

Figure 4.24: Equipment setup and IF output spectrum of the modified LNB connected to a bias tee, while in the presence of a - 60 dBm RF signal at 10.85 GHz. The output spectrum now shows a raised noise floor along with a distinguishable output peak of approximately - 11 dBm at 1.10 GHz. These results indicated that the LNB still functions correctly and that the IF amplifiers were enabled.

4.4.1.3 *Single-dish Observations of the Sun*

Having had successfully resolved the IF amplifier issue, the sun could now be observed by performing a drift-scan. These observations were performed on the roof of the GH Menzies Building, at the University of Cape Town (UCT). The equipment was connected in a configuration similar to that shown in Figure 4.22 along with a laptop connected to the Teensy 3.6 for live data monitoring - this is shown in Figure 4.25.

As the stands included with the caravan dish kit did not provide tracking capabilities, the dish was aligned with the sun using the procedure described in Figure 4.20. Figure 4.26 shows a successful drift-scan observation of the sun which was performed over 29 minutes.

At the beginning of the observation the sun's reflection was aligned at the centre of the main-beam, thus justifying the initial peak output of -27.02 dBm. As time progressed, the sun drifted out of the main beam resulting in a reduced output of - 28.88 dBm.

Due to the way in which the dish was aligned, only half of the beam pattern could be observed - future observations of the entire beam pattern can be observed by making use of pedestals which include more accurate alignment and tracking functionality.

Furthermore, the half-power (3 dB) beamwidth of the dish could not be classified by performing a drift-scan of the sun. This is due to the extensive physical temperatures to which the LNB was exposed, resulting in an increase in noise in the system, particularly over the LNB's wide RF bandwidth. As discussed in Section 2.2.1, the sensitivity

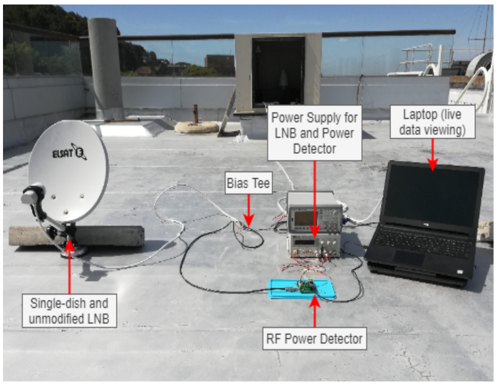

Figure 4.25: Single-dish equipment setup used for drift scan observations of the sun

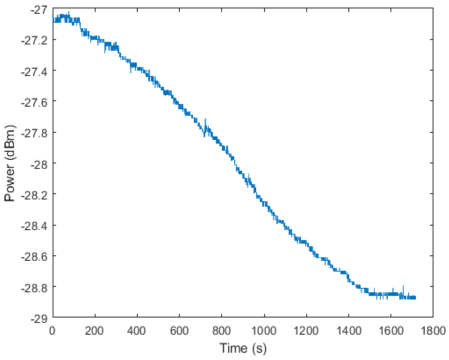

Figure 4.26: Single-dish observation of the sun performed using an unmodified LNB along with the RF power detector.

of the total power radiometer degrades as a result of gain variation. For these particular tests. the raise in physical temperature of the LNB's electronics contributed to large gain variations which affected the overall sensitivity. One technique to reduce the effects of gain variation is to make use of a noise-adding radiometer. This technique combines the source's signal with a known controlled noise source (the latter which is periodically switched on and off), which combined is then input to the total power radiometer. In doing so, the system sensitivity is increased, however, it is no longer susceptible to gain variations [30]. A second approach to mitigate noise and gain variations would be to make use of cooled receiver in which the environmental conditions are better monitored and controlled as often included in professional radio astronomy instruments, however, both of these techniques are beyond the scope of this implementation.

Both the beam pattern and half-power beamwidth can be characterised in a lab environment by placing the dish in a fixed position and rotating a controlled source (controlling the transmitted power, step size, and step rate of the source) around the dish. However, this was beyond the scope of this project. Regardless of this, the result shown in Figure 4.26 indicated that it was indeed possible to observe the sun using satellite TV dishes and LNBs, and further verified that the designed RF power detector was suitable for such observations.

4.4.2 Non-coherent Two-element Interferometer Observations

Having completed the single-dish observations, attention shifted to observing the sun using an incoherent (unmodified LNBs) two-element radio interferometer, similar to the MIT VSRT [10] previously discussed in Chapter 2. However, unlike the MIT VSRT, this configuration did not require additional IF amplification nor did it use a Schottky Diode for the squaring of signals.

As the adding interferometer was the primary interferometry topology under investigation, the IF signals of each

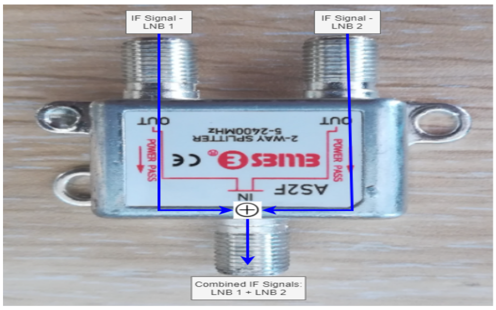

Figure 4.27: Repurposing a TV-splitter to instead combine two LNB IF outputs onto a single port

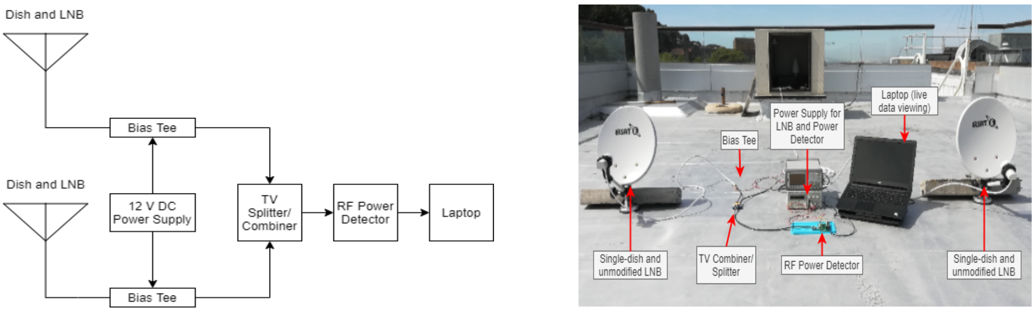

(a) Block diagram configuration

(b) Equipment setup

Figure 4.28: Equipment setup of the two-element incoherent interferometer. The individual IF signals were combined using a repurposed TV combiner which was then measured by the power detector.

LNB would first be combined (added) before being measured by the RF power detector (squared). The conventional TV-splitter previously used to split the 25 MHz reference signals between LNBs in Section 4.2.2 was repurposed to instead combine these LNB signals as per Figure 4.27.

Similar to the single-dish observations, a bias tee was used to provide DC power to each LNB. Thereafter, the individual IF signals were combined using the TV combiner/ splitter and was then measured by the RF power detector. Figure 4.28a shows the block diagram configuration of the incoherent interferometer, which was largely influenced by the designs presented in [10, 11], while Figure 4.28b shows the physical setup of the equipment during observations.

The technique described in Figure 4.20 was once again used to align both dishes such that the sun was at the centre of both main beams. Thus, a peak output was at the beginning of the measurements which would then decay over time as the sun drifted across the dishes.

As per Section 2.2.3 and Section 2.2.5, the expected output of the adding interferometer is sinusoidal fringes which has been modulated by a single antenna's beam pattern. Figure 4.29 shows the measured output of the incoherent two-element interferometer which was performed over a 1.9 m baseline. This measured output differs with the expected theoretical output.

The measured output resembles that of the single-dish in Figure 4.26, which is expected as a result of the modulation. However, the quasi-sinusoidal fringes are not easily distinguishable from the single-dish beam pattern. There are possible fringes near 410 s, 1000 s, and 1330 s, however, these are not clearly recognisable. Such observations were repeated and similar results were observed.

This is attributed to the fact that the LNBs were incoherent and a beat frequency existed between the LNBs [10]. Thus pure constructive or destructive interference between elements did not take place as the sun drifted across the interferometer. Thus a single source, such as the sun, could not be resolved using this interferometer. This justified the efforts previously discussed in modifying LNBs such that they were coherent in order to observe the sun.

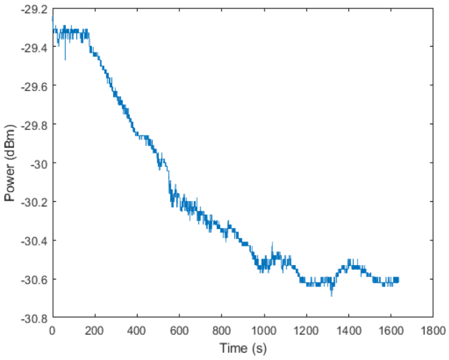

Figure 4.29: Incoherent two-element interferometer observation of the sun performed using unmodified LNBs along with the RF power detector over a 1.9 m baseline.

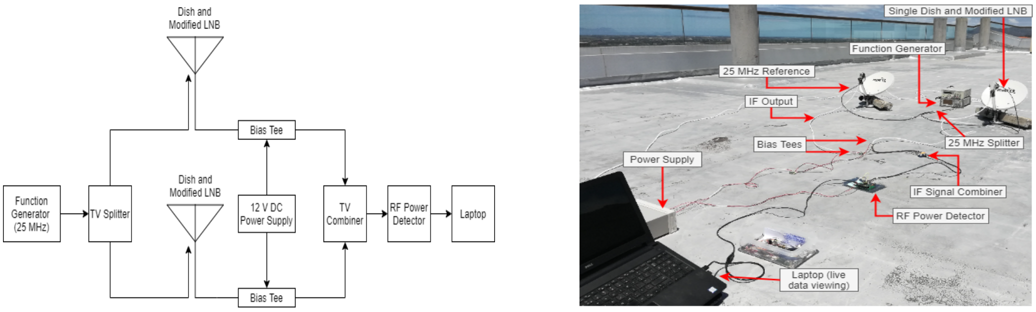

(a) Block diagram configuration

(b) Equipment setup

Figure 4.30: Equipment setup of the coherent two-element interferometer. The function generator along with a TV splitter distributes the 25 MHz reference signal to each of the modified LNBs ensuring coherency among elements.

4.4.3 Coherent Two-element Interferometer Observations

Attention was shifted to the coherent two-element interferometer which made use of modified LNBs, following the limitation imposed by the incoherent two-element interferometer. The equipment setup resembled that of the incoherent two-element interferometer described by Figure 4.28, but now included the function generator and TV splitter to provide the 25 MHz reference to each of the modified LNBs; this adjusted setup is shown in Figure 4.30.

Figure 4.31 shows a drift-scan observation of the sun using the coherent two-element interferometer performed across a 1.9 m baseline. This result included the expected fringes which was discernible from the envelope modulation, however, there was significant fluctuation and instability in the output. Such observations were conducted multiple times along varying baselines, however, similar results were still observed.

4.4.3.1 Modified LNB Issues

With the only difference between the incoherent (Figure 4.28) and coherent interferometer (Figure 4.30) being the modified LNBs, and having proven earlier that the function generator and splitter were operating correctly, these questionable results indicated that the modified LNBs were malfunctioning during drift-scan observations.

Lab-based tests similar to those in Figure 4.10 were once again conducted and verified that the modified LNBs were still operating correctly. However, the LNB and power detector's large operating band encouraged further investigation into the modified LNBs' behaviour over a larger bandwidth (DC - 3 GHz), which revealed the cause of this poor performance. The LNB modifications resulted in significant spurious leakage of the LO (a multiple generated by the PLL) into the IF passband near 0.8475 GHz, as per Figure 4.32 - this issue was present in both modified LNBs, but not in the unmodified LNB.

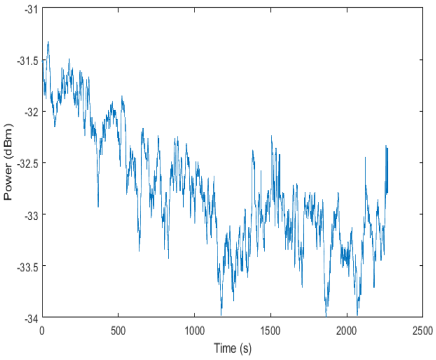

Figure 4.31: Coherent two-element interferometer observation of the sun performed using modified LNBs along with the RF power detector across a 1.9 m baseline.

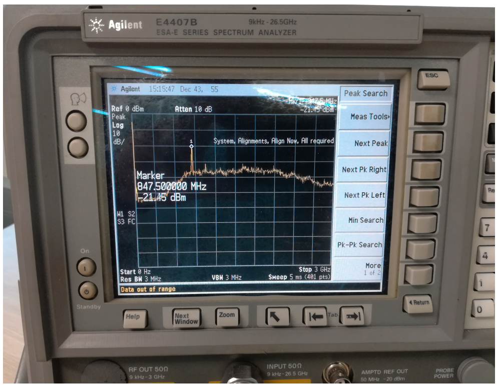

Figure 4.32: Observed spectrum of the modified LNB between DC - 3 GHz. A significant spike in output was observed at 0.8475 GHz. This was present regardless of whether an external source was being observed. Further tests attributed this spurious signal to have originated from the LNB's PLL in conjunction with the function generator.

Due to its significant strength above the noise, this spurious signal had a detrimental impact on the output of the coherent two-element interferometer. Reducing the power of the 25 MHz reference did not change this behaviour, while varying the reference frequency only resulted in the spurious signal shifting in accordance. The spurious signal was not present when the LNB was operated without the reference (as expected, the PLL did not down-convert correctly), however, if the reference was present and later removed, the spurious signal would slowly decay. These tests indicated that the spurious signal was generated by the PLL in conjunction with the function generator as a result of the LNB modifications. Chapter 5 discusses how the effects of this spurious signal was reduced to assist in improved observations of the sun.

4.5 SUMMARY OF CHAPTER

This chapter focused largely on the operation of typical satellite TV equipment and repurposing these for amateur radio astronomy observations; these included dishes, LNBs, and splitters/ combiners. This reiterates the scope of this research, which is to provide readers with a radio interferometer, which to a large extent can replicated using inexpensive repurposed equipment. Attention was placed on modifying the LNBs to achieve coherency among interferometer elements. An RF power detector was also designed to measure the strength of LNBs' signals.

Finally, radio astronomy observations were performed - in particular observing the sun by means of a drift-scan. These include single-dish and interferometer configurations. Due to the nature of its design, fringes were not clearly visible using the incoherent interferometer.Fringes were visible using the coherent interferometer, however, there was significant instability in performance. Later investigations into this indicated that this was attributed to LO leakage into the IF spectrum, which will be addressed in the following chapter.

CHAPTER 5

SYSTEM DESIGN: IF FILTERING AND SEPARATION

Chapter 3 introduced the various design requirements - these specified requirements coupled with the literature presented in chapter 2 served as a guideline for the design of the two-element interferometer. The previous chapter dealt with the initial two-element interferometer and the various limitations present in the system. Specifically, the initial interferometer offered poor resolution due to its wide passband, while the modified LNBs experienced issues attributed to the external LO. Furthermore, I-Q separation of signals was not possible using standard satellite TV equipment. This chapter discusses how these various issues have been addressed.

Issues regarding resolution and LNB performance were addressed by the design of additional IF filters. The two planar filter topologies investigated for these purposes were the hairpin and quarter-wavelength short-circuit stub filters.

Two techniques of separating signals into I-Q components were investigated, namely, the conventional superheterodyne receiver and the direct separation without down-conversion. The latter largely relied on the system being narrownband. Both architectures shared common components (albeit at different frequenices) such as filters, power dividers, and hybrid couplers, all of which are discussed in this chapter.

It would have been impractical to import the various components needed from overseas suppliers, due to import limitations and the weakened Rand-Dollar exchange rate imposed by the pandemic.

Instead, focus was placed on designing these components - the added benefit of this approach was that components could be designed and optimised for specific frequencies. Low-loss 0.508 mm Mercurywave 9350 substrate was chosen, which is locally available. Specifically, local PCB manufacturer, Trax Interconnect, is capable of developing PCBs on Mercurywave substrate. It is to be noted that Trax Interconnect does not manufacture the substrate. Attention was also placed on integrating multiple designs onto single PCBs to minimise losses as well as amplitude and phase imbalance. This chapter also compares the simulated designs to the Mini-circuits equivalents, which served as performance benchmarks.

5.1 I-Q SEPARATION ARCHITECTURES

In order to perform the complex correlation, the LNBs' IF signals first needed to be separated into I-Q components. In Chapter 2, the identified technique of separating components using a quarter-wavelength length of coaxial cable [12] was not suitable as it was only truly valid at a single frequency. Instead, [5] suggested that a superheterodyne network be used to separate signals. Specifically, the LO used in performing this should first be separated into its I-Q components before being mixed with the LNBs' IF signals. A block diagram of this proposed superheterodyne network required to separate both LNBs' IF signals into its I-Q components is depicted in Figure 5.1.

A significant number of components would be required to implement this network, including an additional LO, all

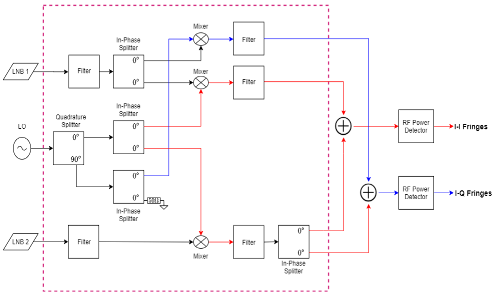

Figure 5.1: Block diagram of the superheterodyne network required to separate the LNBs' IF signals into I-Q components [5] and perform complex correlation. The LO is separated into its I-Q components, while the bandlimited signals are split equally with no phase shift. Components within the purple box are specific to this superheterodyne network.

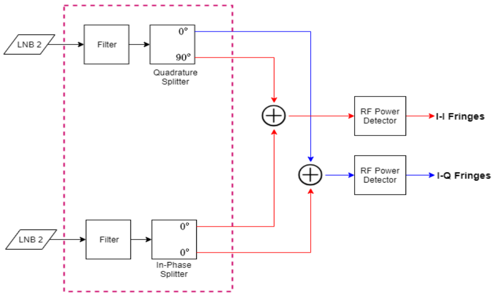

Figure 5.2: Block diagram of the alternative network required to separate the LNBs' IF signals into I-Q components. This network relied on the system being narrowband. Components within the purple box are specific to this I-Q network.

of which would increase the cost and complexity of the overall system.

A more viable alternative was to separate the LNB signals into I-Q components without an additional down-conversion stage. This was achieved using a branchline coupler which relied on quarter-wavelength transmission lines to separate signals into I-Q components, as per Figure 5.2. As a result, the branchline coupler is suited for narrowband architectures, with a fractional bandwidth (FBW) less than 0.20 [14].

For the purposes of this project, both architectures were explored, as the intended system was narrowband (discussed later in this chapter). As such, PCBs were designed and simulated to fulfil both architectures. The latter solution (presented in Figure 5.2) was selected as it provided a simplified architecture along with successful simulated results. The simulated results of the former architecture is included in Appendix B.

5.2 ADDITIONAL IF FILTERING

As previously discussed in Chapter 2, the LNB operated over a wide band of RF frequencies, which were then down-converted to a lower IF by selecting one of two LOs - for this implementation, the low-band was used with a 9.75 GHz LO. This in turn resulted in an LNB IF band between 0.95 GHz - 1.95 GHz (corresponding to a RF band between 10.7 - 11.7 GHz). The low-band was chosen as it did not require a 22 kHz switching tone, unlike the high-band, as discussed in Chapter 4.

Utilising the entire IF bandwidth of 1 GHz would have greatly improved the system's sensitivity as shown by 2.21. Sophisticated digitised systems are able to sample large bandwidths at high speeds and are thus able to correlate the signals with a high resolution. However, for an analogue system, correlating the LNBs entire 1 GHz low-band bandwidth would have resulted in a poor resolution with a large variation in the fringe phase. More specifically, for a 3 m baseline the fringe resolution, given by $\theta_s \approx \frac{\lambda}{D}$, would have varied between $0.49°$ (11.7 GHz) - $0.54°$ (10.7 GHz) - a variation of 9.3%. This variation was minimised by reducing the bandwidth by means of an additional IF

Table 5.1: Intermediate filter specifications

Parameter	Specification
Passband	1.05 - 1.15 GHz
Bandwidth	0.1 GHz
Fractional Bandwidth	0.091
Passband Return Loss	$\geqslant$ 10 dB

filter, as suggested by [11]. Specifically, [11] made use of a tunable 0.04 GHz bandpass filter to reduce the fringe resolution variation from 8.5% to 0.7%.

The IF filters were centred at 1.10 GHz with a bandwidth of 0.1 GHz - further filter specifications are listed in Table 5.1. The centre frequency and bandwidth were selected in conjunction with one another to overcome a few challenges, such as fractional bandwidth (FBW), losses, and suppression of the spurious LO signal near 0.8475 GHz. These filters were suited for the direct I-Q separation and superheterodyne networks. With many RF structures being fractions of a wavelength in length, at these relatively low IF frequencies, filters would be physically large and expensive to manufacture. Thus, third-order IF filters were selected to reduce the PCB size.

Although a narrower passband would improve resolution, the reduced FBW is challenging to achieve using low-order microstrip filters since the roll-off is not as steep as higher-order designs. This is better understood by using a 0.1 GHz bandwidth to compare the FBW centred at either ends of the low-band spectrum. At 0.95 GHz, the FBW is 0.105%, while at 1.95 GHz, the FBW is 0.051 %.

The lower IF cut-off frequency was also avoided as the LNB's roll-off near 0.95 GHz (10.7 GHz RF) was insufficient and would struggle to suppress the spurious LO signal. Accounting for all these factors, the IF filter was chosen to be centred at 1.1 GHz (corresponding to an RF of 10.85 GHz) with a 0.1 GHz bandwidth. The two filter topologies investigated to meet these specifications were the hairpin and stub filter implementations.

5.2.1 Hairpin Filter Design

The commonly-used RF filter design book, "Microwave Filters, Impedance-matching Networks, and Coupling Structures" [37] served as an initial guide in the design of these IF filters. Suitable topologies identified for this FBW involved coupled line microstrip resonators. However, initial simulations of the conventional capacitive-gap coupled and parallel coupled implementations (which made use of unfolded half-wavelength resonators) showed substantial insertion loss which could be attributed to their physically longer structures.

Instead, the hairpin filter design was investigated as it offered a more compact structure [38]. It followed a similar operation and design equations as the parallel coupled structure outlined in [37, 38], but the individual half-wavelength resonators are folded into a "U" shape. The corresponding design equations were incorporated in Cadence AWR iFilter Filter Synthesis tool, which generated the filter dimensions required to achieve the given set of specifications. The tool was configured for a third-order 0.01 dB Chebyshev ripple while matched to 50 Ω (in order to be measured on the Vector Network Analyser). These dimensions were then used as an initial guideline to generate a more accurate model (see Figure 5.3) in CST Studio Suite.

The first iteration of the design showed favourable results as per Figure 5.4. The simulation showed low insertion loss of 0.49 dB near the centre of the band along with a minimum return loss of 22.85 dB at 1.128 GHz. There was also a rise in return loss to 10.7 dB at 1.161 GHz, however, this was still within specification.

Importantly however, both S_{11} and S_{21} parameters showed a shift from the specified centre frequency and an increased bandwidth - the Trust Region Framework was used to further improve these results. As shown in Table 5.2, the optimisation successfully corrected the centre frequency and bandwidth offset to within 0.005 GHz from specification. This improvement in bandwidth and centre frequency is evident in Table 5.2, which compares the initial and optimised results.

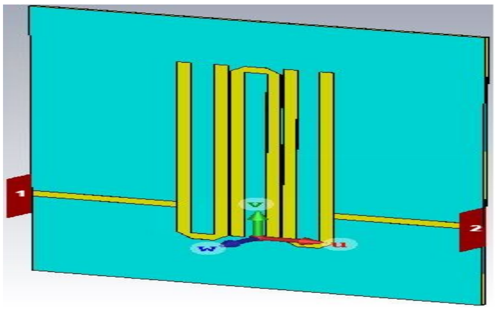

Figure 5.3: CST model of the hairpin filter. Due to the symmetric nature of the design about the y-axis, the structure required fewer parameters to define its shape. This allowed for a quicker computation and optimisation, as fewer parameters needed to be optimised.

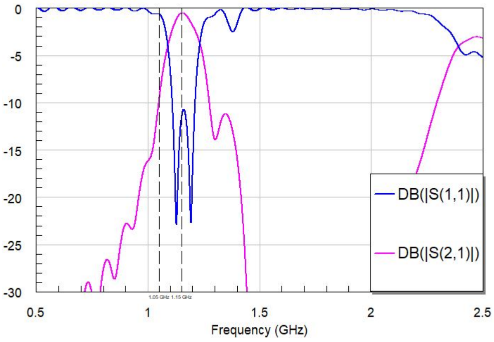

Figure 5.4: Initial S-parameters of the CST hairpin filter model.

Figure 5.5 which shows the optimised S-parameters indicate that although the centre frequency and bandwidth had been corrected, the optimised design showed an increase in insertion loss to 0.88 dB at the centre of the band. Also as a result of the optimisation, there was an increase in passband return loss which now had a minimum of 18.57 dB at 1.064 GHz and a maximum of 9.63 dB at 1.097 GHz. Attempts were made to reduce this raised peak, but were unsuccessful. However, as only 0.014 GHz of the passband is outside the initial specification, this deviation was considered negligible. Furthermore, this filter offered in excess of 20 dB suppression near 0.8475 GHz. The final optimised filter occupied a PCB area of 40.98 mm x 59.22 mm.

5.2.2 **Quarter-wavelength Stub Filters**

The hairpin filters previously discussed successfully met the bandwidth and centre frequency specifications, however, even after optimisation, results showed an undesirable decline in return loss near 1.3 GHz, which could result in spurious transmission, albeit poorly - this decline is attributed to the filter's detuned third pole. Furthermore, a prominent spurious passband exists near 2.3 GHz. Although the latter spurious passband was outside the LNB's IF band, the LNB's roll-off at this upper cut-off frequency was insufficient, thus needed to be avoided. Furthermore, suppression begins to decline near the image band (1.85 GHz - 1.95 GHz) due to the spurious passband, which may be problematic when considering the heterodyne stage discussed in Appendix B.

Table 5.2: Comparison of the hairpin filter's performance before and after optimisation. Improvements in centre frequency and bandwidth were achieved as a result of the Trust Region Framework optimisation tool. The bandwidth was determined for the frequency band in which the return loss was less than 10 dB.

Iteration	Centre Frequency (GHz)	Bandwidth (GHz)
Initial	1.161	0.102
Optimised	1.098	0.100

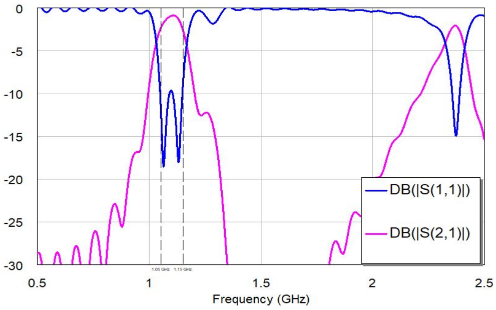

Figure 5.5: Optimised S-parameters of the CST hairpin filter model which showed an improvement in centre frequency and bandwidth compared to the initial simulated results in Figure 5.4.

Thus, quarter-wavelength stub filters were designed to address these issue as its theoretical first spurious passband occurs at three times the centre frequency (i.e. 3.3 GHz) [37], which is well above the LNB's upper cut-off frequency. It is to be noted that the hairpin filter and quarter-wavelength stub filters differ with respect to their direct current (DC) biasing, specifically, the former is a DC open circuit, while the latter is a DC short circuit. For this particular application, the DC conditions were not of primary concern as the desired signals are near 1.1 GHz and any DC signal components would have been blocked by the bias-tee and power detector.

The design rules presented in [38] were used as an initial guideline to develop the CST model. Generally, these filters comprises of a series of single-sided, short-circuited microstrip stubs which are a quarter guided wavelength in length, as shown in Figure 5.6. Typically, these filters are recommended for wideband applications where $0.4 < \text{FBW} < 0.7$ [37], however, there have been narrowband implementations [39, 40] which have achieved FBWs of 0.05 and 0.10, respectively, by adjusting the shape and length of the connecting transmission lines.

The iFilter Filter Synthesis tool was once again used and configured for a third-order stub filter centred at 1.1 GHz with a 0.1 GHz bandwidth, and 0.01 dB Chebyshev ripple matched to 50 Ω. However, such a narrow bandwidth required low impedance single-sided stubs, which would not meet manufacturing capabilities. In order to obtain impedances which could be realised on microstrip, the single-sided stubs shown in Figure 5.6 were extended to double-sided stubs as per Figure 5.7, which effectively placed stubs in parallel, thus doubling the required impedance per stub, albeit with a larger PCB area.

Furthermore, more manageable impedances could also be realised on thinner substrates, thus the initial choice of 0.508 mm Mercurywave substrate. This governed the PCB substrate thickness of all the Mercurywave-based designs, as Trax Interconnect manufactures a panel of PCBs, as opposed to individual PCBs of different substrate thicknesses. Considering these factors, the synthesis tool generated the set of stub and transmission line impedances, which were then matched to their appropriate microstrip dimensions using Cadence TXLine tool. Thereafter, the dimensions were transferred to CST develop the initial model shown in Figure 5.7.

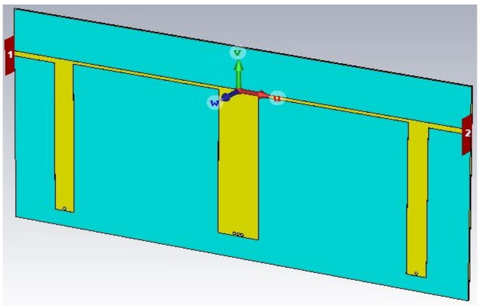

Figure 5.6: Basic outline of the single-sided quarter-wavelength stub filter. The stubs are and connecting transmission lines are a quarter guided wavelength in length. The stubs are short-circuited to ground by circular vias placed near the lower-end of the individual stubs.

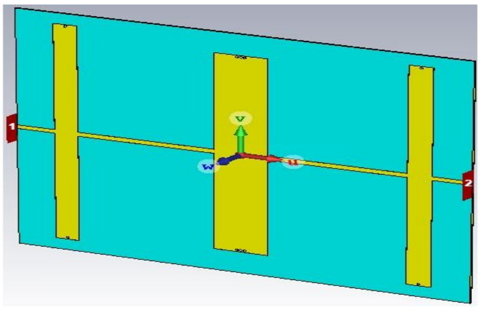

Figure 5.7: CST model of the double-sided quarter-wavelength stub filter. The structure is symmetric about the x- and y-axis which allowed for quicker computation and optimisation.

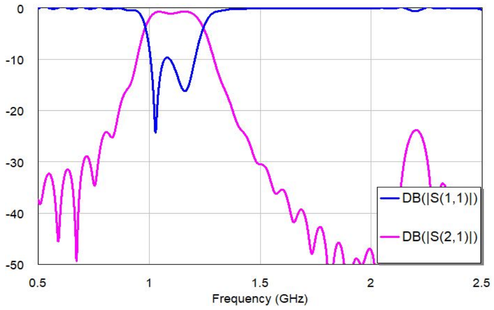

Figure 5.8: Initial simulated S-parameters of the quarter-wavelength stub filter. These results indicate strong suppression of spurious passbands near 1.3 GHz and 2.2 GHz, however, this was traded for a larger bandwidth and negligible shift in centre frequency from the desired specifications.

The simulated results shown in Figure 5.8 indicated that initial design had a maximum insertion loss of 1.10 dB near 1.1 GHz, which then decreased to a minimum of 0.71 dB at 1.16 GHz (i.e. outside the specified passband). This initial result shows that the stub filter experienced greater insertion loss compared to the initial hairpin filter.

Figure 5.8 also indicates acceptable return loss over the passband, with a minute fluctuation above 10 dB near 1.08 GHz. However, this is negligible as it does not rise above 9.66 dB and fails to meet the specifications for less than 0.025 GHz of the specified bandwidth. Notably however, is the absence of spurious passbands near 1.3 GHz and 2.2 GHz, which indicates that the stub filter indeed addressed the shortcomings of the hairpin filter. However, based on the 10 dB return loss points shown in Figure 5.8, the initial stub filter exceeded the bandwidth specification by 0.1 GHz (i.e. double the specified bandwidth). Optimisation using the Trust Region Framework was attempted, but could not overcome this issue.

In an effort to reduce the bandwidth of a similar filter design, [13] made use of stepped impedance connecting lines - this technique was also applied here to overcome the bandwidth issue. Figure 5.9 shows the optimised filter along with an enlarged view of the now stepped connecting transmission lines used in the optimised design, which occupied a PCB area of 111.88 mm x 84.96 mm.

This stepped impedance aided in reducing the bandwidth as can be seen in Table 5.3, which showed a 0.072 GHz reduction in bandwidth, albeit with a negligible shift in centre frequency. Overall, this resulted in an optimised FBW of 0.115 which was significantly narrower than the initial 0.181. This optimised design also achieved more than 24 dB suppression near 0.848 GHz, which should be capable of suppressing the spurious LO signal.

The final S-parameters are shown in Figure 5.10 which graphically shows this improvement in bandwidth and centre frequency. With reference to the return loss, the optimised result showed a further improved minimum of 39.76 dB at 1.131 GHz as well as the absence of any sudden rises, which was not the case in the initial design. The passband insertion loss showed no wavering, but there was a minor increase in insertion loss from the initial 0.706 dB to 0.738 dB.

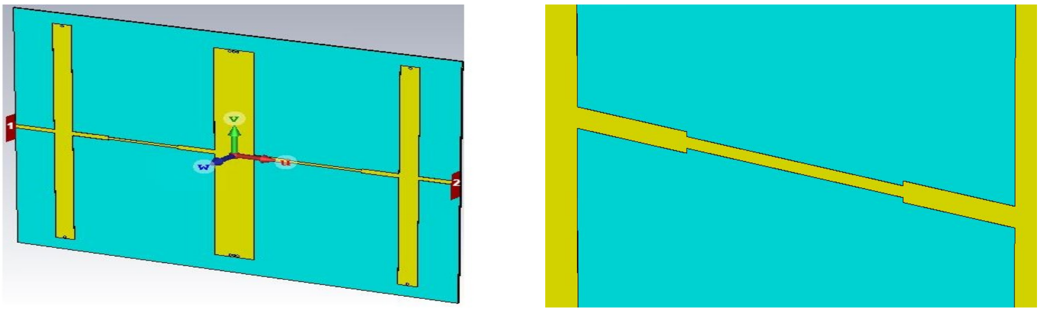

(a) Entire structure.

(b) Enlarged connecting transmission lines

Figure 5.9: The quarter-wavelength stub filter showing the reduced/ stepped impedance connecting transmission lines. These were used to reduce the bandwidth, similar to the implementation in [13].

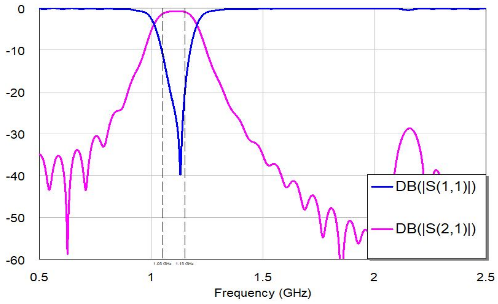

Figure 5.10: S-Parameters of the optimised quarter-wavelength stub filter which made use of stepped impedance connecting transmission lines. The greater selectivity was evident by the reduced bandwidth relative to the initial results along with improved spurious passband suppression compared to the hairpin filter.

Both these designs, namely the hairpin and quarter-wavelength stub filters, closely met the design specifications with performance trade-offs between each other. The hairpin filter had a narrower bandwidth and due to its shape and structure, occupied a smaller PCB area - this greatly reduced the manufacturing cost. However, it struggled to suppress spurious passbands. The quarter-wavelength stub filter managed to suppress spurious passbands to beyond 2.5 GHz and offered lower passband insertion and return loss. However, this was at the expense of a wider passband and a significantly larger PCB area.

5.3 IN-PHASE SIGNAL SEPARATION

As per Figure 5.2, one of the LNB's IF signals needed to be equally split in both amplitude and phase. This was also necessary for the superheterodyne receiver in per Figure 5.1. This separation was achieved using a Wilkinson power divider suited for narrowband operation at 1.1 GHz. The Wilkinson power divider is commonly used in RF applications and can be designed for equal and unequal amplitude split of the input signal among the output ports - the three-port, equal power Wilkinson power divider will be focused on in this section.

The simulated device made use of quarter-wavelength transmission lines to connect the input and output port,

Table 5.3: Comparison of the initial and optimised quarter-wavelength stub filters. Improvements in the stub filter's centre frequency and bandwidth were achieved using the Trust Region Framework optimisation tool and stepped impedance connecting transmission lines. The centre frequency and bandwidth were determined for a return loss less than 10 dB.

Iteration	Centre Frequency (GHz)	Bandwidth (GHz)
Initial	1.106	0.200
Optimised	1.111	0.128

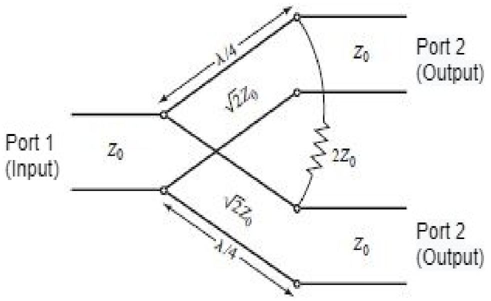

Figure 5.11: Conventional three-port Wilkinson power divider: the input signal at port 1 is equally split between output ports 2 and 3 along with no phase imbalance [14].

along with a resistor placed between the two outputs, as shown in Figure 5.11. All ports were matched to Z_0, and the presence of the resistor provided high isolation between the two output ports. When a signal is incident at the input, it is equally split between the outputs (port 2 and port 3), however when a signal is incident at one of the output ports, half of the signal is transmitted to the input, while the remaining half is dissipated in the resistor. An in-depth analysis of its operation can be found in [14, 41].

5.3.1 **Standard Wilkinson Power Divider**

A common design of the quarter-wavelength transmission line is to use straight or tapered microstrip designs as shown in Figure 5.12, however, a circular design similar to those present in [42, 15] was chosen. As a consequence of the quarter-wavelength transmission lines, the Wilkinson power divider is limited to narrowband operation, thus making it suitable for this operation.

A circular design utilised PCB board space more efficiently, as the quarter-wavelength transmission lines were curved - this reduced the overall board length. This symmetric design also allowed for adequate spacing between output ports. This assisted in output isolation and reduced undesired phase imbalance between the output ports.

Figure 5.13 shows the circular Wilkinson power divider model which was developed in CST. The model was developed on 0.508 mm Mercurywave substrate and TXLine was used to calculate the initial 50 Ω and 70.71 Ω transmission line dimensions for a 1.1 GHz operation. The CST model further accommodates a 100 Ω 0805 surface mount device (SMD) resistor between the two output ports. This design was further compared to the Mini-circuits ZAPD-2+ power divider, as the Mini-circuits device is rated for similar operation.

The Trust Region Framework was used to optimise performance for a slightly larger operating band - these optimised results are shown in Figure 5.14. A noticeable decline in return loss near 1.10 GHz which reached a minimum of 24.66 dB at 1.12 GHz was evident in the simulated results. More notably, the return loss remains

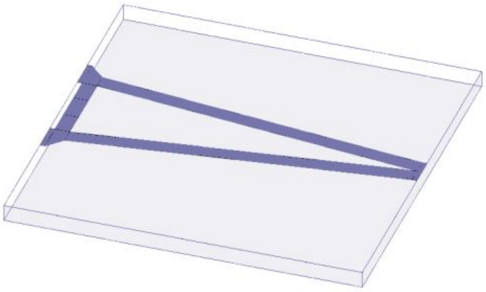

Figure 5.12: Common design of the Wilkinson power divider which makes use of straight transmission lines, each a quarter-wavelength in length, to connect the input port to the two output ports. A resistor of $2Z_0$ is placed between the output ports to improve isolation [15].

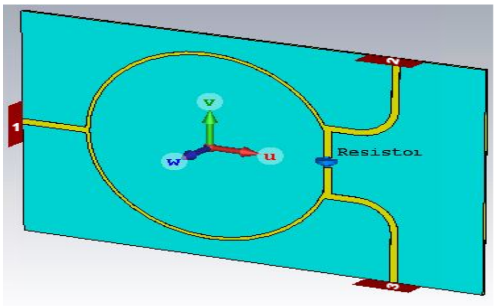

Figure 5.13: Circular Wilkinson power divider model developed in CST including dimension and port labels.

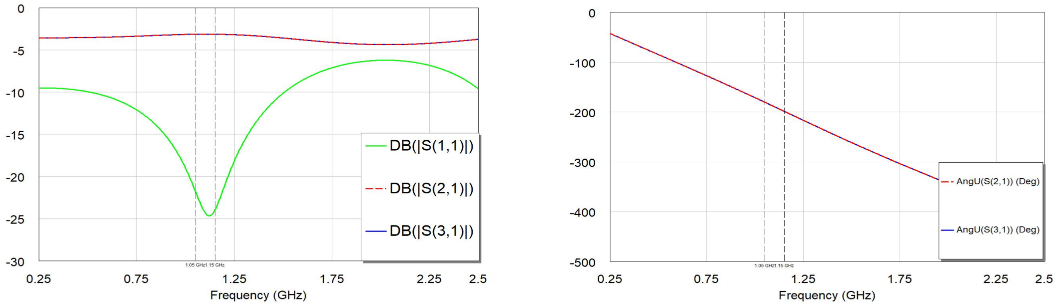

(a) S-parameter amplitudes of the 1.1 GHz Wilkinson power divider (b) S21 and S31 phases of the 1.1 GHz Wilkinson power divider

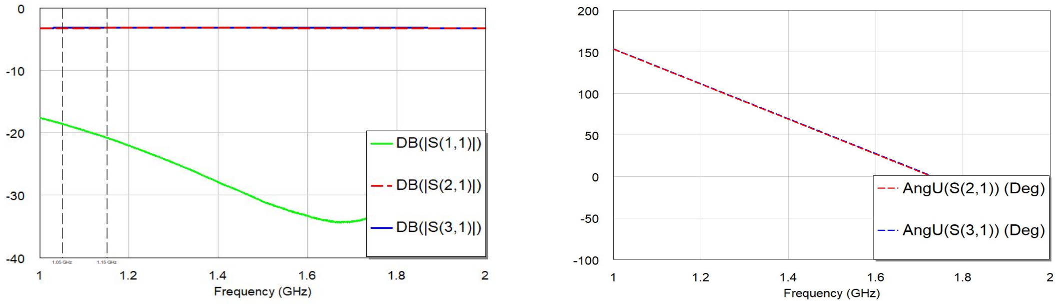

(c) S-parameter amplitudes of the Mini-circuits power divider (d) S21 and S31 phases of the Mini-circuits power divider

Figure 5.14: S-parameter amplitudes and phases of the designed narrowband 1.1 GHz Wilkinson power divider and Mini-circuits ZAPD-2+ Power Divivder.

below 20 dB for the entire 0.1 GHz bandwidth, while insertion loss did not exceed 0.13 dB. Furthermore, the output amplitude fluctuation was less than 0.01 dB, while the output phase remained linear over the band.

Table 5.4 compares the performance of the 1.10 GHz Wilkinson power divider to the Mini-circuits ZAPD-2+ [43] component to determine how feasible the Wilkinson power divider was for the narrowband operation. The simulated results indicated that the Wilkinson power divider's output ports showed no amplitude imbalance over the 0.10 GHz band, while the Mini-circuits component's imbalance remained below 0.04 dB. The overall results indicated that the 1.10 GHz Wilkinson power divider was a suitable solution for equally separating the bandlimited IF signals.

5.3.2 Integrated Filter and Wilkinson Power Divider Structures

Integrating multiple structures/ functions onto a single PCB offered advantages such as improved modelling and minimised losses. As such, focus was placed on merging the 1.1 GHz Wilkinson power divider and each of the IF filter onto a single PCB.

Since 0.508mm Mercurywave substrate was also used for the integrated design, the dimensions of the standalone

Table 5.4: Comparison of the output port amplitude imbalance between the simulated Wilkinson power divider and the Mini-circuits ZAPD-2+.

	S_{21} (dB)			S_{31} (dB)			Imbalance (dB)		
	1.05GHz	1.10GHz	1.15GHz	1.05GHz	1.10GHz	1.15GHz	1.05GHz	1.10GHz	1.15GHz
Simulation	-3.13	-3.12	-3.13	-3.13	-3.12	-3.13	0.00	0.00	0.00
Mini-Circuits	-3.22	-3.23	-3.24	-3.22	-3.21	-3.20	0.00	0.02	0.04

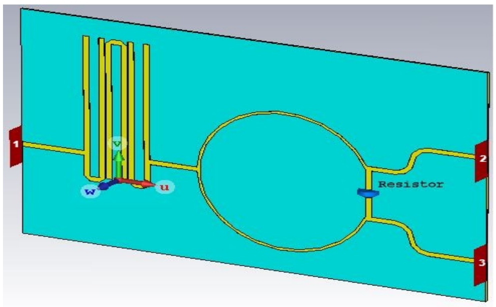

Figure 5.15: CST model of the hairpin filter and Wilkinson power divider integrated onto a single structure. The IF signal arriving at port 1 is filtered and then equally split between output ports 2 and 3.

filters and Wilkinson power divider models could be used to develop the initial CST integrated models. Since the separate improved designs were optimised for a standalone performance, these integrated designs also needed to be optimised for an improved integrated performance. This was done using the CST Trust Region Framework, albeit now with limitations due to the increased number of parameters available.

5.3.2.1 *Hairpin Filter and Wilkinson Power Divider Integration*

Figure 5.15 shows the Wilkinson power divider integrated onto the hairpin filter PCB. The compact structure of the individual hairpin filter and Wilkinson power divider allowed for an overall PCB size of 98.73 mm x 61.26 mm. Majority of this area was attributed to the size of the power divider structure.

The simulated performance of the integrated design is shown in Figure 5.16. Figure 5.16a showed the strong amplitude balance between the output ports which was attributed to the symmetry of each individual structure. Similar to the individual filter discussions, the - 10 dB S_{11} points were used to determine the operating frequency. The integrated design showed a centre frequency of 1.0955 GHz and a bandwidth 0.103 GHz, which closely matches the initial filter specification and individual hairpin filter.

However, it is to be noted that within this band, S_{11} deviated from this - 10 dB passband requirement for approxi-

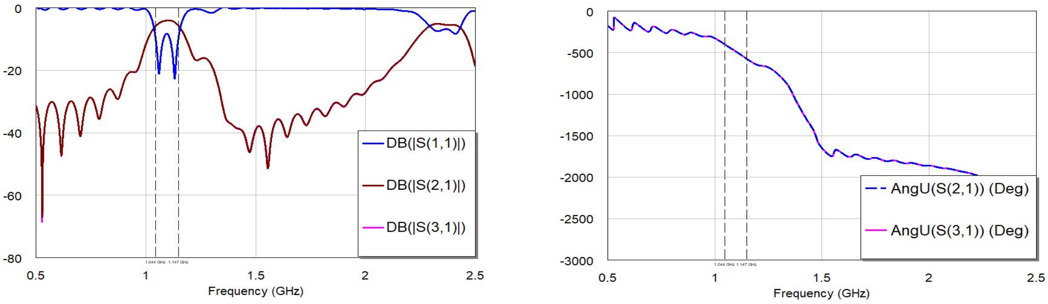

(a) S-parameter amplitudes.

(b) Output ports' S-parameter phases.

Figure 5.16: S-parameter amplitudes and phases of the integrated hairpin filter and Wilkinson power divider structure shown in Figure 5.15.

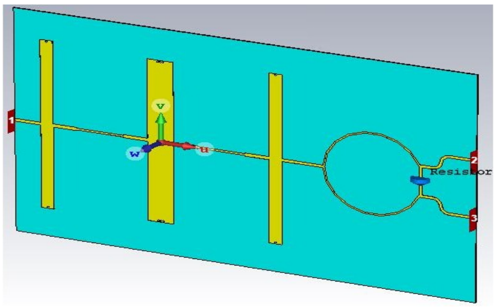

Figure 5.17: CST model of the quarter-wavelength stub filter and Wilkison power divider integrated onto a single structure. The IF signal arriving at port 1 is filtered and then equally split between output ports 2 and 3.

mately 0.029 GHz. Attempts were made at improving these, however, due to limited computational resources, this deviation could not be resolved by the optimisation tool. Nonetheless, this was still tolerable as S_{11} did not deviate by more than 1.7 dB (maximum S_{11} of -8.3 dB) at 1.094 GHz from the specification.

Figure 5.16a also shows an S_{21} and S_{31} peak of -4.02 dB at 1.102 GHz, which indicated a minimum insertion loss of 1.02 dB, since the power was equally (3 dB) split between the two output ports. Considering that at this frequency the standalone hairpin filter and Wilkinson power divider had individual insertion losses of 0.8925 dB and 0.122 dB, respectively, the integrated results showed minimal additional losses attributed to the merging of the two structures. Finally, the output port phases in Figure 5.16b indicate that the output phases were identical and remained linear over the passband, as required.

5.3.2.2 Quarter-wavelength Stub Filter and Wilkinson Power Divider Integration

Integrating the Wilkinson power divider onto the quarter-wavelength stub filter as shown in Figure 5.17 resulted in a noticeably large PCB due to the quarter-wavelength microstrip lengths present in both the filter and power divider structures. As these lengths were dominant characteristics, there were limited layout options which could optimise board space without sacrificing performance. Thus, the final optimised board area was 174.14 mm x 102.65 mm, which was more than double the area of the integrated hairpin filter and Wilkinson power divider model in Figure 5.15.

The integrated results shown in Figure 5.18 showed minimal passband losses along with strong stopband suppresion, similar to the performance of the standalone stub filter. Thus, there was no noticeable deterioration in the overall filter performance as a result of the integrated power divider.

Based on the - 10 dB S_{11} points shown in Figure 5.18a, this integrated design offered a 0.14 GHz bandwidth centred at 1.106 GHz. While this was 0.04 GHz larger than the specification, it was still acceptable as it was

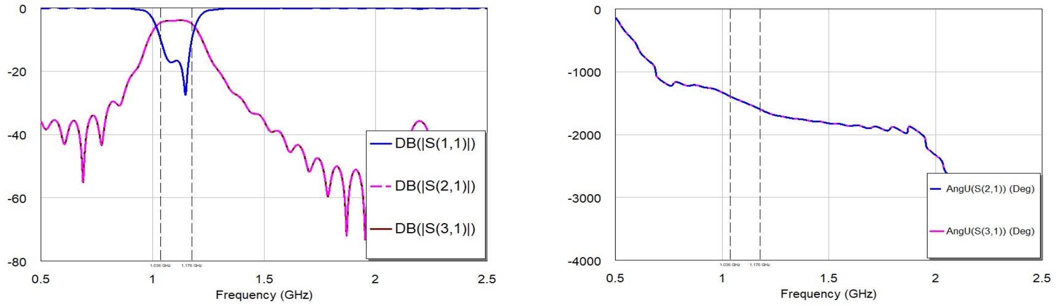

(a) S-parameter amplitudes.

(b) Output ports' S-parameter phases.

Figure 5.18: S-parameter amplitudes and phases of the integrated quarter-wavelength stub filter and Wilkinson power divider structure shown in Figure 5.17.

still centred close to the specified frequency and more importantly, it was still well above the LNB lower cut-off frequency. Furthermore, the return loss remained well below 10 dB for this entire band, while spurious passbands were suppressed till at least 2.5 GHz.

The simulated results also showed that the amplitude of output ports (S_{21} and S_{31}) were identical and achieved a a peak of - 3.969 dB at 1.091 GHz - this indicated an insertion loss of 0.969 dB. At this frequency, the standalone quarter-wavelength stub filter and Wilkinson power divider showed an insertion loss of 0.777 dB and 0.123 dB, respectively, thus minimal insertion loss was attributed to the merging of these two structures. The output port phases shown in Figure 5.18b were identical and remained linear over the 0.14 GHz bandwidth.

The results from Sections 5.3.2.1 and 5.3.2.2 indicates that integrated filter and power divider structures performed correctly with minimal losses and amplitude imbalance. The benefit of this would be more prominent in the physical implementation, as it would assist in reducing the overall complexity and connector losses.

5.4 IN-PHASE AND QUADRATURE SIGNAL SEPARATION

As per Figure 5.2, the IF signal of one of the LNBs needed to be separated into two parts of equal amplitude, but with a phase imbalance of 90°. A suitable solution to this was the branchline coupler.

5.4.1 Standard Branchline Coupler

The conventional branchline coupler such as the designed CST model shown Figure 5.19 is a four-port device which separates the signal present at port 1 equally (amplitude) between output port 2 and output port 3. Thus, the output signal amplitudes are ideally 3 dB (half-power) below the input signal amplitude. Furthermore, the two outputs signals have a phase-difference of 90° [14]. All ports are matched to Z_0, while the main structure makes use of quarter-wavelength transmission lines of 0.7071 Z_0 and Z_0, as per Figure 5.19. Port 4, referred to as the isolation port, prevents direct transmission between port 2 and port 3, and is further isolated from port 1. A derivation of the even-odd mode analysis of this structure can be found in [14].

The use of quarter-wavelength transmission lines indicated that the branchline coupler was better suited for narrowband purposes. The IF filters previously discussed in Section 5.2 were designed for a centre frequency of 1.10 GHz and 0.1 GHz bandiwidth. Consequently, the filtered signal would be narrowband with an FBW of 0.091, thus, the standard branchline coupler could be used.

The two outputs were required to have an equal amplitude with a 90° phase shift at 1.10 GHz, but more importantly, do so with little variation over the entire 0.10 GHz band. This meant that the performance near the lower cut-off frequency (1.05 GHz) should closely match the performance at the upper cut-off frequency (1.15 GHz). In order to determine how well this narrowband branchline coupler met this criteria, its performance was compared to the Mini-Circuits ZX10Q-2-13-S+ [44] quadrature hybrid, which had a rated operating band between 0.675 - 1.3 GHz. This comparison is shown in Figure 5.20 and Tables 5.5 and 5.6.

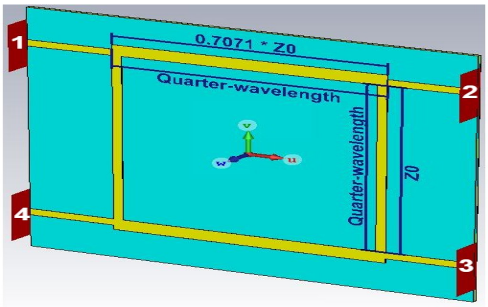

Figure 5.19: CST model of the branchline coupler. The input signal at port 1 was equally split between the output ports 2 and 3 along with a 90° phase imbalance. Port 4 served as an isolation port which minimised transmission between port 2 and port 3.

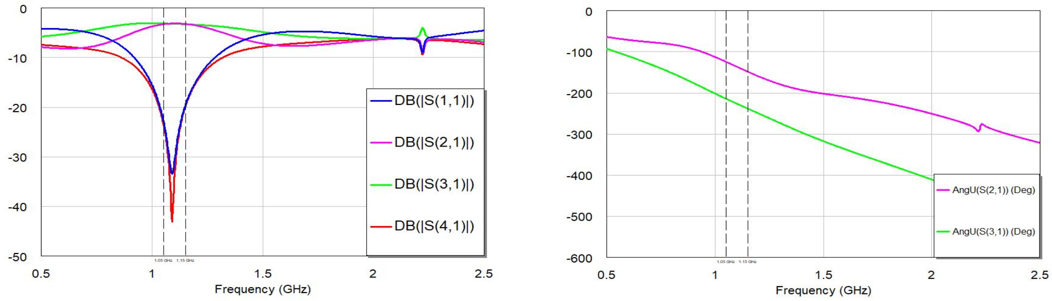

(a) S-parameter amplitude of the 1.1 GHz narrowband branchline coupler.

(b) Output ports' S-parameter phases of the 1.1 GHz narrowband branchline coupler.

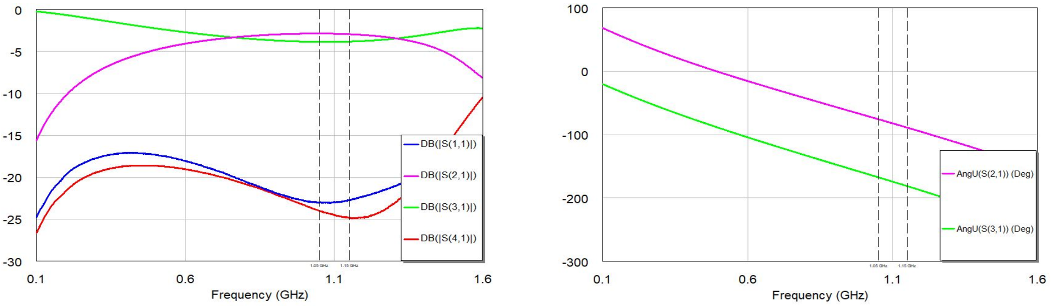

(c) S-parameter amplitude of the Mini-Circuits ZX10Q-2-13-S+.

(d) Output ports' S-parameter phases of the Mini-Circuits ZX10Q-2-13-S+.

Figure 5.20: Comparison of the S-parameter amplitudes and phases of the 1.10 GHz narrowband branchline coupler to the Mini-Circuits ZX10Q-2-13-S+.

Table 5.5: Output port S-parameter amplitudes comparing the performance of the simulated branchline coupler to the Mini-Circuits ZX10Q-2-13-S+.

	S_{21} (dB)			S_{31} (dB)			Imbalance (dB)		
	1.05 GHz	1.1 GHz	1.15 GHz	1.05 GHz	1.1 GHz	1.15 GHz	1.05 GHz	1.1 GHz	1.15 GHz
Simulation	-3.28	-3.11	-3.20	-3.10	-3.19	-3.28	0.18	0.08	0.08
Mini-Circuits	-2.86	-2.88	-2.94	-3.86	-3.86	-3.82	1.00	0.98	0.92

Table 5.6: Output port S-parameter phases comparing the performance of the simulated branchline coupler to the Mini-Circuits ZX10Q-2-13-S+

	S_{21} (°)			S_{31} (°)			Imbalance (°)		
	1.05 GHz	1.1 GHz	1.15 GHz	1.05 GHz	1.1 GHz	1.15 GHz	1.05 GHz	1.1 GHz	1.15 GHz
Simulation	-124.2	-136.3	-148.3	-214.1	-226.2	-238	89.9	89.9	89.
Mini-Circuits	-75.6	-82.2	-88.9	-167.3	-174.2	-181.2	91.7	92	92.3

A Steep decline was seen in both S_{11} and S_{41} of the simulated device towards 1.10 GHz which indicated minimal return loss and strong isolation between port 1 and 4, respectively. Furthermore, the return loss remained below 20 dB for the entire 0.10 GHz bandwidth. In observing the Mini-circuits performance in Figure 5.20c, return loss remained below 15 dB for its entire rated bandwidth.

As per Figure 5.20a, the amplitude of branchline coupler's S_{21} and S_{31} response merged toward one another and remained stable over the 0.1 GHz bandwidth. As there were no sudden changes in the amplitude nor phase, this was better depicted in Table 5.5 and 5.6 which showed the performance at 1.05 GHz, 1.1 GHz, and 1.15 GHz.

The maximum amplitude imbalance between output ports at a given frequency was 0.18 dB and the maximum amplitude variation over the frequency band was also 0.18 dB; furthermore, insertion losses remained below 0.3 dB.

Figure 5.20b also shows that the output port phases remained linear over the 0.1 GHz bandwidth, with no sudden changes. Examining this closer in Table 5.6 revealed that the output ports closely met the 90° phase specification, with a maximum variation of 0.3° from this target.

As the Mini-Circuits equivalent was more suited for a wider operating band, it was unable to provide superior performance specifically at 1.10 GHz. Figure 5.20c shows that the amplitude of the Mini-Circuits component flattens near the 1.1 GHz band. However, there remained a large amplitude imbalance, which at some frequencies reached 1.00 dB. These results further indicate that the input power is not equally split between the output ports as S_{21} was greater than - 3 dB, while S_{31} was less than -3dB (without accounting for losses).

Examining the Mini-Circuit's output phase response in Figure 5.20d and Table 5.6 once again indicated it was better suited for a larger operating band, as the phase remains almost linear even beyond its rated frequency. It also showed less than 3° variation from the 90° phase specification.

In comparing the CST model branchline coupler to the Mini-Circuits equivalent, it was evident that the simulated performance showed desirable attributes in both amplitude balance and phase imbalance. Additionally, it outperformed the Mini-Circuits equivalent in both these areas, mainly due to Mini-Circuit's larger operating band.

Most importantly, these simulated results indicated that a branchline coupler was a feasible solution to separate the 1.05 GHz - 1.15 GHz band into its I-Q components with minimal variation in performance over this band. This reduced the overall complexity, loss, and cost of the entire system, as no heterodyne network was needed.

5.4.2 Integrated Filter and Branchline Coupler

The technique of using a standard branchline coupler to directly separate the IF signals into I-Q components was only possible for narrowband operation, which the standard LNB was not. This implied that the previously designed hairpin and quarter-wavelength stub filters would once again be necessary. It was decided to investigate integrating a branchline coupler onto each of the IF filters, for reasons (minimise cost, loss, and imbalance) similar to merging the filter and Wilkinson power dividers onto a single PCB.

5.4.2.1 Hairpin Filter and Branchline Coupler

Figure 5.21 shows the CST model of the hairpin filter and branchline coupler integrated onto a single PCB. The individual optimised models were merged and were again optimised using the Trust Region Framework. Due to the significantly larger structure of the branchline coupler, specifically at this frequency, the integrated PCB occupied an area of 114.16 mm x 77.75 mm.

The simulated results shown in Figure 5.22 indicate that integrating these two structures did not result in noticeable deterioration in neither filtering nor phase-shifting performance. Observing S_{11} in Figure 5.22a, specifically the -10 dB points, indicated a slightly negligible increase in bandwidth to 0.104 GHz centred on 1.099 GHz. This neglected the rise in S_{11} between 1.083 GHz - 1.116 GHz, however, this rise did not exceed - 8.312 dB. This trait (rise in S_{11}) has previously been present in other instances of the hairpin of filter, however it had been reduced

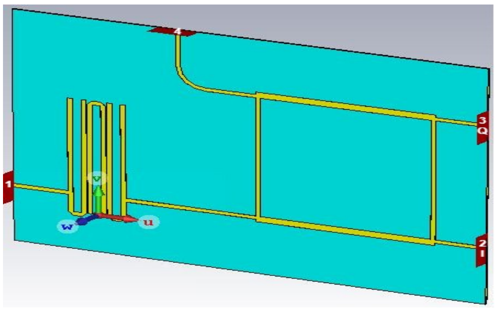

Figure 5.21: CST model of the haripin filter and branchline coupler integrated onto a single PCB.

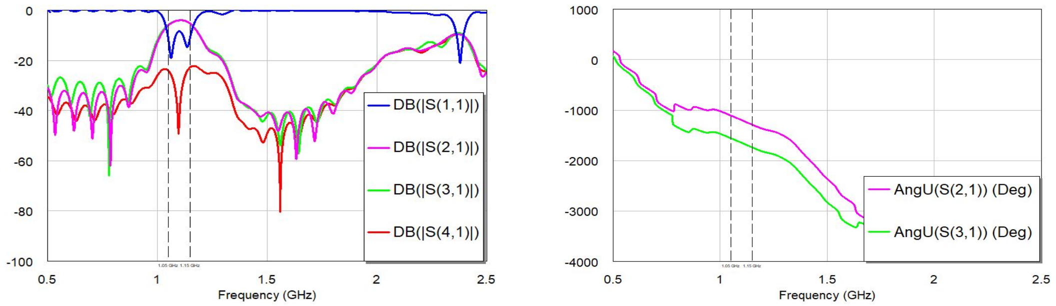

(a) S-parameter amplitudes of all four ports.

(b) Output ports' S-parameter phases.

Figure 5.22: S-parameter amplitudes and phases of the integrated hairpin filter and branchline coupler.

Table 5.7: Amplitude and phase imbalance between the two output ports of the haipin filter and branchline coupler integrated onto a single PCB. The phases shown take into account that port 3 leads port 2 by a single cycle.

	S_{21}			S_{31}			Imbalance		
	1.05 GHz	1.1 GHz	1.15 GHz	1.05 GHz	1.1 GHz	1.15 GHz	1.05 GHz	1.1 GHz	1.15 GHz
Amplitude	-5.90 dB	-3.96 dB	-5.39 dB	-5.68 dB	-3.94 dB	-5.38 dB	0.22 dB	0.02 dB	0.01 dB
Phase	-25.9°	-115.7°	152.2°	-115.6°	154.7°	61.9°	89.7°	89.6°	90.3°

through optimisation. Unfortunately, this was not accomplished in this integrated design.

Table 5.7 focuses on S_{21} and S_{31}, which shows that the output amplitudes strongly agreed with one another indicating minimal amplitude imbalance. There was a minor imbalance in amplitude, no more than 0.241 dB, near the lower cut-off frequency, however, this reduced throughout the remainder of the band. In observing the phase, it was evident that the two output port phases followed a linear trajectory and the phase imbalance remained within 0.5° of the 90° specification.

Furthermore, there was a peak in output amplitude of - 3.913 dB near the centre of the band, which indicated insertion losses of 0.913 dB. Comparing this insertion losses to the standalone hairpin filter (0.876 dB) and the branchline coupler (0.108 dB), indicated that the integrated design already offered lower insertion loss even without accounting for additional connector losses, which the standalone configuration would experience.

5.4.2.2 Quarter-wavelength Stub Filter and Branchline Coupler

Figure 5.23 shows the CST model of the quarter-wavelength stub filter and narrowband branchline coupler integrated onto a singe PCB structure. The integrated structure was optimised, in particular the microstrip transmission line joining the two structures, in order to minimise mismatch and consequently improve return loss. The overall structure of 192.29 mm x 109.1 mm was noticeably larger than all the other structures previously discussed, due to the large, straight/non-curved individual structures.

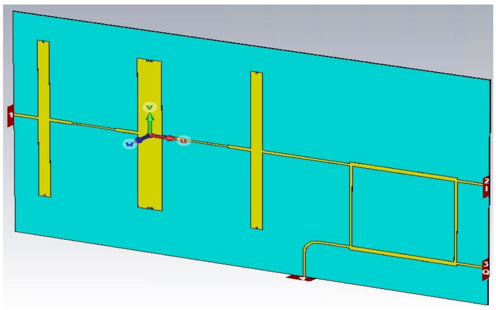

Figure 5.23: CST model of the quarter-wavelength stub filter and branchline coupler integrated onto a single PCB.

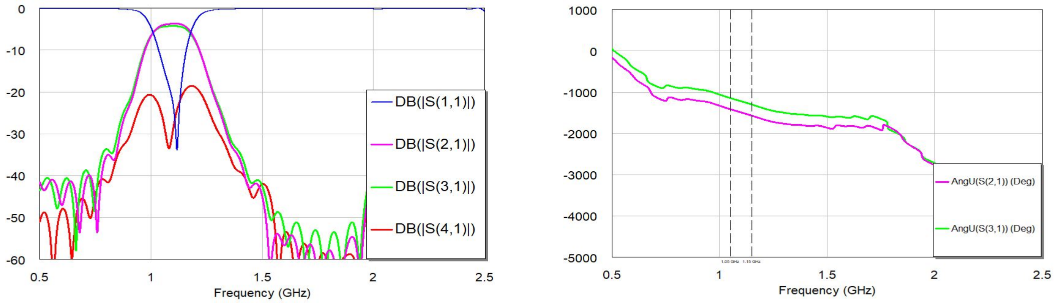

(a) S-parameter amplitudes of all four ports.

(b) Output ports' S-parameter phases.

Figure 5.24: S-parameter amplitudes and phases of the integrated quarter-wavelength stub filter and branchline coupler shown in Figure 5.23.

Table 5.8: amplitude and phase imbalance between the two output ports of the quarter-wavelength stub filter and branchline coupler integrated onto a single PCB. The phases shown take into account that port 3 leads port 2 by a single cycle.

	S_{21}			S_{31}			Imbalance		
	1.05 GHz	1.1 GHz	1.15 GHz	1.05 GHz	1.1 GHz	1.15 GHz	1.05 GHz	1.1 GHz	1.15 GHz
Amplitude	-4.12 dB	-3.72 dB	-4.21 dB	-4.45 dB	-4.28 dB	-4.73 dB	0.33 dB	0.56 dB	0.52 dB
Phase	28.0°	-48.8°	-127.8°	-62.1°	-138.6°	142.7°	90.1°	89.8°	89.5°

The results of the integrated quarter-wavelength stub filter and branchline coupler, shown in Figure 5.24, outperformed the hairpin filter equivalent previously discussed. The amplitude of S_{11} in Figure 5.24a indicated a - 10 dB bandwidth of 0.125 GHz centred on 1.098 GHz. While this bandwidth was slightly larger than specification, it still included both cut-off frequencies. More noticeable was the smoother trajectory of S_{11} which reached a minimum of -33.87 dB at 1.12 GHz. There were no spurious passbands up to at least 2.5 GHz, indicating strong suppression of the remainder of the LNB passband.

The output port amplitudes closely tracked one another as shown in both Figure 5.24a and Table 5.8, with less than 0.6 dB amplitude imbalance - this was noticeably larger than the hairpin filter equivalent (less than 0.25 dB imbalance). However, the stub filter equivalent achieved a peak amplitude of -3.71 dB, which was 0.20 dB greater than the hairpin filter equivalent. Furthermore, the stub filter equivalent showed a minimum insertion loss of 0.71 dB, which was 0.14 dB less than the sum of its individual structure losses. The output phases were also linear with respect to frequency throughout the operating band and remained within 0.5° of the 90° phase specification.

The simulated results of the standalone 1.10 GHz branchline coupler as well as having it integrated onto each of the hairpin and quarter-wavelength stub filters, indicated that this technique was a viable alternative to a quadrature down-conversion network. This alternative reduces system cost, losses, and complexity with no obvious degradation in performance.

5.5 CHAPTER SUMMARY

This chapter focused on the network of PCBs required to separate the LNBs' IF signals into its I-Q components. Two architectures were explored namely, using a superheterodyne network in which the LO was separated into its I-Q components, or directly separating the IF signals into I-Q components. The latter option was chosen based on its simpler architecture as well as its successful simulated results. This option largely relied on the narrowband configuation of the system, which allowed it to make use of structures such as Wilkinson power dividers and branchline couplers.

This chapter also discussed the design of IF filters which were required to improve the interferometer's resolution as well as remove the spurious LO leakage present in the modified LNBs. Third-order narrowband hairpin and quarter-wavelength stub filters were designed to achieve this. Multiple integrated structures were also developed alongside these individual structures to minimise complexity and losses. All of these PCB designs were optimised for manufacturing on 0.508 mm Mercurywave substrate. The next chapter focuses on the measurement of these PCBs, which will further be compared to their corresponding simulations.

CHAPTER 6

MANUFACTURED PCB MEASUREMENTS

The previous chapters identified the limitations of satellite TV equipment and the issues introduced by the LNB modifications. This led to the design of specialised PCBs capable of suppressing undesired signals along with separating signals into I-Q components. The PCBs capable of separating signals into I-Q components were responsible for fulfilling the user requirement of performing complex correlation, as discussed in Chapter 3.

These PCBs were manufactured locally, and the completed PCB panel is shown in Figure 6.1. This chapter discusses the measured performance of the manufactured PCBs required for the direct separation of signals into I-Q components. Measurements of the superheterodyne PCBs are included in Appendix C. The manufactured PCBs were all measured using the Agilent N5247A PNA-X Network Analyser. All four pouts of this Vector Network Analyser (VNA) were calibrated using the Agilent N4694-60001 Electronic Calibration (ECal) module.

6.1 IF FILTER MEASUREMENTS

Two IF filters were designed, namely the hairpin filter and quarter-wavelength stub filter. These were designed to improve the interferometer's resolution and importantly to suppress the spurious LO signal near 0.8475 GHz. These filters were also designed to suppress the LO leakage and the image band of the superheterodyne receiver (alternative I-Q separation network) as discussed in Appendix B.

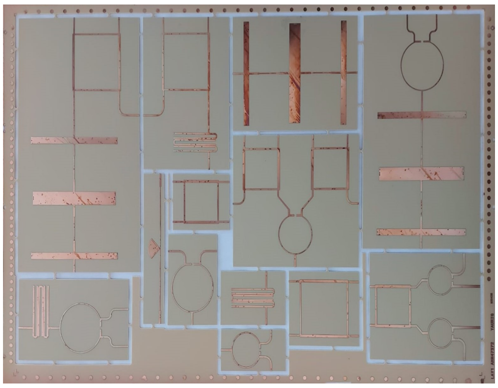

Figure 6.1: Manufactured PCB panel comprised of filters, power dividers, and couplers. The 275 mm x 427 mm panel was manufactured locally by Trax Interconnect using 0.508 mm Mercurywave substrate.

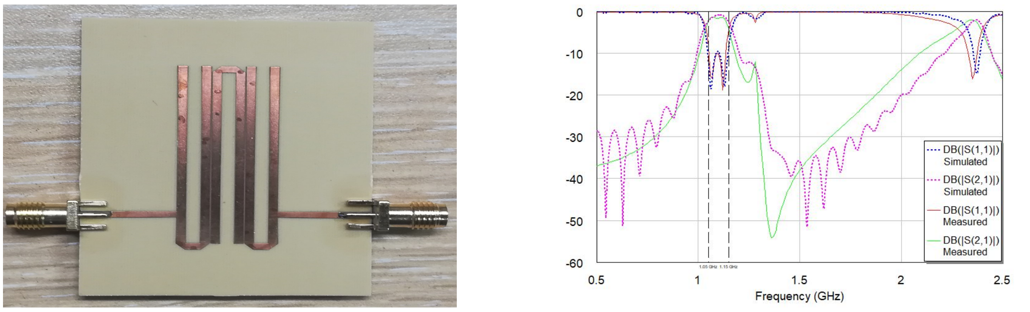

(a) Manufactured hairpin filter.

(b) S-parameter comparison between the simulated and measured filter performance.

Figure 6.2: Manufactured hairpin filter and corresponding S-parameter amplitudes.

Table 6.1: S-parameter comparison between the simulated and measured performance of the hairpin filter.

	S11 (dB)			S21 (dB)		
	1.05 GHz	1.10 GHz	1.15 GHz	1.05 GHz	1.10 GHz	1.15 GHz
Simulated	-10.90	-9.68	-9.14	-2.42	-0.91	-2.53
Measured	-8.45	-10.17	-4.46	-2.24	-1.63	-4.21

6.1.1 **Hairpin Filter**

The simulated hairpin filter offered a narrow passband and physically compact structure. The corresponding manufactured hairpin filter along with its SMA connectors are shown in Figure 6.2a, while Figure 6.2b and Table 6.1 compares the measured hairpin PCB performance to its previously simulated results.

Figure 6.2b indicate that the manufactured filter closely resembled the simulated performance with a visible passband near 1.10 GHz along with a spurious passband near 2.35 GHz. The measured filter showed adequate suppression of the image frequency between 1.85 GHz - 1.95 GHz, should the alternative superheterodyne network be used. As expected, the manufactured filter also showed an increase in insertion loss of approximately 0.5 dB relative to the simulation.

The manufactured filter offered a slightly narrower passband (based on the 10 dB return loss points) of 0.085 GHz compared to the simulated 0.100 GHz bandwidth; the measured filter also showed a negligible shift in centre frequency to 1.095 GHz compared to the simulated 1.098 GHz. Furthermore, the measured result indicated that the return loss remained below 10 dB for the entire passband. Regardless of this, these results indicated that the manufactured hairpin filter closely fulfilled the initial filter specifications.

6.1.2 **Quarter-wavelength Stub Filter**

The quarter-wavelength stub filter was designed to overcome the spurious passband limitations of the hairpin filter. This came with a trade-off in being a physically larger PCB as per Figure 6.3a. There was a strong agreement between the manufactured filter's performance and simulated performance as per Figure 6.3b and Table 6.2. The manufactured PCB had a slightly larger bandwidth of 0.134 GHz compared to the simulated bandwidth of 0.128 GHz, however, as the former also showed a slight shift in frequency, it (manufactured filter) was centred at 1.102 GHz - this agreed precisely with the initial filter specification.

There was also a remarkable agreement in passband insertion loss between the measured and simulated filters; the former showed less than 0.2 dB increase in insertion loss compared to the latter. The measured passband return loss showed no sudden fluctuations and achieved a minimum 29.69 dB near 1.14 GHz. Also of note was the strong suppression of spurious signals to well above 2.5 GHz for both the measured and simulated performances. This result indicated that the manufactured filter closely fulfilled the filter specifications and showed a remarkable agreement to its simulated performance.

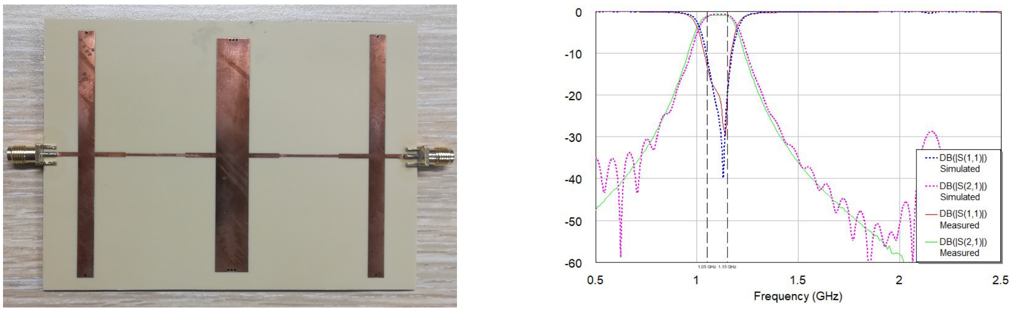

(a) Manufactured quarter-wavelength stub filter.

(b) S-parameter comparison between the simulated and measured filter performance.

Figure 6.3: Manufactured quarter-wavelength stub filter and corresponding S-parameter amplitudes.

Table 6.2: S-parameter comparison between the simulated and measured performance of the quarter-wavelength stub filter.

	S11 (dB)			S21 (dB)		
	1.05 GHz	1.10 GHz	1.15 GHz	1.05 GHz	1.10 GHz	1.15 GHz
Simulated	-10.70	-23.29	-20.49	-1.41	-0.75	-0.89
Measured	-13.28	-19.26	-19.58	-1.17	-0.92	-1.08

6.1.3 **Filtered LNB Performance**

An important function of the filters was to remove the LO leakage near 0.8475 GHz, which had previously distorted initial observations of the sun. The effectiveness of each filter was evaluated by connecting each filter to the modified LNB and observing the output spectrum between DC - 3 GHz. The equipment setup was shown in Figure 6.4, while the corresponding observed results are shown in Figure 6.5.

The results shown in Figure 6.5 indicated that both filters had drastically reduced the effects of the LO leakage. Although the spurious LO signal was not entirely removed (as it was relatively close to the passband and neither filters offered sufficient roll-off since these were only third-order filters), it had significantly been attenuated. Previously, the LO leakage was approximately - 21 dBm, however, with the introduction of either of the filters, this had been reduced to approximately - 40 dBm. This greatly improved drift-scan observations of the sun, as discussed in Chapter 7.

However, the hairpin filter did not provide sufficient suppression of the remainder of the LNBs passband. This was due to its (hairpin filter) inherent harmonic passband, which would introduce ambiguities in the measured fringe phase. Furthermore, the hairpin filter would not adequately suppress the image band in the case of the

(a) Hairpin filter and modified LNB

(b) Quarter-wavelength stub filter and modified LNB

Figure 6.4: Equipment setup to observe the performance of the modified LNB with each of the manufactured filters.

(a) Hairpin filter and modified LNB

(b) Quarter-wavelength stub filter and modified LNB

Figure 6.5: Observed spectrum of the modified LNB with each of the manufactured filters. The LO leakage has been drastically reduced as a result of either of the filters, however the hairpin filter's prominent second harmonic passband may be susceptible to spurious signals within the LNB's passband.

superheterodyne receiver. Contrary to this, the quarter-wavelength stub filter did not suffer from such issues, as its spurious passband was above 3 GHz. As a result of this, the quarter-wavelength stub filter and its its corresponding integrated designs were selected for drift-scan observations of the sun, as discussed in Chapter 7.

6.2 IN-PHASE SIGNAL SEPARATION

As previously discussed, one of the LNB's IF signals was required to be separated into two in-phase outputs (ideally with identical amplitude and no phase imbalance). This was addressed by the design of Wilkinson power dividers centred at 1.1 GHz for narrowband operation. This section discusses the measured performance of the manufactured Wilkinson power dividers.

6.2.1 Standard Wilkinson Power Divider

The manufactured standard Wilkinson power divider (without any integrated filtering) designed for narrowband functionality is shown in Figure 6.6. The manufactured Wilkinson power divider included SMA connectors as well as a 100 Ω 0805 SMD resistor.

The earlier shown simulation of the standard Wilkinson power divider showed excellent amplitude and phase balance over the operating band, hereby justifying its manufacture - these were then compared to the measured results as shown in Figure 6.7.

As evident by the S-parameter amplitudes, there was a strong resemblance in performance between the measured and simulated results. A steep decline in return loss occurred near the specified bandwidth which reached a minimum of 33.4 dB at 1.07 GHz. While this occurred at a slightly lower frequency compared to the simulations, the measured results showed greater than 8 dB improvement in return loss compared to the simulation. An almost

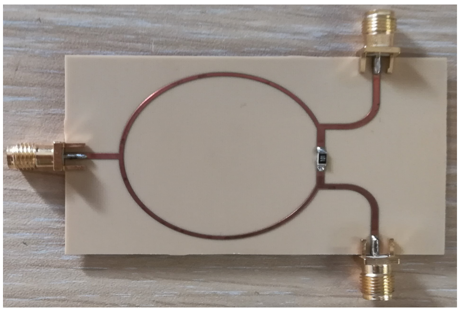

Figure 6.6: Manufactured standard Wilkinson power divider, which includes SMA connectors and a 100 Ω 0805 SMD resistor

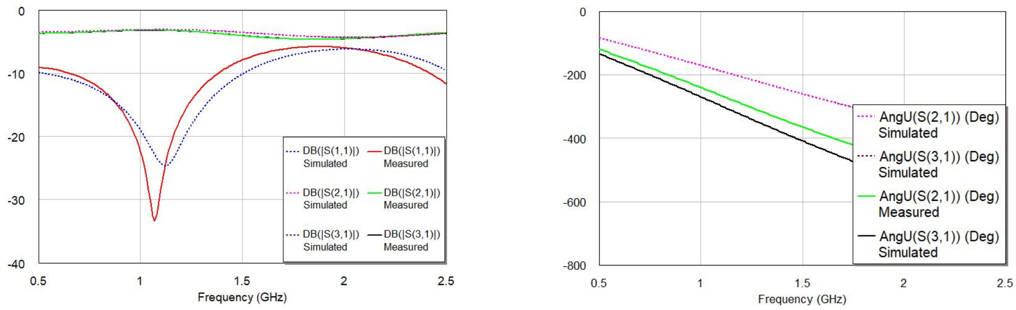

(a) Amplitude imbalance

(b) Phase imbalance

Figure 6.7: S-parameter amplitude and phase imbalance of the measured Wilkinson power divider compared to its simulated performance.

Table 6.3: Summarised S-parameter amplitude and phase imbalance of the measured Wilkinson power divider compared to the simulated performance.

	Amplitude Imbalance (dB)			Phase Imbalance (°)		
	1.05 GHz	1.10 GHz	1.15 GHz	1.05 GHz	1.10 GHz	1.15 GHz
Simulated	0	0	0	0	0	0
Measured	0.038	0.036	0.03	30.8	32.3	33.7

identical performance between simulation and measurement was found in terms of insertion loss. The measured insertion loss remains below 0.25 dB throughout the band, which was less than 0.12 dB greater than the simulated result.

The output phases indicated a linear response throughout the band with no unexpected fluctuations, however, what was of concern was the large phase imbalance/ error between the two outputs. This is more clearly demonstrated by Table 6.3.

These results indicated that although there was an almost perfect balance in amplitude, there was a significant phase imbalance in excess of 30°. This phase imbalance continues to increase at higher frequencies. This result resembled the issue identified earlier: during the initial simulations and optimisations, excellent amplitude balance could be achieved, however at the expense of a large phase imbalance. Furthermore, these results indicated that the manufactured Wilkinson power divider would not be capable of performing its task required by the complex correlator.

A similar phase discrepancy was also observed for the manufactured 1.5 GHz Wilkinson power divider which formed part of the superheterodyne alternative discussed in Appendix B. As both designs shared similar structures, this similarity in performance indicated that the likely cause of the imbalance may be as a result of incomplete optimisation. Due to time constraints, these PCBs could not be redesigned and manufactured.

However, this did not hinder completion of the complex correlator: the corresponding integrated designs (discussed below) showed favourable measured results and could thus replace the standalone Wilkinson power divider. This was not an anticipated benefit of having integrated designs, but its presence prevented any further delays during the project.

In comparing the structures of the standard Wilkinson power divider (Figure 6.6) to the integrated structures (Figure 6.8 and Figure 6.10), the main difference in the power divider structures was the transition from circular transmission lines to the curved output ports. For the case of the standard Wilkinson power divider, the output ports were closely spaced to the circular transmission lines, which may have resulted in undesired coupling, and consequently the large phase imbalance - this issue was not present during the simulation process.

While the Wilkinson power divider suffered from undesirably large phase imbalance, all analogue I-I and I-Q

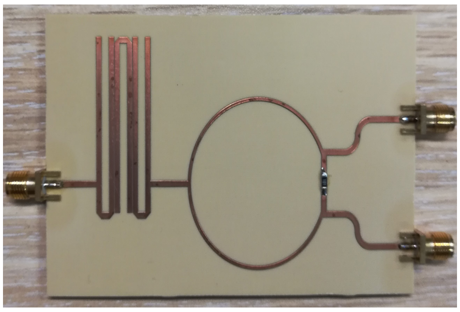

Figure 6.8: Manufactured integrated hairpin filter and Wilkinson power divider.

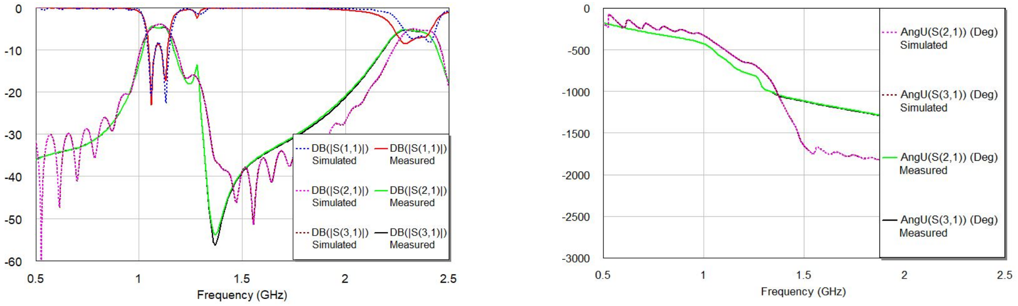

(a) Amplitude imbalance

(b) Phase imbalance

Figure 6.9: S-parameter amplitude and phase imbalance of the measured integrated hairpin and Wilkinson power divider compared to the simulated performance.

separators will suffer from at least minute amplitude and phase imbalance, the extent of this imbalance is largely dependent on the operating frequency along with manufacturing capabilities and precision. To overcome these challenges, many systems which rely on analogue I-I and I-Q separation compensate for these errors in the digital domain after having sampled the signals as described in [45, 46].

6.2.2 Hairpin Filter and Wilkinson Power Divider

The first integrated PCB comprised of the hairpin filter and Wilkinson power divider - the former would ensure that the system was narrowband, thus allowing the use of the latter. The manufactured equivalent is presented in Figure 6.8.

Through observation of the S-parameters in Figure 6.9, in particular the amplitudes, it was evident that there was a strong agreement between the measured and simulated results. Furthermore, the behaviour of this integrated PCB closely resembled that of the standard hairpin filter, indicating that the integrated design's amplitude response was strongly governed by the filter response, as desired.

A negligible shift in frequency and improvement in return loss was observed for the measured PCB compared to the simulated result. The measured result also showed a 0.093 GHz bandwidth, which was 0.01 GHz narrower than the simulated result. The former showed steeper roll-off near the band edges, but this was accompanied by an in increase in passband ripple and insertion loss of 1.46 dB. This was 0.45 dB greater than the latter's insertion loss, which is typically expected. Both results also indicate a prominent spurious passband near 2.2 GHz.

Regardless of this, excellent amplitude balance was achieved between outputs as summarised by Table 6.4 - at a given frequency, the amplitude imbalance between outputs remained within 0.06 dB. As also indicated by Figure 6.9b, the measured output ports showed a liner phase response over the narrowband. More importantly, the phase of these output were almost indistinguishable from one another, with an imbalance no greater than 0.4°, which was only 0.1° greater than that of the simulation. These results indicated that this integrated design was capable of filtering and separating the input signal with minimal amplitude and phase imbalance.

Table 6.4: Summarised S-parameter amplitude and phase imbalance of the measured integrated hairpin filter and Wilkinson power divider compared to the simulated performance.

	Amplitude Imbalance (dB)			Phase Imbalance (°)		
	1.05 GHz	1.10 GHz	1.15 GHz	1.05 GHz	1.10 GHz	1.15 GHz
Simulated	0.01	0.01	0.02	0.3	0.2	0.2
Measured	0.05	0.06	0.04	0.4	0.3	0.3

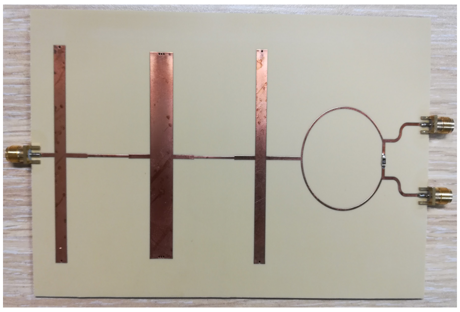

Figure 6.10: Manufactured integrated quarter-wavelength stub filter and Wilkinson power divider.

6.2.3 Quarter-wavelength Stub Filter and Wilkinson Power Divider

The following integrated design instead made use of the quarter-wavelength stub filter, as shown in Figure 6.10. The corresponding results shown in Figure 6.11 indicated a strong agreement between simulation and measurement. The measured results also showed an improvement in return loss (relative to simulation) which showed a minimum of 33.49 dB near 1.14 GHz, a shift in frequency of approximately 0.01 GHz relative to the simulated minimum of 27.53 dB. These results also indicated that the measured PCB occupied a negligibly wider passband of 0.144 GHz compared to the simulated 0.140 GHz.

Impressively, the measured result showed an insertion loss ranging between 0.93 dB - 1.23 dB which was an improvement compared to the simulated 0.96 dB - 1.25 dB loss. The summarised output imbalance per Table 6.5 indicated that the measured amplitude imbalance was less than 0.14 dB, while the phase imbalance was less than 1°. While this measured imbalance was larger than the simulated results, it was still a significant improvement compared to the standard Wilkinson power divider previously discussed.

6.3 IN-PHASE AND QUADRATURE PHASE SIGNAL SEPARATION

This section discusses the measured results of the standard branchline coupler followed by the integrated filter implementations.

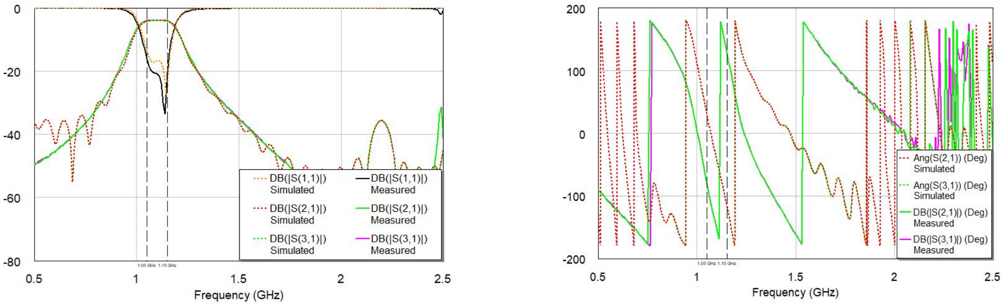

(a) Amplitude imbalance

(b) Phase imbalance

Figure 6.11: S-parameter amplitude and phase imbalance of the measured integrated quarter-wavelength stub filter and Wilkinson power divider compared to the simulated performance.

Table 6.5: Summarised S-parameter amplitude and phase imbalance of the measured integrated quarter-wavelength stub filter and Wilkinson power divider compared to the simulated performance.

	Amplitude Imbalance (dB)			Phase Imbalance (°)		
	1.05 GHz	1.10 GHz	1.15 GHz	1.05 GHz	1.10 GHz	1.15 GHz
Simulated	0	0.01	0.01	0	0	0
Measured	0.11	0.12	0.13	0.9	0.8	0.9

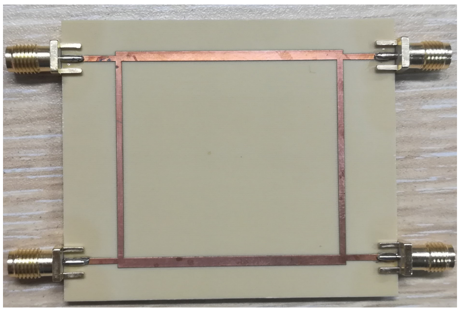

Figure 6.12: Manufactured branchline coupler.

6.3.1 Standard Branchline Coupler Measurements

The branchline coupler offered a simpler, thus a less expensive solution, compared to the superheterodyne network, to fulfil the I-Q separation requirement. Consequently, the simulated branchline coupler was manufactured and the corresponding PCB is shown in Figure 6.12.

Two vital requirements of the branchline coupler were that it should achieve minimal amplitude imbalance between output ports, along with a 90° phase imbalance between the output ports - both requirements needed to be fulfilled across the entire passband. The corresponding amplitude and phase imbalance are shown in Figure 6.13. Excellent agreement was once again observed between the measured and simulated branchline coupler. The measured branchline coupler showed a clear passband centred near 1.10 GHz along with a desirable minimum in return loss of 27.31 dB at 1.07 GHz, while the simulated result achieved a minimum return loss of 33.51 dB at 1.09 GHz. This result indicated a negligible shift of 0.02 GHz between the measured and the simulated branchline coupler. The manufactured branchline coupler also showed minimal insertion loss of 0.34 dB at 1.10 GHz compared to the simulated 0.11 dB. The measured phase of both outputs ports also showed a linear response across the 1.05 GHz - 1.15 GHz band.

Observing the summarised performance per Table 6.6 indicated an impressive performance by the manufactured branchline coupler: the amplitude imbalance across the 1.05 GHz - 1.15 GHz band was less than 0.45 dB, while

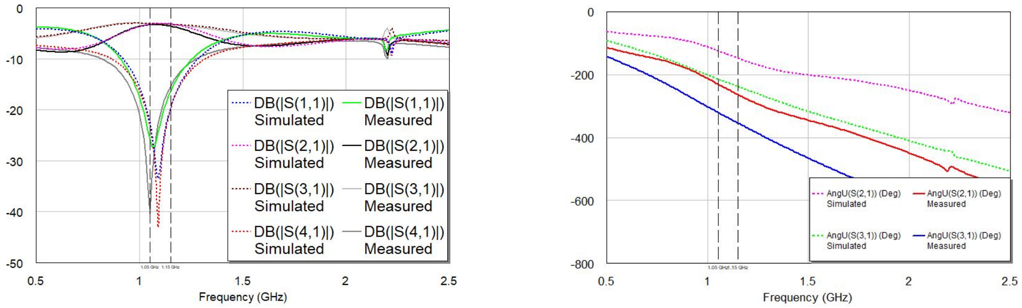

(a) Amplitude imbalance

(b) Phase imbalance

Figure 6.13: S-parameter amplitude and phase imbalance of the measured branchline coupler compared to the simulated performance.

Table 6.6: Summarised S-parameter amplitude and phase imbalance of the measured branchline coupler compared to the simulated performance.

	Amplitude Imbalance (dB)			Phase Imbalance (°)		
	1.05 GHz	1.10 GHz	1.15 GHz	1.05 GHz	1.10 GHz	1.15 GHz
Simulated	-0.179	0.078	0.078	89.9	89.9	89.7
Measured	0.177	0.067	0.22	89.9	89.4	89.5

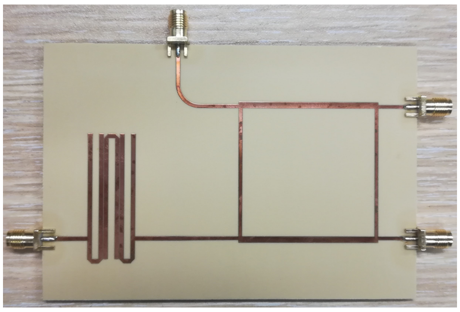

Figure 6.14: Manufactured integrated hairpin filter and branchline coupler.

the imbalance between outputs at a given frequency was less than 0.25 dB. Furthermore, the phase imbalance between output ports at a specified frequency was within 0.6° from the specified 90°. These results all verified that the manufactured branchline coupler was operating correctly and would be capable of separating signals into I-Q components required for complex correlation during the full-system testing.

6.3.2 **Hairpin Filter and Branchline Coupler**

The integration of designs was also extended to the use of branchline couplers, such as the manufactured integrated hairpin filter and branchline coupler shown in Figure 6.14. This integrated design also needed to achieve minimal amplitude imbalance, while phase imbalance should be 90° between output ports.

Comparison of the simulated and measured results indicated a strong agreement in performance, as per Figure 6.15. The amplitude response was strongly influenced by that of the standard hairpin filter, thus, the passband and spurious passband of this integrated design resembled that shown previously in Figure 6.2b. The manufactured integrated PCB showed a return loss which remained above 10 dB throughout the passband. This was an improvement compared to the simulated result which experienced an increase in return loss of 8.33 dB near 1.10 GHz. Based on the outer - 10 dB S_{11} points, the measured PCB showed a reduced passband of 0.084 GHz compared to the simulated 0.104 GHz passband. As expected, the insertion loss of the measured PCB was approximately 0.56 dB greater than the simulated result.

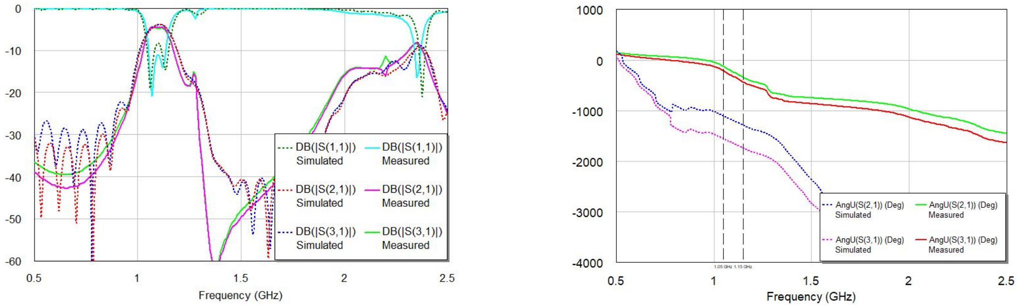

(a) Amplitude imbalance

(b) Phase imbalance

Figure 6.15: S-parameter amplitude and phase imbalance of the measured integrated hairpin filter and branchline coupler compared to the simulated performance.

Table 6.7: Summarised S-parameter amplitude and phase imbalance of the measured integrated hairpin filter and branchline coupler compared to the simulated performance.

	Amplitude Imbalance (dB)			Phase Imbalance (°)		
	1.05 GHz	1.10 GHz	1.15 GHz	1.05 GHz	1.10 GHz	1.15 GHz
Simulated	0.217	0.027	0.008	90	89	90
Measured	0.036	0.193	0.164	89.4	90.1	90.8

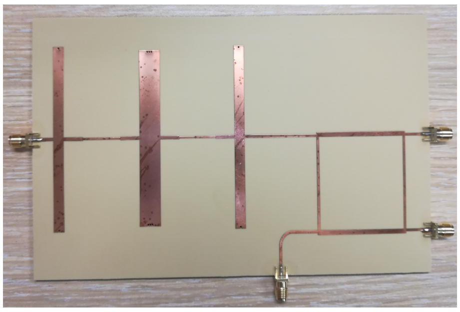

Figure 6.16: Manufactured integrated quarter-wavelength stub filter and branchline coupler.

A summarised comparison of the output ports' amplitude and phase imbalance is shown in Table 6.7. These results indicates minimal amplitude imbalance between the output ports of the measured PCB - specifically, the measured PCB offered less than 0.20 dB imbalance between output ports at a given frequency. Similarly, the phase imbalance of the measured PCB was no greater than 0.8° of the targeted 90° phase imbalance - this closely agreed with the simulated results. These results verified that this integrated PCB was capable of both filtering and separating the IF signals, however, similar to standard hairpin filter, it experienced limitations attributed to its spurious passband.

6.3.3 Quarter-wavelength Stub Filter and Branchline Coupler

The technique of integrating components onto a single PCB was also applied to the quarter-wavelength stub filter (i.e. integrating it with the branchline coupler), as shown in Figure 6.16.

An impressive agreement between the measured and simulated performance is shown in Figure 6.17; specifically, the measured S-parameter amplitudes were almost identical to those of the simulated results. The S-parameter amplitudes largely resemble that of the standard quarter-wavelength stub filter previously presented: a clear passband is present near 1.1 GHz, while harmonic passbands, and consequently spurious passbands are successfully suppressed to beyond 2.5 GHz.

The measured PCB achieved a slightly larger bandwidth of 0.151 GHz compared to the simulated bandwidth of

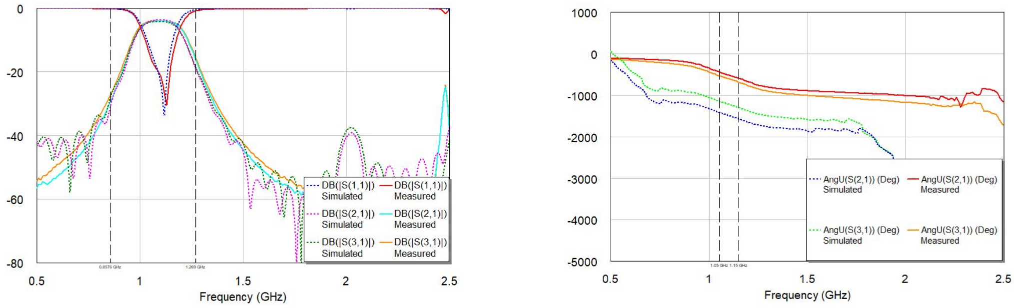

(a) Amplitude imbalance

(b) Phase imbalance

Figure 6.17: S-parameter amplitude and phase imbalance of the measured integrated quarter-wavelength stub filter and branchline coupler compared to the simulated performance.

Table 6.8: Summarised S-parameter amplitude and phase imbalance of the measured integrated quarter-wavelength stub filter and branchline coupler compared to the simulated performance.

	Amplitude Imbalance (dB)			Phase Imbalance (°)		
	1.05 GHz	1.10 GHz	1.15 GHz	1.05 GHz	1.10 GHz	1.15 GHz
Simulated	0.335	0.560	0.522	90	90	89
Measured	0.114	0.025	0.026	89.8	90.4	91.1

0.125 GHz. The former also maintained a return loss below 10 dB throughout the band and achieved a minimum return loss of 30.48 dB near 1.13 GHz. There was a negligible increase in insertion loss from 0.71 dB (simulation) to 1.08 dB (measured).

Observing the S-parameter amplitude and phase imbalance as per Table 6.8 indicated an imbalance of less than 0.12 dB between the output ports of the measured PCB - this was a noteworthy improvement in performance compared to the simulated performance. Importantly, the phase imbalance between output ports remained within 1.1° from the specified 90° - this deviates slightly from the simulation, however this was largely due to the minute shift in spectrum (to a lower frequency) in the measured result compared to the simulated result. These results, along with strong suppression of the LO leakage and second harmonic passband, indicated that this manufactured integrated PCB successfully filtered the IF signals and further separated signals into I-Q components.

As will be shown during the full-system discussion, the integrated quarter-wavelength stub filter implementations (consisting of Wilkinson power dividers and branchline couplers) were chosen over the hairpin filter equivalents. This was largely to avoid phase issues associated with the spurious second harmonic passband.

Due to the phase issues experienced with the standard Wilkinson power divider, only an integrated equivalent could be used during testing. Consequently, an integrated branchline equivalent also needed to be used.

The integrated hairpin filter equivalents (Wilkinson power divider and branchline coupler) both consisted of second harmonic spurious passbands. These spurious passbands were notably different in centre frequency and bandwidth, and did not comply with the phase requirements. The integrated hairpin filter and Wilkinson power divider maintained output port phase balance throughout the spurious passband, while the integrate hairpin filter and branchline coupler did not. This would produce inconsistencies when combined to form I-I and I-Q output pairs. The quarter-wavelength stub filter equivalents only showed a spurious third harmonic passband, which was well above the LNB passband, thus similar issues would not arise by its use.

6.4 COMPARISON TO COTS

This section compares the measured performance of the standard Wilkinson power divider and branchline coupler to their relevant Mini-circuits COTS, similar to the discussion presented in Chapter 5. As previously discussed, the onset of the SARS-CoV-2 pandemic resulted in delays and limitations on the import of COTS, which motivated the local manufacturing of RF PCBs. Due to this, this section will compare the measured PCB results to the performance provided by the manufacturer's datasheet [43, 44]. However, it is to be noted that these comparisons do not include the integrated filter designs, as comparable COTS were not available.

6.4.1 In-phase Power Signal Separation

Section 5.3 compared the Wilkinson power divider to the Mini-circuits ZAPD-2+ - the latter being a connectorized in-phase two-way power splitter operating between 1 GHz 2 GHz. It is to be noted that the Mini-circuits datasheet only provides performance figures over its specified operating band as evident in Figure 6.18, which compares both the amplitude and phase imbalance between the manufactured PCB and the Mini-circuits component.

These results indicated that the manufactured PCB achieved a return loss less than 20 dB across the 1.05 GHz –1.15 GHz band, while the Mini-circuits equivalent, achieved a return loss less than 18.57 dB. In certain regions of this band, the former's return loss outperformed that of the latter by 14.76 dB. However, in observing the output ports, the latter showed lower amplitude imbalance and insertion loss compared to the former. Specifically at 1.10 GHz,

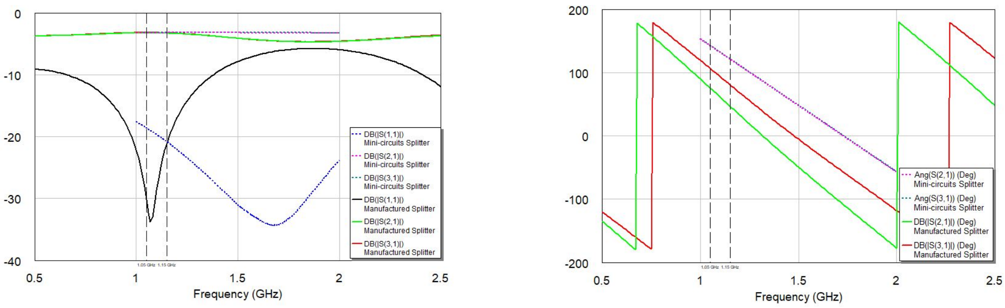

(a) S-parameter amplitudes.

(b) Output ports' S-parameter phases.

Figure 6.18: S-parameter amplitude and phase comparison of the measured Wilkinson power divider compared to the Mini-circuits ZAPD-20+

the former achieved an amplitude imbalance of 0.036 dB and an insertion loss less than 0.25 dB. The latter however, achieved an amplitude imbalance of 0.021 dB and an insertion loss less than 0.21 dB. Similarly, the Mini-circuits equivalent indicated excellent phase agreement between outputs which remained within 0.5 ° imbalance between ports. However, the manufactured PCB struggled to achieve the phase imbalance specifications as discussed in Section 6.2.1.

6.4.2 **In-phase and Quadrature Signal Separation**

Similar to the Wilkinson power divider, the branchline coupler was compared to the Mini-circuits ZX10Q-2-13-S+ which is a hybrid coupler operating between 0.68 1.30 GHz, as shown in Figure 6.19.

The manufactured PCB and Mini-circuits equivalent showed excellent return loss near the 1.05 GHz - 1.15 GHz band, both achieving below 20 dB of return loss, however, in certain regions of the band, the manufactured PCB outperformed the Mini-circuits equivalent by 6 dB in this regard. The manufactured PCB showed excellent amplitude imbalance of less than 0.22 dB, while the Mini-circuits equivalent, showed slightly poorer imbalance, in certain cases reaching an imbalance of 1 dB. The phase imbalance also indicated that the manufactured PCB outperformed the Mini-circuits device; specifically across the band, the former was within 0.5 ° of the specified 90 °, while the latter was in excess of 2.3 ° from this specification.

6.5 CHAPTER SUMMARY

This chapter focused on analysing and comparing the measured results of the various manufactured PCBs to the simulated results. A strong agreement between measured and simulated results was found among all the PCBs, except in the case of the Wilkinson power divider.

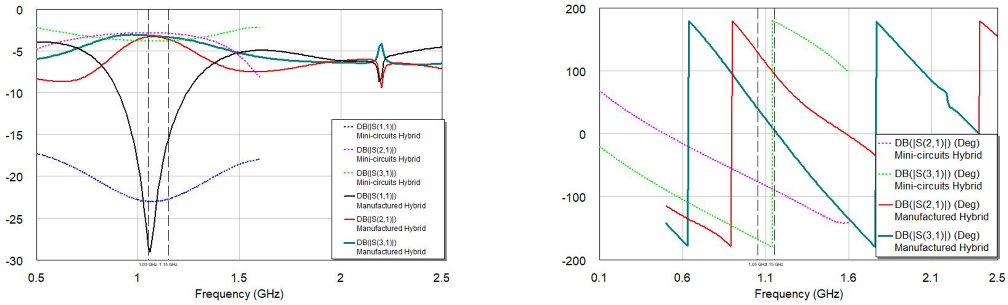

(a) S-parameter amplitudes.

(b) Output ports' S-parameter phases.

Figure 6.19: S-parameter amplitude and phase comparison of the measured branchline coupler compared to the Mini-circuits ZX10Q-2-13-S+

Measurement of the filters further indicated that the quarter-wavelength stub filter offered superior suppression compared to the hairpin filter. This was particularly noticeable when the filters were connected to the modified LNBs. As such, the quarter-wavelength stub filter along with its integrated equivalents were used during the full-system observations of the sun, as discussed in Chapter 7. Furthermore, results of the branchline coupler and consequently the integrated PCBs all indicated that the I-Q separation of signals was achieved using one of these implementations.

In ending, this chapter also compared the measured PCB results to their Mini-circuits equivalents. The results indicated that the manufactured branchline coupler outperformed the ZX10Q-2-13-S both in terms of required amplitude and phase imbalance. However, the ZAPD-2+ outperformed the manufactured Wilkinson power divider in both these specifications, more notably in terms of phase imbalance. Chapter 7 will discuss the full-system testing, however, due to the Covid-19 pandemic and subsequent inability to procure these Mini-circuits components, these full-system tests were limited to only using the manufactured PCBs.

CHAPTER 7

COMPLETE INTERFEROMETER TESTING

The initial testing of the coherent interferometer indicated that the modified LNBs were susceptible to spurious LO signals. Furthermore, I-Q separation of signals was not possible using COTS satellite TV equipment. This issue was addressed in Chapters 5 and 6 with the design and manufacturing of various PCBs.

Having successfully manufactured and measured these PCBs, attention once again shifted to observing the sun using the improved coherent two-element adding interferometer. This chapter discusses the various tests performed, which included:

- First light: successful observation of the sun using the coherent interferometer.
- Reducing the systems susceptibility to RFI.
- Resolving the sun using varied baseline.
- Estimating the system temperature.
- Full-system testing: observing the sun's cosine and sine fringes.

The previous chapters also successfully showed that the manufactured Wilkinson power dividers and branchline couplers, specifically the integrated designs, were capable of separating the LNBs' signals into I-Q components required for complex correlation.

7.1 FIRST LIGHT

The equipment configuration of the improved coherent two-element interferometer was similar to that of the previous coherent two-element interferometer, however, now included the quarter-wavelength stub filter. This removed the spurious LO signal at 0.8475 GHz and further narrowed the LNB's IF bandwidth from typically 0.950 GHz - 2.150 GHz to 1.014 GHz - 1.203 GHz. As only one standard quarter-wavelength stub filter was available, the filter was inserted between the IF combiner and power detector, which ensured that the effect of filtering applied to both modified LNBs - this setup is shown in Figure 7.1.

Remarkable improvement was noted with this improved setup: successful detection of the sun took place on the 5th of December 2020, when observing the sun across a 1.1 m baseline, as shown in Figure 7.2.

The observation took approximately 26 minutes to complete in which two distinct fringes were noted near 400 s and 900 s. However, this result indicated that the system was susceptible to RFI, with spikes in output noted particularly 1100 s and 1400 s, which would needed to be addressed.

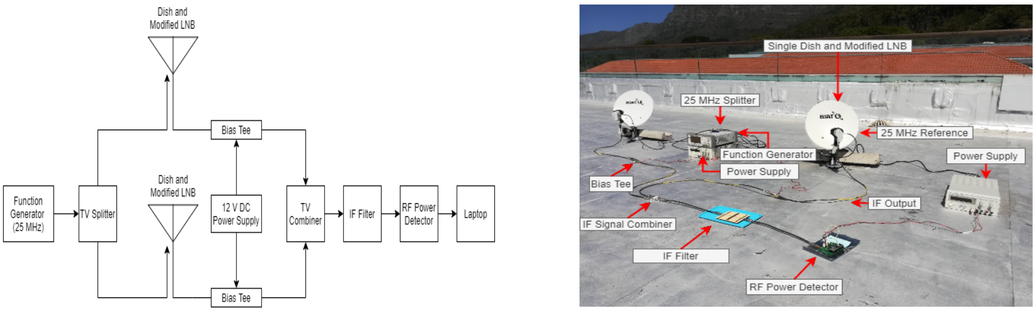

(a) Block diagram configuration

(b) Equipment setup

Figure 7.1: Equipment setup of the improved coherent two-element interferometer with which first light was observed. The IF filter was placed between the IF combiner and RF power detector to remove the spurious LO signal and reduce the IF passband

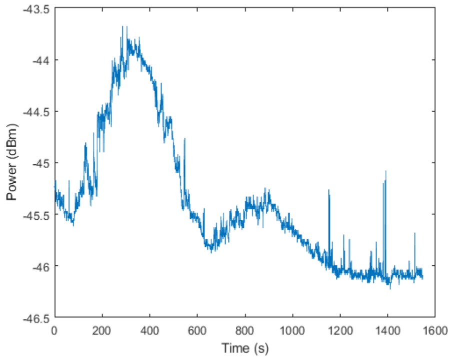

Figure 7.2: First light: observing the sun using the improved coherent two-element interferometer. The observation was conducted along a 1.1 m baseline and two distinguishable fringes are visible near 400 s and 900 s.

7.2 IMPROVED SHIELDING AGAINST RFI

In order to reduce the effects of RFI on the system, the IF filter and RF power detector were placed in cast iron and stainless steel cases, respectively. Each case included screw-on lids, while drilled holes on the sides of the cases, which allowed for easier cable connection. These cases are shown in Figures 7.3a and 7.3b along with the final equipment setup of the coherent two-element interferometer in Figure 7.3c.

Drift-scans of the sun across a 1.9 m baseline were performed with and without these cases - the corresponding results are shown in Figure 7.4. Significant improvement in performance was noted once again as a result of these cases.

Seven fringes were clearly visible in both of these observations over the 28-minute period, however substantial spikes were noted in Figure 7.4a as result of RFI and the system's lack of defence against it. Vast improvements were seen as per Figure 7.4b which showed a reduction in both the amplitude and occurrence of RFI. These results indicate that the inclusion of metallic cases greatly assisted in reducing RFI.

7.3 BASELINE VERIFICATION

The period of the output fringes correspond to an angular shift, $\Delta\theta$, in source of $\Delta\theta \approx \lambda/b$. Thus, the baseline length could be verified using the measured fringe period of a known source along with known data regarding the source's rotational behaviour. If the angular shift and operating frequency are both known, this approximation can be used to determine the baseline, as $b \approx \lambda/\Delta\theta$.

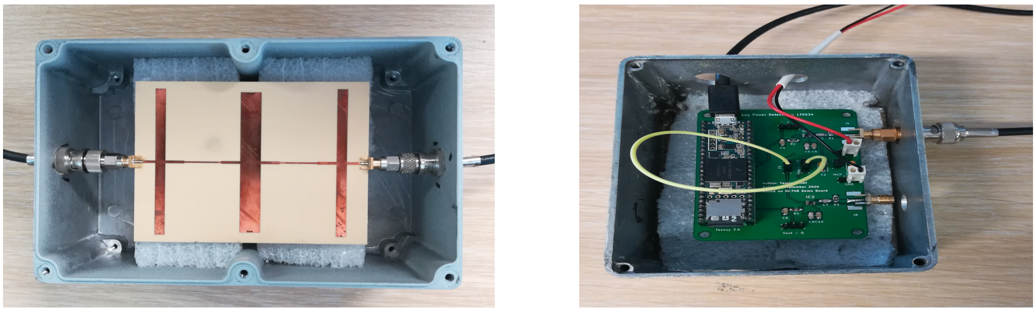

(a) IF Filter Case

(b) RF Power Detector Case

(c) Final equipment setup of the coherent two-element interferometer

Figure 7.3: Improved shielding against RFI by making use of cast iron and stainless steel cases.

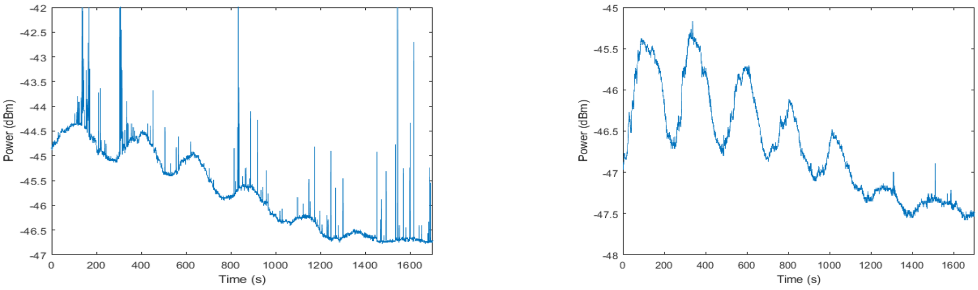

(a) Cases excluded.

(b) Cases included.

Figure 7.4: Drift-scan observations of the sun along a 1.9 m baseline. Observations were first performed without metallic cases which were later introduced to reduce the effects of RFI.

The sun, being the primary source under observation, is known to have a relative (to the earth) rotation of 360° over a 24-hour period. This corresponds to 15° per hours and 0.25° per minute. This data could be applied to the result in Figure 7.5 to determine the physical baseline with which this observation was conducted.

As per this observation, three distinct fringes were visible, with an average fringe period of 344 s (5.73 minutes). This corresponded to an angular shift of 1.43° (0.025 radians). The filtered IF signal centred at 1.0975 GHz, which corresponded to an RF signal centred at 10.8475 GHz and wavelength of 0.0277 m. Applying this to the above mentioned approximation yielded a theoretical baseline of 1.11 m. The same procedure was applied to the 1.9 m baseline data presented in Figure 7.4b, which showed an average fringe period of 220 s (3.67 minutes). This corresponded to an angular shift of 0.92° and theoretical baseline of 1.73 m.

Errors in this results may be attributed to fluctuations within the LNBs (such as that seen near 350 s in Figure 7.5) as well as the wider resolution of the IF filter (the IF filter passes a band of frequencies, as opposed to a single frequency). Furthermore, data processing such as the correcting of baseline shifts would also assist in reducing this error, but was beyond the scope of this project. Nonetheless, for the purpose of amateur observations, this was an impressive difference of between 0.17 m - 0.19 m between the theoretical and physical distances. It further

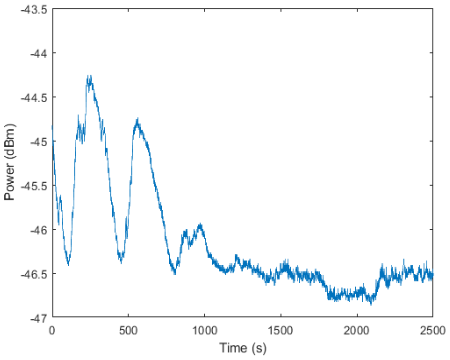

Figure 7.5: Drift-scan observation of the sun performed along a 1.3 m (physically measured) baseline. Three distinct fringes were visible, with an average period of 344 s - this corresponded to a theoretical baseline of 1.11 m

indicated that the interferometer was operating correctly, and its observed fringes could be used to verify the interferometer baseline.

7.4 RESOLVING SOURCES

This section focuses on observations of the sun which was conducted using the coherent two-element interferometer. Focus was placed on observing the change in output fringes when the baseline was varied.

As previously discussed, one of the benefits of an interferometer is its ability to detect smaller sources by increasing the baseline. The angular diameter, θ, of the sun is approximately 0.53° (0.0093 radians). As the observations were conducted at 10.85 GHz, the sun could be resolved (as per $\theta = \lambda/b$) using a baseline of 2.98 m.

Observations were conducted along baselines varying from 1.3 m to 3 m, as per Figure 7.6. These results indicated that the fringe frequency increases with an increase in baseline; this agreed with 2.32 which stated that the fringe frequency was directly proportional to the baseline. Thus, for a fixed observation time, more fringes would be observed along longer baselines. Consequently, for a given observation time, the fringe width decreases as the baseline increases.

Also noticeable in these results was the decrease in fringe amplitude specifically (peak-to-trough of fringes excluding the effects of modulation) as the baseline was increased. This can be justified using Figure 2.8: as the baseline increases, the fringe width decreases thus, the source is comparable in size to the spacing between bands (fringes). At a given time the source is crossed by multiple maxima and minima, thus pure constructive/ destructive interference does not take place, which reduces the fringe amplitude. This was most prominent using a 3 m baseline (Figure 7.6d) in which the fringes were barely visible - this is attributed to the baseline having been increased to the theoretical distance at which the sun could be resolved.

7.5 EFFECTS OF CORRELATION AND SYSTEM TEMPERATURE

The pandemic limited access to sophisticated hardware typically used to quantify the performance of a radiometer. Instead, this section discusses the rudimentary techniques used to observe the effect of correlating the elements' signals with one another. Thereafter, it offers an effort to quantify the system temperature and sensitivity based on a simple hot-cold test.

7.5.1 Effects of Correlation

A simple method to verify that the interferometer was operating correctly (i.e. correlating the elements' IF signals with one another), was to align both dishes to point at a known source. This should result in a peak in output as the correlation would be at its greatest. However, if one of the dishes was misaligned with the source, the output would decay significantly due to the correlation being weakened.

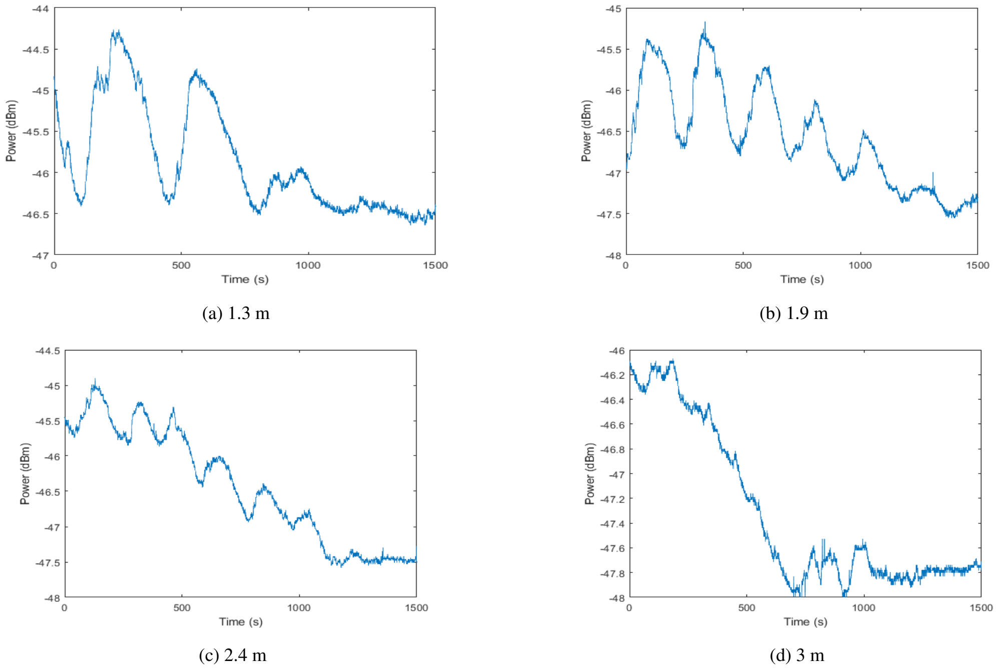

(a) 1.3 m

(b) 1.9 m

(c) 2.4 m

(d) 3 m

Figure 7.6: Drift-scan observations of the sun with varying baseline lengths- an increase in fringe frequency and a decrease in fringe amplitude was noted for the increase in baseline. The fringe amplitude decayed significantly when the baseline was increased to 3 m as this was approximately the baseline required to resolve the sun.

Figure 7.7 shows the output of such a test once again configured to observe the sun along a 1.9 m baseline. When both dishes were aligned with the sun (0 s - 50 s), the output showed a steady increase from - 44.14 dBm to - 43.14 dBm. Similar to the fringes observed in previous measurements, this increase was attributed to the constructive interference taking place as the sun drifted across the interferometer. However, at 50 s, one of the dishes was turned away from the sun, thus reducing the output to approximately -45.22 dBm. The output then remained almost constant for the remaining duration of the observation. This constant reduced output verified that the system was performing correctly - only signals common to both elements resulted in an increased output, as expected from the correlator.

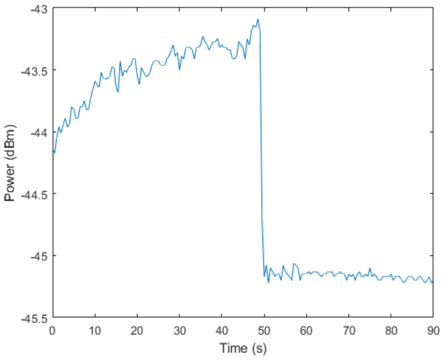

Figure 7.7: The effects of correlation could be observed by aligning and misaligning elements with a common source. Between 0 s - 50 s, both dishes were aligned with the sun resulting in the increased fringe amplitude. Thereafter, one of the dishes was misaligned with the sun resulting in the steep decay in output.

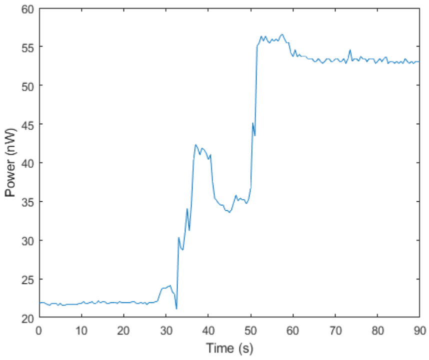

Figure 7.8: Determining the receiver temperature by means of a hot-cold test. The sky (cold source) was observed between 0 s - 27.5 s. A single dish was then pointed at the ground (hot source) between 32.5 s - 49 s. Thereafter a second dish was also pointed at the ground between 49 s - 90 s. The relatively constant output verified that the dishes were aligned with non-varying sources.

7.5.2 System Noise Temperature and Sensitivity

The receiver's temperature/ noise figure can typically be determined using the Y-factor method or gain method. The former requires the use of calibrated noise source with a known Excess Noise Ratio (ENR), while the latter technique requires precise measurement of the receiver gain. Neither of these techniques were possible given the limited access to resources. Instead, a hot-cold test was used to determine the receiver and system noise and temperatures, and consequently determine the receiver sensitivity. This included observing the sky (cold load) followed by observing the ground (hot load), as shown in Figure 7.8.

7.5.2.1 Receiver and System Noise Temperature

The average output of 21.9 nW (P_1) when observing the sky was attributed to the receiver temperature (T_R) and the sky temperature (T_{Sky}), such that $cP_1 = T_R + T_{Sky}$, where c is the proportionality constant (K/nW). T_{Sky} comprises of radiation from the Cosmic Microwave Background (CMB), water vapour in the atmosphere, and ground radiation entering the dishes' sidelobes.

The average output increased to 53.3 nW (P_2) when both dishes were pointed at the ground - this comprised of the receiver temperature (T_R) and ground temperature (T_{Ground}), such that $cP_2 = T_R + T_{Ground}$.

T_{Sky} was approximately 15 K, while T_{Ground} was approximately 290 K [3]. Applying this to the above observations yielded $c = 8.76$ K/nW and $T_R = 176.35$ K. As discussed in Section 2.2.2.1, the system noise temperature, T_{Sys}, is the summation of T$_R$, and the antenna temperature, T_A. In the absence of the source, $T_A = T_{Sky}$, thus, $T_{Sys} = 191.35$ K.

Similarly, on the day of the hot-cold observation, the output fringes showed a peak of 44.0 nW (P_3) when aligned with the sun. This output was as a result of the portion of the main-beam filled by the suns radiation and corresponding temperature, T_{sun}, along with T_R and T_{Sky}, such that $cP_3 = T_{sun} + T_{Sky} + T_R$. This resulted in $T_{sun} = 193.52$ K.

This high system noise temperature may be attributed to the following factors:

- The extreme physical heat to which the LNBs were exposed raised the receiver temperature. These conditions would not be as severe had lab-based tests such as the Y-factor method been used to classify the receiver temperature.
- Uncorrelated noise present in each of the LNBs are added to the correlated source signal. This is inherent to the adding interferometer, and results in a raised system temperature.

- Inaccuracies in the approximations used by the hot-cold tests which may have skewed the data.
- Impedance mismatches between the 75 Ω satellite TV equipment and standardised 50 Ω equipment (cables, connectors, RF PCBs etc.) resulted in increased losses and consequently raised the receiver temperature. Impedance matching pads were ordered, but had not arrived in time for these measurements.
- Discrepancies may exist between the manufacturer's stated LNB noise figure and its true noise figure, similar to those identified by [9].

Regardless, the system was still capable of observing the sun, which was the primary goal outlined at the beginning of this project. The system noise temperature could be improved by the inclusion of impedance matching pads as well as the adjusting the sampling and integration time of the RF power detector.

7.5.2.2 *Radiometric Resolution*

In addition to the system noise temperature, the radiometric resolution is a key benchmark in determining the instruments sensitivity and consequently its ability to detect radio sources. The concept of receiver sensitivity was introduced in Chapter 2 - specific to the adding interferometer, the radiometric resolution is given by 2.21, repeated below for convenience:

$$\Delta T_{min} = \frac{T_{sys}}{\sqrt{\Delta B \tau}} \tag{7.1}$$

Applying the estimated system noise temperature, $T_{Sys} = 191.35$ K, over the IF bandwidth, $\Delta B = 100$ MHz, and an integration time, $\tau = 500$s, to 7.1 yields a radiometric resolution of 0.86 mK, which is the weakest radio signal (in terms of noise temperature) this instrument can detect.

This can further be extended to the minimum flux density detectable by this two-element radio interferometer. Due to its similar architecture, the adding interferometer and ideal total power radiometer share the same minimum detectable flux density, ΔS, given by 2.28, which is also repeated here for convenience:

$$\Delta S = \frac{2k}{A_e} \frac{T_{sys}}{\sqrt{\Delta B \tau}} \tag{7.2}$$

The effective area in 7.2 is determined by the physical area of the dish with a diameter of 0.38 m along with its aperture efficiency of 0.75. Applying this combined data to 7.2, yields an estimated minimum detectable flux density of $\Delta S = 27.77$ Jy.

However, as previously discussed, the total power radiometer and consequently the adding interferometer are susceptible to gain variations which increases their radiometric resolution and consequently increases their minimum detectable flux density. Characterisation of this gain variation was not possible due to limited access to equipment, however, as indicated by [1], these variations may worsen the instrument's sensitivity by a factor of 5. Thus, a more accurate estimate of the system's radiometric resolution is $\Delta T = 2.57$ mK, and the corresponding estimate of the minimum detectable flux density is $\Delta S = 138.84$ Jy. While this result is incomparable to larger professional radio astronomy instruments, such as MeerKAT, which is capable of detecting sources weaker than 1 Jy, this amateur instrument was well within the initial specifications of having a minimum detectable flux density of less than 500 Jy.

7.6 FULL SYSTEM TESTING: ANALOGUE COMPLEX CORRELATOR

After having successfully tested the standard two-element adding interferometer, focus was placed on adapting the system to perform complex correlation, which will now be discussed. This adaptation increased the overall system complexity as separate filters, power dividers and hybrid couplers were required for each LNB - the standard interferometer only required a single IF filter after the signals were combined, as per Figure 7.1a. This adapted

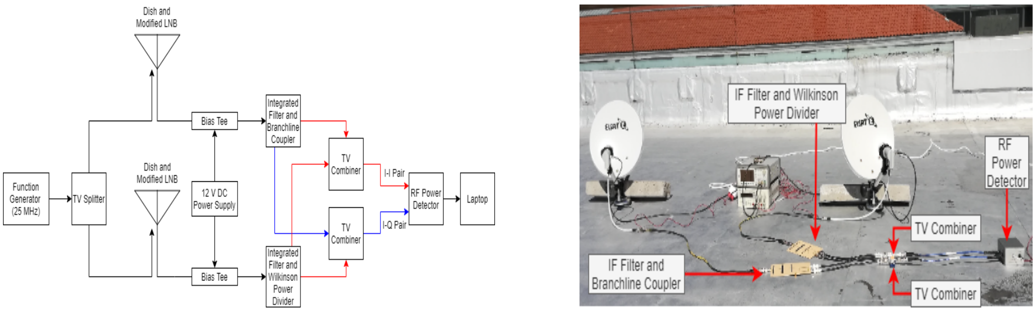

(a) Block diagram configuration (b) Equipment setup

Figure 7.9: Equipment setup of the coherent two-element adding interferometer capable of performing complex correlation. The quarter-wavelength stub filters with integrated Wilkinson power dividers and branchline couplers were used during these observations.

version made use of the integrated Wilkinson power dividers and branchline couplers. The quarter-wavelength stub filter equivalents were used due to the spurious passband limitations of the hairpin filter, as discussed in Section 6.3.3. The equipment setup of this adapted system is shown in Figure 7.9.

The tests of this complex correlating adding interferometer were conducted along three baseline lengths: 1.9 m , 2 m, and 2.3 m - these are shown in Figure 7.10.

Distinct fringes, similar to those previously found using the standard adding interferometer (Figures 7.2 and 7.3), were once again observed for both in-phase and quadrature components. Similarly, an increased baseline resulted in an increased fringe frequency, along with a reduced peak-to-null amplitude. However, it was evident that these fringes (I-I component and I-Q component) are delayed relative to one another.

This delay was as a result of the correct phase-shift introduced by the branchline coupler, as discussed in Section

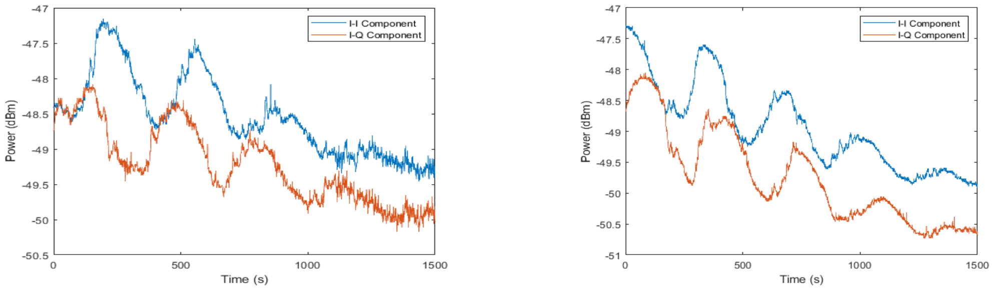

(a) 1.9 m (b) 2 m

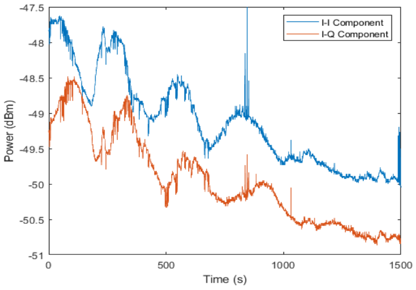

(c) 2.3 m

Figure 7.10: Drift-scan observations of the sun across varying baselines. These were completed using the adapted two-element adding interferometer capable of performing complex correlation.

6.3.3. As the fringe outputs were quasi-sinusoidal, the I-I and I-Q outputs resembled two sinusoidal graphs which had a relative delay of approximately 90°. This justified why the fringes were misaligned, but not completely out-of-phase (180°) relative to each other.

Due to the various delays experienced and consequently the reduced time available for testing, there were certain issues of this adapted system which could not be addressed such as the amplitude imbalance and RFI. Approximately 1 dB of imbalance was observed between the I-I and I-Q outputs in all three of these drift-scan observations. This could be attributed to the minor amplitude and phase imbalance of the individual PCB outputs as well as the minor difference in passband performance between the two PCBs. However, this had not fully been investigated yet. Issues regarding RFI could more easily be identified as it resembled the earlier RFI issues. Specifically, the exposed PCBs were susceptible to in-band RFI which resulted in fluctuations and spikes in results.

Regardless, these observed results indicate that the two-element adding interferometer had successfully been adapted for complex correlation and was operating correctly.

7.7 SUMMARY OF CHAPTER

This chapter focused largely on observations performed using the coherent two-element adding interferometer, which successfully detected the sun during various drift-scans. Initial results indicated a strong susceptibility to RFI - this was addressed by enclosing hardware in metallic cases, which showed noteworthy improvement in performance.

Thereafter, the sun's known trajectory was used to verify the physical baseline for which an observation was conducted. Furthermore, the effects of baseline length on output fringes were observed for increasing baselines. This was then followed by a hot-cold test which was used approximate the receiver temperature and the system temperature.

Finally, the two-element adding interferometer capable of complex correlation was discussed. This adapted interferometer successfully observed the sun with a consistent phase difference between the I-I and I-Q output pairs. Issues such as minor amplitude imbalance and RFI were experienced, however these initial results were encouraging and motivate future testing and development of this system.

CHAPTER 8

CONCLUSION

This thesis discussed the design, assembly, and testing of a two-element radio interferometer, which primarily made use of satellite TV equipment. This chapter encapsulates the focal design stages discussed in the previous chapters and further draws conclusions based on the success of the developed system.

8.1 PROJECT BACKGROUND

The design of such a two-element radio interferometer was motivated by the rapid development in science and technology, particularly in the field of radio astronomy. With the construction of sophisticated instruments like MeerKAT in South Africa, it would be crucial to teach the fundamental concepts of radio astronomy to existing students to garner their interest in STEM. This could be achieved by the development of a low-cost radio interferometer which primarily made use of repurposed satellite TV equipment.

In order to better understand the need of an interferometer and its advantages over single-dish instruments, this thesis commenced with a literature review of radio astronomy in particular, radio interferometry and its underlying architectures, such as the adding interferometer and the multiplying interferometer.

Thereafter, attention shifted to COTS satellite TV equipment and how these have previously been implemented in amateur radio astronomy instruments such as the VSRT and KISS. The use of LNBs as the front-end of the receiver and how these could be modified to ensure coherency between elements of the interferometer was of particular interest. One of the techniques identified was to replace the LNBs' 25 MHz XTAL with a common reference.

8.2 SYSTEM REQUIREMENTS AND ANALYSIS

Following the project background, the thesis discussed the various user, functional, and design requirements. In particular, the need to develop a two-element radio interferometer capable of observing the sun. Another important requirement was that the interferometer should perform analogue complex correlation. A set of ATPs were developed to ensure that all these requirements were met. All the ATPs were successfully fulfilled and the corresponding sections of this thesis in which these ATPs were fulfilled, are shown in Table 8.1.

The various project constraints were also identified - one of the most prominent being the SARS-CoV-2 pandemic which introduced time-delays and restricted access to equipment.

8.3 INITIAL TESTS AND OBSERVATIONS

Initial testing of COTS satellite TV equipment was rhen discussed - in particular, the operation of the LNB and its 9.75 GHz LO . This was investigated by transmitting an RF signal at 10.85 GHz and observing a distinct output at 1.10 GHz (which was the correct IF frequency). Attention then shifted to the (successful) modifications of the LNBs to make use of an external 25 MHz reference.

Table 8.1: Set of ATPs initially developed to ensure that all the user, functional, and design requirements were fulfilled. *Chapter/ Section* refers to the location in this thesis where a specific ATP was resolved.

Index	Reference	Test Procedure	Chapter/ Section
A.01	R.F.0.1, R.F.09	A known source (sun) will drift across the elements and the output fringes will be observed. The measured fringe phase and corresponding theoretical baseline will be compared to the physical baseline.	Section 7.3
A.02	R.F.03, R.F.04, R.F.05	The sun will be observed across varying baselines. As the baseline is increased, the fringe frequency is expected to increase, while the fringe amplitude should decrease. The baseline for which the fringe amplitude reduces to approximately zero will be compared to the theoretical baseline required to resolve the sun.	Section 7.4
A.03	R.F.04, R.F.06, R.F.07	While observing the sun, one element will continuously be rotated resulting in an increase and decrease in correlation. The correlation should decrease when the elements are pointing in opposite directions.	Section 7.5
A.04	R.F.06, R.F.07	Custom manufactured RF PCBs will be measured individually using a Vector Network Analyser (VNA). The measured results will be compared to the corresponding simulated results to examine how well signals are separated into I-Q components.	Chapter 6
A.05	R.F.02, R.F.09	Measure both modified LNBs responses (power and IF frequency) when in the presence of a wire antenna transmitting at 10.85 GHz. This result will be compared to the unmodified LNBs response to verify that the modified LNBs PLLs are correctly locking to the new 25 MHz reference.	Section 4.2.1, Section 6.1.3
A.06	R.F.04, R.F.05	The designed RF power detectors will be calibrated at 1.10 GHz using a calibrated RF signal generator. Thereafter the calibrated power detectors response to varying (known) RF levels will be measured. The error (difference between measured and expected outcome) should be less than 30 mV.	Section 4.3.2.2

This was followed by the design of a suitable RF power detector PCBs which comprised of the Analog Devices LT 5534 power detector IC and the Teensy 3.6 Microcontroller. Two ICs were included on a single PCB such that the I-I and I-Q correlation pairs could synchronously be measured and stored.

Lastly, the chapter discussed the initial observations of the sun using a single-dish setup as well as the non-coherent and coherent interferometer setups. The sun was detected by all three configurations, but the coherent interferometer in particular experienced performance issues. This was resolved by the design of specialised PCBs.

8.4 IF FILTERING AND I-Q SEPARATION

Specialised RF PCBs were designed to overcome the limitations of the COTS equipment and the issues resulting from having modified the LNBs. Hairpin filters and quarter-wavelength stub filters were designed to suppress the LNBs' spurious LO and to further ensure that the system was narrowband.

The latter requirement allowed IF signals to be separated into I-Q components without the need of a complex heterodyne stage. Instead, a series of Wilkinson power dividers and branchline couplers were designed to separate signals into I-Q pairs. Filters were also integrated onto these structures to reduce loss and overall complexity.

These PCBs were manufactured and measured - almost all the PCBs showed an impressive agreement between the simulated and measured results. Significant phase discrepancies between the simulated and measured results were only found for the standard Wilkinson power divider, which may have been attributed to undesired coupling.

However, this did not introduce any delays as all the integrated equivalents functioned correctly. In order to minimise amplitude and phase errors, the quarter-wavelength stub filter and its corresponding integrated designs were used during the full-system tests.

8.5 FULL-SYSTEM TESTING

After successfully designing the various sub-systems and resolving all the issues, attention once again shifted to full-system observations of the sun. First light (first successful observation) of the sun was observed along a 1.1 m baseline in which two distinct fringes were seen over the 26 minute observation. The observed issue of RFI was resolved by placing PCBs into separate metal cases.

The fringe pattern and suitable approximations were then used to verify the physical baseline. For a baseline of 1.3 m (physically measured), the fringe period indicated a theoretical baseline of 1.11 m , which was an acceptable discrepancy of less than 0.2 m. This discrepancy may have been attributed to LNB fluctuations and the interferometer's resolution.

Other tests conducted included observing the sun's fringe pattern along different baseline lengths. The fringe amplitude decayed, while the fringe frequency increased, as the baseline increased. The fringes were almost indiscernible from the single dish beam pattern when the baseline was increased to 3 m. This agreed with the calculated baseline required to resolve the sun.

The receiver temperature was determined to be 176.35 K, while the antenna temperature (when observing the sun) was 193.52 K. These were notably high, and may have been attributed to, among others, the inaccurate noise figure ratings of the LNB and the physical temperature to which the devices was exposed. Regardless of this, the sun's fringes were still clearly visible.

Lastly, the completed two-element interferometer was tested. This included observations of the sun's I-I and I-Q output fringes. The output I-I and I-Q fringes closely resembled one another, however there was a distinct delay between the cosine and sine fringes. This was attributed to the 90° phase-shift introduced by the branchline coupler, as required by the system.

Thus, the primary goal of this project was fulfilled: a two-element radio interferometer capable of performing analogue complex correlation was designed and built, and was successful in detecting the sun.

CHAPTER 9

RECOMMENDATIONS AND FUTURE WORK

The developed two-element radio interferometer successfully fulfilled the various requirements outlined at the beginning of the project. However, due to the limited time and resources available, there were certain aspects of the project which could not be refined or explored. This should be addressed in future implementations, as discussed in this chapter.

9.1 FULL-SYSTEM INTEGRATION: SUPERHETERODYNE NETWORK

One of the techniques explored in separating the LNBs' IF signals into I-Q components was the superheterodyne network, as discussed in Appendix B. This technique involved an additional down-conversion stage which made use of an LO that was first separated into its I-Q components. The entire network of PCBs required for this implementation was manufactured and tested as shown in Appendix C, however, due to its increased complexity, it was not implemented. Future implementations should thus compare the full-system performance of both I-Q separation techniques, as the PCBs required by both techniques were manufactured and were found to be functioning correctly.

9.2 MULTIPLYING INTERFEROMETER

An alternative to the adding interferometer is the multiplying interferometer, which offers reduced output noise and consequently improved sensitivity. Its architecture previously discussed in Chapter 2 made use of a mixer and low-pass filter to multiply the elements signals instead of the combiner and power detector, found in the adding interferometer. Apart from these differences, both architectures share the same design in terms of LNB modifications and the I-Q separation network. As such, future implementations should explore the performance of the multiplying interferometer.

9.3 ALTERNATIVE PCB SUBSTRATES

The various RF PCBs required for filtering and I-Q separation were manufactured on Mercurywave substrate. This was chosen as it could be manufactured locally and offered low-loss performance, however at an increased cost. Low-loss was an important factor as these PCBs were developed during the initial prototyping stages of the project during which the LNBs' response to such devices were unknown.

However, having proven that the LNBs offered sufficient gain and operated correctly with such PCBs structures, the various filters, power dividers and hybrid couplers should be redesigned/ optimised using alternative substrates, such as FR-4. While this would result in increased losses, the interferometer would still be able to detect the sun (due to the high LNB gain), however, would now do so at a significantly reduced cost. This would greatly encourage replication of the system among students.

9.4 EDUCATIONAL OUTREACH

This project was aimed at developing a two-element radio interferometer to be used for educational demonstrations. Future work should include developing a lab module which makes use of the developed the two-element interferometer. The lab module could be in the form of a YouTube series which covers topics such as the fundamental concepts of radio interferometry, step-by-step assembly of the interferometer, and guidelines for observing radio sources - this platform would assist in reaching a larger audience.

The lab module should further demonstrate the various stages of developing a radio interferometer - starting with a simple single-dish receiver, followed by a non-coherent interferometer, and lastly the coherent interferometer. This technique would promote gradual development of students' theoretical and practical understanding of both the science and engineering fields.

BIBLIOGRAPHY

[1] J. J. Condon and S. M. Ransom, *Essential Radio Astronomy*. Princeton University Press, 2016.

[2] D. F. Miller, *Basics of Radio Astronomy for the Goldstone−Apple Valley Radio Telescope*. Jet Propulsion Laboratory, 1998.

[3] M. Gaylard, "Radio Astronomy with a Single−Dish Radio Telescope," August 2012. Available at: http://avntraining.hartrao.ac.za/images/radio_astronomy_theory.pdf. Accessed: 21 December 2019.

[4] D. Hayden, "Introduction to Interferometery," March 2018. Available at: http://avntraining.hartrao.ac.za/images/Schools/2018March/2018_Talks/AVN2018_DH_Interferometry.pdf. Accessed: 28 December 2019.

[5] A. R. Thompson, J. M. Moran, and G. W. Swenson, *Interferometry and Synthesis in Radio Astronomy*. Springer, 2017.

[6] "Ellies Universal Twin LNB," September 2017. Available at: https://www.ellies.co.za/product/elsat-twin-universal-lnb-10-6ghx-osc/. Accessed: 05 January 2020.

[7] A. Talbot, "Using an External LO Source with the Octagon PLL Low Noise Block ," June 2016. Available at: http://g4jnt.com/OctagonExtLo.pdf. Accessed: 06 January 2020.

[8] D. Leupold, "Low Cost TVSat LNB Disciplined to 10MHz Reference," November 2019. Available at: http://www.df9np.de/page4.html. Accessed: 06 January 2020.

[9] N. A. Salmon, P. N. Wilkinson, and J. Radiven, "Amplitude and Intensity Interferometry using Satellite LNB Receivers for Innovative and Low Cost Microwave and Millimetre Wave Sensor Development," in *Millimetre Wave and Terahertz Sensors and Technology V*, vol. 8544, pp. 80 – 89, International Society for Optics and Photonics, SPIE, 2012.

[10] J. Marr, A. Pere, K. Durkota, A. Rogers, V. Fish, and M. Arndt, "Laboratory Exercises Using the Haystack VSRT Interferometer To Teach the Basics of Aperture Synthesis," *arXiv preprint arXiv:1109.3816*, September 2011.

[11] C. F. Jentink, "Constructing the Backend of the Kapteyn Interferometer for Short-Baseline Solar Observations (KISS)," Dissertation, University of Groningen, July 2018.

[12] W. P. Lonc and K. Tapping, *Radio Astronomy Projects*. Radio-Sky, 2006.

[13] J. Lee, K.-C. Yoon, H. Lee, T.-S. Jung, T.-Y. Kim, and J.-C. Lee, "Open Stub Band-pass Filter using Stepped Impedance Resonator for Size Reduction," in *2013 Asia-Pacific Microwave Conference Proceedings*, pp. 875–877, November 2013.

[14] D. M. Pozar, *Microwave Engineering*. John Wiley & Sons, 2012.

[15] D. D. Harty, “Novel Design of a Wideband Ribcage Dipole Array and its Feeding Network,” Master’s thesis, Worcester Polytechnic Institute, December 2010.

[16] M. Rosenberg, G. Baldon, P. Russo, and L. L. Christensen, “Astronomy in Everyday Life,” *Communicating Astronomy to the Public Journal*, vol. 14, pp. 30–36, 2014. Accessed: 2019-11-24.

[17] C. Ramaphosa, “State of the Nation Address by President Cyril Ramaphosa, Parliament,” February 2019. Available at: http://www.thepresidency.gov.za/newsletters/state-nation-address-president-cyril-ramaphosa%2C-parliament. Accessed: 24 November 2019.

[18] SARAO, “MeerKAT Radio Telescope,” 2018. Available at https://www.sarao.ac.za. Accessed: 24 November 2019.

[19] M. Limn, “Importance of Astronomy in Modern Education,” *Tecnológico de Monterrey*, April 2019. Available at: https://observatory.tec.mx/edu-news/why-should-teaching-astronomy-be-a-priority-in-education. Accessed: 24 November 2019.

[20] E. Gough, “China’s FAST Telescope, the World’s Largest Single Radio Dish Telescope, is Now Fully Operational,” September 2019. Available at: https://www.universetoday.com/143346/chinas-fast-telescope-the-worlds-largest-single-radio-dish-telescope-is-now-fully-operational. Accessed: 26 December 2019.

[21] J. Brodkin, “Cable and Satellite TV Sinks Again as Online Streaming Soars,” July 2019. Available at https://arstechnica.com/information-technology/2019/03/cable-and-satellite-tv-sinks-again-as-online-streaming-soars/. Accessed: 24 November 2019.

[22] S. Arnold, *Getting Started in Radio Astronomy: Beginner Projects for the Amateur*. Springer, 2014.

[23] M. Garret, “Emission Mechanisms in Radio Astronomy,” April 2013. Available at: https://www.astron.nl/astrowiki/lib/exe/fetch.php?media=ra_uva:ra_uva_lecture4.pdf. Accessed: 26 December 2019.

[24] J. D. Kraus, M. E. Tiuri, A. V. Raisanen, and T. D. Carr, *Radio Astronomy*. Cygnus-Quasar Books, 1986.

[25] W. L. Stutzman and G. A. Thiele, *Antenna Theory and Design*. Wiley, 2013.

[26] C. Gohd, “China is Opening the World’s Largest Radio Telescope up to International Scientists,” December 2020. Available at https://www.livescience.com/china-fast-radio-telescope-open-international-scientists.. Accessed: 30 December 2020.

[27] K. Zhang, A. Peck, J. Braatz, A. Isella, and S. Stierwalt, “Introduction to interferometry,” March 2017. Available at: https://science.nrao.edu/science/meetings/2017/umichigan17/InterfBasics_UM.pdf. Accessed on 25 December 2019.

[28] M. Ryle and D. D. Vonberg, “Solar Radiation on 175 Mc./s,” *Nature*, vol. 158, p. 339340, Sep 1946.

[29] M. Ryle, “A New Radio Interferometer and Its Application to the Observation of Weak Radio Stars,” *Proceedings of the Royal Society*, vol. 211, p. 351375, Mar 1952.

[30] F. T. F. T. Ulaby, *Microwave radar and radiometric remote sensing*. Ann Arbor: University of Michigan Press, 2014.

[31] T. L. T. L. Wilson, *Tools of radio astronomy*. Astronomy and astrophysics library, Berlin: Springer, 5th ed. ed., 2010.

[32] C. Klein, “The Birth of Satellite TV, 50 Years Ago,” July 2012. Available at: https://www.history.com/news/the-birth-of-satellite-tv-50-years-ago. Accessed on 05 January 2020.

[33] G. Girlando, T. Copani, S. A. Smerzi, and G. Palmisano, “A ku-band monolithic tuner-lnb for satellite applications [low noise block down-converter],” in *Proceedings of the IEEE 2004 Custom Integrated Circuits Conference (IEEE Cat. No.04CH37571)*, pp. 613–616, Oct 2004.

[34] Norsat, "How to Choose the Best LNB for your Satellite System," December 2019. Available at: https://www.norsat.com/choosing-the-best-lnb/. Accessed: 05 January 2020.

[35] D. Maloney, "Es'hail-2: Hams Get Their First Geosynchronous Repeater," Mar 2019. Available at: https://hackaday.com/2019/03/18/eshail-2-hams-get-their-first-geosynchronous-repeater. Accessed: 06 January 2020.

[36] C. Forster, "Chippewa Valley Astronomical Society Star Party Introduces the Little Bitty Telescope Version 2 and LBT Experiment No. 1," November 2001. Available at: http://www.setileague.org/articles/lbt.pdf. Accessed: 09 January 2020.

[37] G. L. Matthaei, L. Young, and E. M. T. Jones, *Microwave Filters, Impedance-matching Networks, and Coupling Structures*. Artech House, 1985.

[38] J.-S. G. Hong and M. J. Lancaster, *Microstrip Filters for RF/Microwave Applications*. Wiley, 2001.

[39] K. C. Son, B. Shrestha, and K.-C. Yoon, "Miniaturized Narrow Band-pass Filter with Quarter-wavelength Short Stubs using U-shaped Folded Transmission Line," *Microwave and Optical Technology Letters*, vol. 57, no. 12, pp. 2862–2865, 2015.

[40] K. Yoon, H. Lee, D. Lee, and J. Lee, "Design of a Compact Narrow Band-pass Filter with $\lambda_g/4$ Short Stubs," in *2009 Asia Pacific Microwave Conference*, pp. 1454–1457, 2009.

[41] A. Qaroot and N. Dib, "General Design of N-way Multi-frequency Unequal Split Planar Wilkinson Power Divider," *Progress in Electromagnetics Research C*, vol. 14, pp. 115–129, 01 2010.

[42] L. J. Berens, "Design, Analysis, and Construction of an Equal Split Wilkinson Power Divider," Master's thesis, Marquette University, Sep 2012.

[43] "Power splitter/combiner."

[44] "Power splitter/combiner."

[45] D. Kurniawan, C. Bin Ali Wael, T. Miftahushudur, and O. Heriana, "Implementation of automatic i/q imbalance correction for fmcw radar system," in *2017 2nd International conferences on Information Technology, Information Systems and Electrical Engineering (ICITISEE)*, pp. 100–105, 2017.

[46] A. Gomaa and L. M. A. Jalloul, "Receiver architecture for frequency offset correction and i/q imbalance compensation in equal bandwidth contiguous carrier aggregation," *IEEE Transactions on Vehicular Technology*, vol. 65, no. 10, pp. 8730–8735, 2016.

APPENDIX A

RF POWER DETECTOR: TEENSY 3.6 MICROCONTROLLER

Teensy 3.6 microcontroller code for sampling two (I-Q sampling) LT 5534 RF power detectors. Microcontroller code includes assistance from Arduino Teensy Example Libraries:

- Datalogger: SD card datalogger, created by Tom Igoe.
- SynchronizedMeasurements: Synchronous sampling of ADC0 and ADC1, included in standard Arduino Teensy Examples.

```
//RF Power Detector
//Analog Devices LT5534 and Teensy 3.6 Microcontroller

/*Calibration Data (Devices calibrated at -45 dBm and -35 dBm at 1.10 GHz):
  - I-Channel m = 0.0349 dB/V, intercept = 2.302 V
  - Q-Channel m = 0.0361 dB/V, intercept = 2.359 V
*/

//Include Arduino libraries for synchronised ADC sampling and micro SD card storage

#include <IntervalTimer.h>
#include <ADC.h>
#include <ADC_util.h>

//-----------------------SD Card------------------------//
#include <SD.h>
#include <SPI.h>
const int chipSelect = BUILTIN_SDCARD;
//-----------------------SD Card------------------------//

//ADC Pins to use
const int readPin = A2;                                 //Power - I-Component
const int readPin2 = A17;                               //Power - Q-Component

ADC *adc = new ADC();                                   // adc object
elapsedMillis time;

IntervalTimer myTimer;
const int ledPin = LED_BUILTIN;                         // the pin with a LED

// Configuration for Power Detector
//LT5534 (2)
const double gradient_I = 0.0349;                       // Top - 500 ms sampling rate
const double int_I = 2.302;                             // Top - 500 ms sampling rate
const double gradient_Q = 0.0361;                       // Bottom - 500 ms sampling rate
const double int_Q = 2.359;                             // Bottom - 500 ms sampling rate

void setup() {
  pinMode(ledPin, OUTPUT);
  pinMode(readPin, INPUT);
  pinMode(readPin2, INPUT);

  Serial.begin(9600);

  //ADC0
  adc->setAveraging(1000); // set number of averages
  adc->setResolution(13); // set bits of resolution
  adc->setConversionSpeed(ADC_CONVERSION_SPEED::VERY_LOW_SPEED); // conversion speed
  adc->setSamplingSpeed(ADC_SAMPLING_SPEED::VERY_LOW_SPEED); // change the sampling speed

  //ADC1
  adc->setAveraging(1000, ADC_1); // set number of averages
  adc->setResolution(13, ADC_1); // set bits of resolution
  adc->setConversionSpeed(ADC_CONVERSION_SPEED::VERY_LOW_SPEED, ADC_1); // conversion speed
  adc->setSamplingSpeed(ADC_SAMPLING_SPEED::VERY_LOW_SPEED, ADC_1); // change the sampling speed
  adc->startSynchronizedContinuous(readPin, readPin2);

  //-----------------------SD Card------------------------//
  if (!SD.begin(chipSelect)) {
    Serial.println("Card failed, or not present"); // if the card is present and can be initialized:
    return;                                        // don't do anything more:
  }
  if (SD.exists("datalog.csv"))
  {
    SD.remove("datalog.csv");                      //Clear previous data
  }
  //-----------------------SD Card------------------------//
```

```
  delay(100);
  myTimer.begin(SampleADC, 500e3);                 // 500 ms between consecutive samples
}

double counter = 0;
double timerTotal = 7200;                          // Sample for 1 hour at 2 samples/s

ADC::Sync_result result;
String dataString ="";

void SampleADC(){
     if(counter<timerTotal)
     {
        counter++;
        result = adc->readSynchronizedContinuous(); //Sample both ADC values synchronously
        result.result_adc0 = (uint16_t)result.result_adc0;
        result.result_adc1 = (uint16_t)result.result_adc1;

        String ADC_0_String = String(((result.result_adc0)*3.3/4096- int_I)/gradient_I);
        //Convert sampled ADC_0 value to power value (dBm)
        String ADC_1_String = String(((result.result_adc1)*3.3/4096- int_Q)/gradient_Q);
        //Convert sampled ADC_1 value to power value (dBm)

        //String ADC_0_String = String(result.result_adc0);
        //Convert sampled ADC_0 value to 12-bit value
        //String ADC_1_String = String(result.result_adc1);
        //Convert sampled ADC_1 value to 12-bit value

        String Time_String = String(counter);

        //Convert time to string format
        dataString = ADC_0_String+","+ ADC_1_String;
        //Compile string to be written to serial/ .CSV file

        //-----------------------SD Card------------------------//
        File dataFile = SD.open("datalog.csv", FILE_WRITE);
        if (dataFile)
        {
           dataFile.println(dataString);
           dataFile.close();
           Serial.println(dataString);
        }
        else
        {
          Serial.println("error opening datalog.txt");
        }
        //-----------------------SD Card------------------------//
        if(digitalRead(ledPin)==HIGH)
        {
          digitalWrite(ledPin,LOW);
        }
        else
        {
          digitalWrite(ledPin,HIGH);
        }
     }
     else
     {
      digitalWrite(ledPin, HIGH);
      myTimer.end();
     }
}
void loop() {
}
```

APPENDIX B

ALTERNATIVE I-Q SEPARATION - SUPERHETERODYNE NETWORK

The primary focus of this chapter is the design of the individual components required to separate the superheterodyne's LO into I-Q components. This superheterodyne network was introduced in Chapter 5 and was identified as a suitable alternative to the direct I-Q separation technique.

In order to ensure coherency, the superheterodyne LO needed to be equally split and mixed with each LNB's IF output as per Figure 5.1. This was realised using a combination of Wilkinson power dividers and branchline couplers. Furthermore, the IF filters discussed in Chapter 5 were also designed to suppress the image band associated with this superheterodyne network. Thus, should be used in conjunction with this superheterodyne network. A radial stub filter was also designed to isolate the mixer output signal (i.e. the second stage IF signals).

B.1 IN-PHASE AND QUADRATURE SEPARATION OF THE LOCAL OSCILLATOR

The LNBs' IF signals were filtered to isolate only a portion of the spectrum centred at 1.10 GHz. For this implementation, the filtered IF band would be down-converted using an LO centred at 1.5 GHz to produce a second IF centred at 0.4 GHz. The proposed second down-conversion process is shown in Figure B.1.

The choice of LO frequency was supported by the following factors:

- Available Rohde & Schwarz signal generator operates between 1 - 20 GHz.
- Image band (per Figure B.1 between 1.85 - 1.95 GHz is suppressed by both narrowband filters and the image band is well away from the filters' spurious passbands.

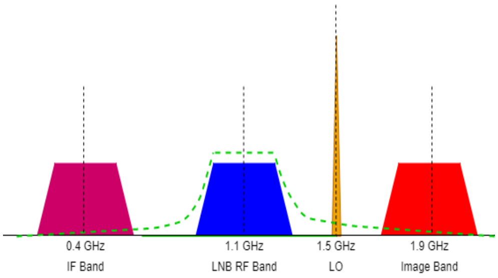

Figure B.1: Proposed down-conversion scheme in which the LO (orange) at 1.5 GHz is mixed with the LNBs' IF band (blue) centred at 1.1 GHz to produce an IF signal (purple) centred at 0.4 GHz. The figure also shows the image band (red) which is attenuated by the IF filter (dotted green lines).

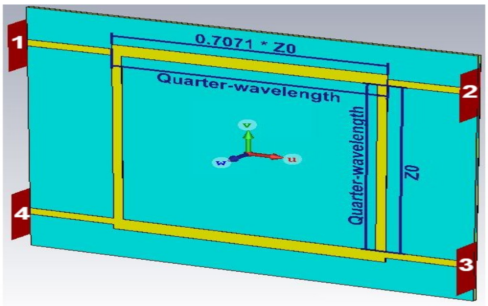

Figure B.2: Simulated branchline coupler required to separate the 1.5 GHz LO into I-Q components

The development of the LO's I-Q network required the use of couplers and dividers. These, along with integrated designs, were all manufactured and the corresponding measured performance is shown in Appendix C.

B.1.1 1.5 GHz Branchline Couplers

Figure 5.1 indicated that the the LO needed to be separated into it I-Q components. This could be accomplished using basic principles such as using a T-junction where one junction output cable is a quarter-wavelength longer than that of the other output. This was feasible as ideally the LO is at a single discrete frequency.

Specific lengths of coaxial cable are needed for the T-junction and the 90° phase shift. Furthermore, this separation needs to be replicated in order for the same LO to be used for both LNBs. In order to ensure the desired amplitude and phase imbalance of the LO, a high degree of precision is required in the cutting of cable lengths (a quarter-wavelength at 1.5 GHz is approximately 50mm). Instead, a microstrip PCB implementation was chosen, which improved modelling and simulation. A suitable solution to this was to use a branchline coupler, as shown in Figure B.2, similar to that discussed in Section 5.4.1.

Suitable commercially available devices include the Mini-Circuits ZX10Q-2-19-S+, which offered features such as a wider bandwidth (0.825 GHz) and a protective casing, however, this is outweighed by the high cost and limitations on importing. This Mini-circuits device served as a benchmark to which the designed branchline coupler was be compared.

Focus was placed on optimising the design to match/ improve on the performance of the Mini-Circuits device previously mentioned, specifically at 1.5 GHz, and to minimise losses. A comparison of the various S-parameters are shown in Figure B.3 and their performance specifically at 1.5 GHz is summarised in Table B.1.

These results indicated that the designed branchline coupler performed as desired at 1.5 GHz with an amplitude imbalance of less than 0.1 dB between the output ports, while precisely meeting the phase imbalance of 90°. At 1.5 GHz, it also provided minimal return loss of 29.42 dB and isolation (between ports 1 and 4) of 30.16 dB.

The Mini-Circuit's component showed minimal amplitude imbalance and an almost linear phase over this band, which justified its use for larger bandwidths. It also provided the desired phase imbalance at 1.5 GHz, however this comes at the trade-off in amplitude imbalance of 0.47 dB. It also achieved a return loss of 26.06 dB and provided superior isolation of 42.52 dB at 1.5 GHz.

Table B.1: Comparison of the amplitude and phase imbalance of the output ports for the designed branchline coupler and Mini-Circuits ZX10Q-2-19-S+. at 1.5 GHz.

	S_{21}		S_{31}		Imbalance	
	Magnitude	Phase	Magnitude	Phase	Magnitude	Phase
Mercurywave Simulation	-3.195 dB	-153.0°	-3.102 dB	-243.0°	0.093 dB	90.0°
Mini-Circuits ZX10Q-2-19-S	-3.115 dB	-109.8°	-3.585 dB	-199.9°	0.470 dB	90.1°

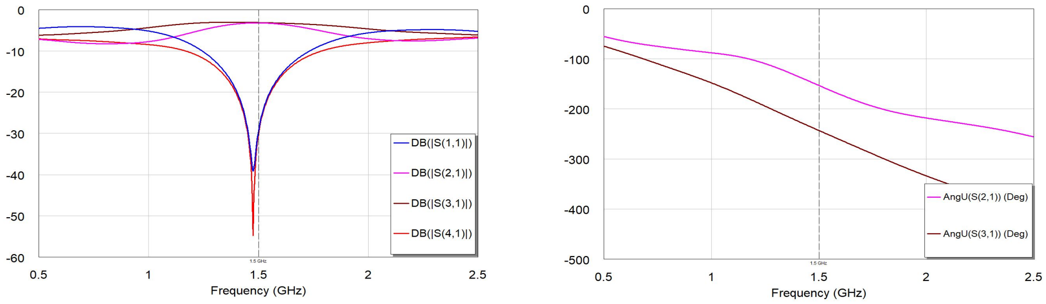

(a) Designed branchline coupler S-parameter magnitudes.

(b) Designed branchline coupler S21 and S31 phases.

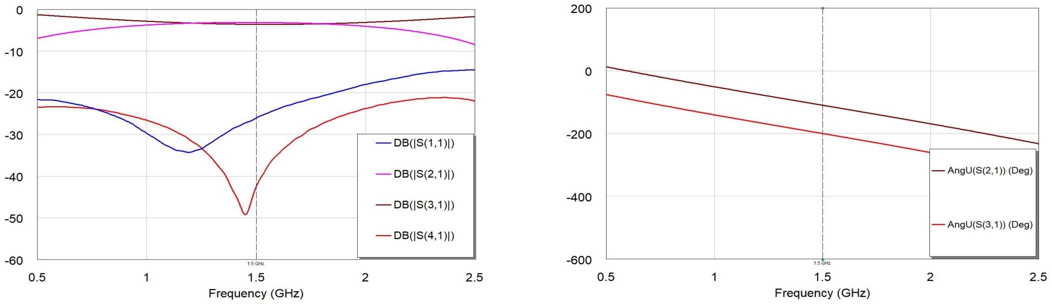

(c) Mini-Circuits ZX10Q-2-19-S+ S-parameter magnitudes.

(d) Mini-Circuits ZX10Q-2-19-S+ S21 and S31 phases.

Figure B.3: Comparison of S-parameter amplitudes and phases of the designed branchline coupler and Mini-Circuits ZX10Q-2-19-S+.

Using the ideal half-power split as a reference, the insertion loss, without factoring in amplitude imbalance, would be the value by how much S_{21} or S_{31} exceeds - 3 dB. Based on this, the simulated branchline coupler showed a maximum insertion loss of 0.195 dB, while the Mini-Circuits component showed an insertion loss of 0.585 dB. These results all indicated that the branchline coupler was a suitable alternative to the Mini-circuits component.

B.1.2 **1.5 GHz Wilkinson Power Divider**

As per Figure 5.1 the LO needed to be split into four parts of equal magnitude i.e. two I-components and two Q-components. The previous section discussed how the LO would be separated into I-Q components, while the focus of this section will be how the LO was separated with equal amplitude and no phase shift.

An equal power split Wilkinson power divider centred at 1.5 GHz was designed and optimised in CST as per Figure B.4. Its performance was also compared to a Mini-Circuits ZAPD-2+ power divider which has a rated operating band of 1 - 2 GHz. Its performance at 1.5 GHz served as a benchmark to which this designed Wilkinson power divider was be compared to.

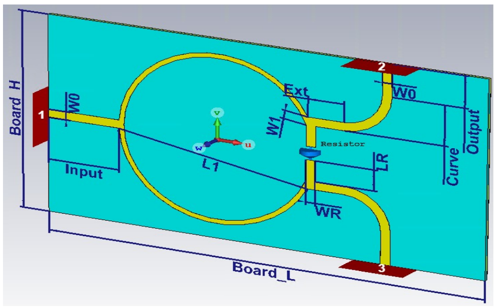

Figure B.4: 1.5 GHz Wilkinson power divider model developed in CST.

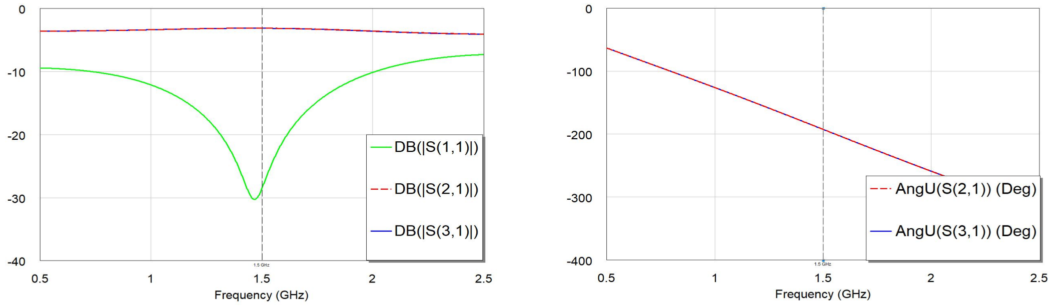

(a) S-parameter amplitudes of the 1.5 GHz Wilkinson power divider

(b) S21 and S31 phases of the 1.5 GHz Wilkinson power divider

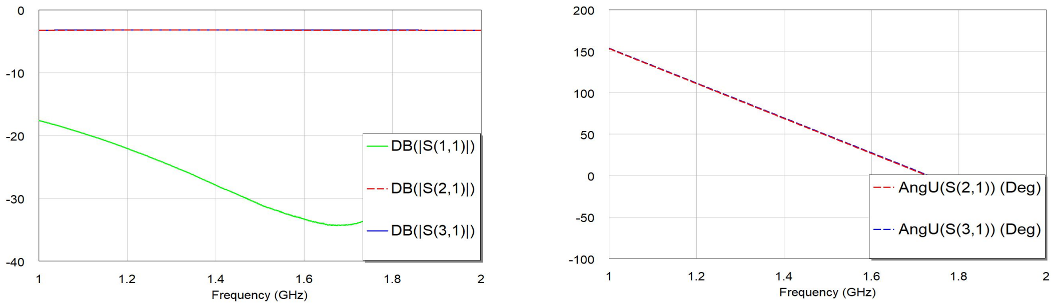

(c) S-parameter amplitudes of the Mini-Circuts power divider

(d) S21 and S31 phases of the Mini-Ciruits power divider

Figure B.5: S-parameter amplitudes and phases of the power dividers, which compares the performance between the Wilkinson power divider model and the alternative Mini-Circuits component.

Initial results showed the desired half-power split between the output ports along with no amplitude nor phase imbalance - this was attributed to the symmetric nature of the design. CST's Trust Region Framework was then used to minimise the frequency shift. This is shown in Figure B.5, which compares the S-parameters of the optimised Wilkinson power dividers to the Mini-Circuits ZAPD-2+ alternative.

As evident in Figure B.5a, the designed Wilkinson power divider showed an appropriate reduction in return-loss near the operating frequency with a return loss of less than than 20 dB. Due to the significantly wider band of operation, the Mini-Circuits ZAPD-2+ was not able to achieve such a low return loss throughout its entire 1 - 2 GHz operating band, but it still outperformed the Wilkinson power divider at 1.5 GHz, as shown in Figure B.5c.

As can be seen from these results, the output ports of the Wilkinson power divider showed the desired performance: equal output amplitude and no phase imbalance. This could be attributed to the symmetric nature of the design. Furthermore, the simulations showed minimal insertion loss, no greater than 0.13 dB (based on the ideal half-power split) at 1.5 GHz. Similar performance was observed for the Mini-Circuits product with a maximum insertion loss of 0.24 dB.

Observing the output port phase in Figures B.5b and B.5d, indicated a linear phase progression over the entire operating band along with 0° phase imbalance between the output ports. Based on these results, it was evident that the designed 1.5 GHz Wilkinson power divider was a suitable alternative to the Mini-Circuits ZAPD-2+.

B.1.3 **Integrated Power Dividers and Couplers**

Similar to designs discussed in Chapter 5, this LO network also integrated multiple designs onto a single PCB. Specifically, the 1.5 GHz branchline coupler and 1.5 GHz Wilkinson power divider were integrated onto a single PCB. In order to better demonstrate the purpose of an integrated solution, Figure B.6 illustrates two possible ways in which the 1.5 GHz LO could be split into I-Q components. Corresponding CST models were developed for both - these are shown in Figure B.7.

Each of these integrated designs offered unique advantages when comparing their physical structures. The model

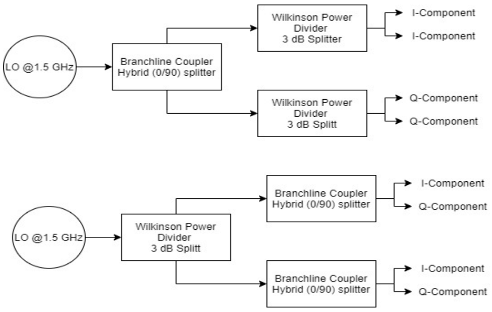

Figure B.6: Two possible methods to separate the 1.5 GHz LO into its I-Q components. The top method first uses a branchline coupler to separate the LO into I-Q components, which is then equally split using two Wilkinson power dividers to produce four outputs: two adjacent I-components and two adjacent Q-components. The second technique instead firsts equally splits the LO using a single Wilkinson power divider followed by two branchline couplers, which provide the I-Q separation. The final outputs consist of two pairs of I-Q components.

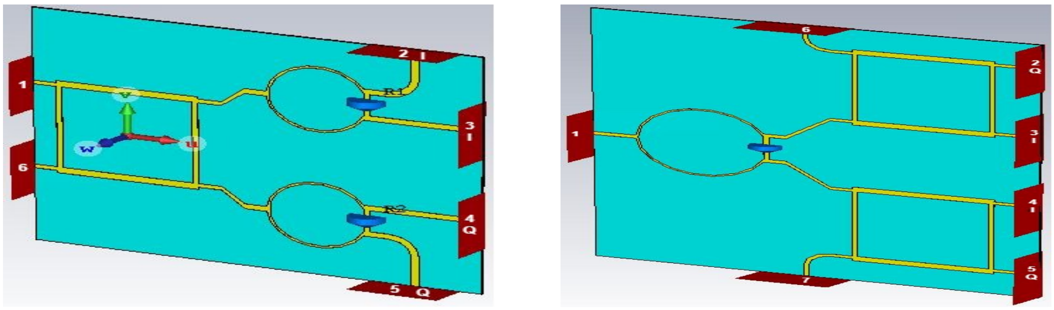

(a) Separation into two adjacent I-components and two adjacent Q-components sets, which is equivalent to the top method in Figure B.6.

(b) Separation into two pairs of I-Q components, which is equivalent to the bottom method in Figure B.6.

Figure B.7: Equivalent CST models of the I-Q separation network shown in Figure B.6 required to separate the 1.5 GHz LO. The various port numbers and the phase of the output ports relative to one another are also indicated.

presented in Figure B.7a comprised of a single branchline coupler along with two Wilkinson power dividers. This resulted in an overall PCB layout with six ports, which was less than that of Figure B.7b, which made use of a single Wilkinson power dividers along with two branchline couplers to produce a seven port PCB. As discussed in section B.1.1, the branchline coupler included an isolation port; thus, the latter model's additional port was attributed to the additional branchline coupler. Furthermore, the former model was physically smaller than the latter - this was again attributed to branchline couplers occupying more board space than Wilkinson power dividers.

The latter model still had more desirable features, regardless of this larger PCB size. The PCB layout provided pairs of LO I-Q components, which would reduce interlacing physical cables when connecting the the PCBs to the superheterodyne mixers. Another important consideration was the spacing between output ports. No modifications to the standard branchline coupler were needed to accommodate the SMA connectors in the integrated design, as the output ports were separated by approximately a quarter-wavelength. This was not the case for the former option (Figure B.7a). The Wilkinson power divider outputs were modified (curved) to accommodate the SMA connectors. This resulted in unwanted phase imbalance which was evident in the simulated performance.

For the case of the integrated designs, the ideal (excluding any losses) output magnitude at each port was -6.02 dB (25%) - this was due to splitting of a single input signal among four output ports. CST's optimiser tool was used to refine the performance of each of these integrated designs at 1.5 GHz, however, it provided limited improvement due to the design restrictions previously discussed along with the vast number of parameters now involved. The final optimised results are shown in Figure B.8.

These results indicated that the intended performance was still obtained when merging two structures with one another. In approaching 1.5 GHz, there was noticeable reduction in return loss, unifying of S-parameter magni-

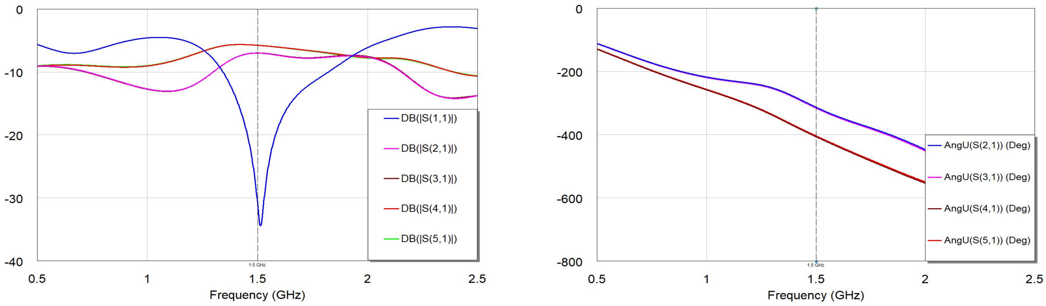

(a) S-parameter amplitude of the integrated branchline-Wilkinson power divider shown in Figure B.7a.

(b) Output S-parameter phases of the integrated branchline-Wilkinson power divider shown in Figure B.7a.

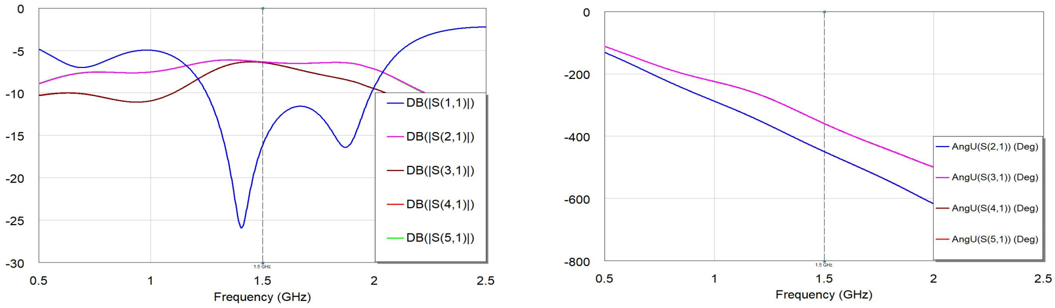

(c) S-parameter amplitude of the integrated Wilkinson-branchline power divider shown in Figure B.7b.

(d) Output S-parameter phases of the integrated Wilkinson-branchline power divider shown in Figure B.7b.

Figure B.8: S-parameter amplitudes and phases of the integrated I-Q network comparing the performance of the models shown in Figure B.7.

tude for S_{21}-S_{51}, and a linear phase response. However, upon closer inspection of these results, there were subtle differences in performance between the two integrated designs. This is better depicted in Table B.2 and Table B.3, which compares the amplitudes and phases, respectively, of each of the output ports specifically at 1.5 GHz. These further highlight pairs of I-outputs and pairs of Q-outputs.

With specific reference to the branchline-Wilkinson power divider in Figure B.7a, its results in Figure B.8a showed a rapid decline in return loss, reaching 30.87 dB at 1.5 GHz. The amplitude of ports 2 and 3 (I-components) were approximately - 7.00 dB indicating 1 dB insertion loss, however port 4 and 5 (Q-components) were approximately -5.76 dB. The maximum at any output port should be less than -6.02 dB (since the input signal was split among four outputs). Therefore, this result indicated that there was a power imbalance among output ports (less than 1.24 dB since part of this was also due to insertion loss).

In observing the output phases at 1.5 GHz, the I-outputs differed by 2.6°, while the Q-outputs differed by 2.5°. The largest phase imbalance between a set of I-Q components was 93.2° - this was an unwanted 3.2° phase deviation from the target 90°. This may be attributed to the design changes made to the output ports (such as port-pairs 2-3 or 4-5 in Figure B.7a), in which one output port (3 or 4) was inline with the Wilkinson power divider, while the other paired output port (2 or 5) curved away from the Wilkinson power divider. This curved output design was

Table B.2: Comparison of the amplitude balance for the integrated I-Q network structures at 1.5 GHz. Grey highlighted cells are pairs of I-outputs while unhighlighted cells are pairs of Q-outputs as per Figure B.7.

	S_{21}	S_{31}	S_{41}	S_{51}	Imbalance
Branchline-Wilkinson (Figure B.7a)	-7.00 dB	-6.98 dB	-5.76 dB	-5.76 dB	1.24 dB
Wilkinson-Branchline (Figure B.7b)	-6.34 dB	-6.41 dB	-6.41 dB	-6.34 dB	0.07 dB

Table B.3: Comparison of the phase imbalance of the integrated I-Q network structures at 1.5 GHz. Grey highlighted cells are pairs of I-outputs while unhighlighted cells are pairs of Q-outputs as per Figure B.7.

	S_{21}	S_{31}	S_{41}	S_{51}	Imbalance
Branchline-Wilkinson (Figure B.7a)	-312.9°	-315.5°	-406.1°	-403.6°	93.2°
Wilkinson-Branchline (Figure B.7b)	-449.1°	-359.2°	-358.9°	-448.9°	90.2°

necessary to ensure that SMA connectors could be mounted onto the boards, however, this was at the expense of an increased phase imbalance.

The alternative solution would be the Wilkinson-branchline power divider shown in Figure B.7b. As previously mentioned, no modifications to the output ports were necessary in this design since the standard branchline coupler outputs were spaced a quarter-wavelength apart - the corresponding results are shown in Figures B.8c and B.8d. These results showed a decrease in return loss to 16.2 dB at 1.5GHz. While the previous branchline-Wilkinson power divider achieved a superior, smoother return loss, this Wilkinson-branchline power divider traded a poorer return loss (while still adequate) for an improved performance in other areas. Table B.1 showed improved amplitude balance among all four output ports, with a maximum variation of 0.07 dB. Using the benchmark of -6.02 dB for equal power splitting among 4 ports, these results also indicated an insertion loss less than 0.39 dB. Furthermore, the maximum phase imbalance of 90.2° between outputs indicated only a 0.2° deviation from the desired phase imbalance.

This Wilkinson-branchline power divider outperformed the branchline-Wilkinson power divider in terms of amplitude and phase imbalance. It also showed fewer losses at 1.5 GHz. The expense of this was a larger PCB and the need for an additional isolation port. It is also to be noted that this branchline-Wilkinson power divider outperformed the previously designed standard branchline coupler and Mini-circuits equivalent in both amplitude and phase imbalance.

B.2 Low-pass Filter

Typically a second bandpass filter is placed after the down-converting mixer. This is generally done to isolate the desired band, while removing spurious signals, such as the upper sideband and higher-order mixer products. Implementing a microstrip bandpass filter centred at 0.4 GHz would be challenging largely due to the overall size. Third-order stub filters such as those previously discussed would occupy a PCB space in excess of 350 mm x 220 mm, which would be extremely costly, while the hairpin filter would require minute spacing that would not meet the minimum fabrication specifications. Due to these complications, a decision was made to instead make use of a low-pass filter. After the down-conversion network, the desired lower sideband would be between 0.35 GHz - 0.45 GHz, while the upper sideband would be between 2.55 GHz - 2.65 GHz. Furthermore, the lowest third order mixer product would be present at 0.80 GHz. A third-order, single radial stub, low-pass filter was chosen with a cut-off frequency of 0.6 GHz. The AWR iFilter Filter Synthesis tool was used to determine the initial parameters to be used in the CST model, as shown in Figure B.9.

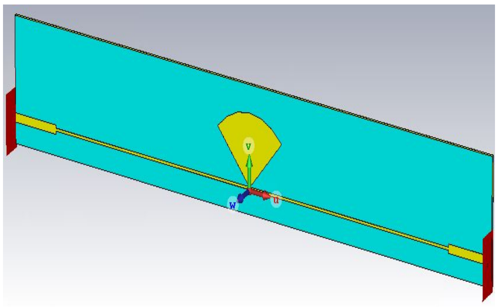

Figure B.9: CST model of the third-order, single stub low-pass filter.

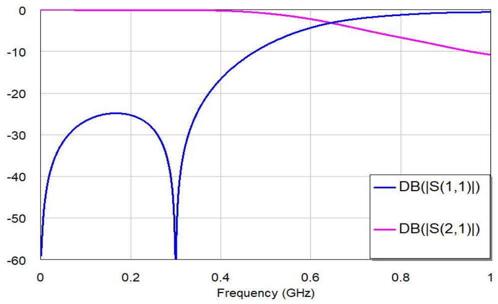

Figure B.10: Simulated S-parameters of the third-order single stub low-pass filter shown in Figure B.9.

The simulated performance shown in Figure B.10 showed adequate performance in return loss which remained below 10 dB up to 0.477 GHz and increases to 1.231 dB at 0.8 GHz. Furthermore, there was minimal insertion loss throughout the 0.35 GHz - 0.45 GHz IF band, which remained below 0.5 dB. The cut-off frequency based on when S_{21} fell below -3 dB was 0.638 GHz, which was slightly higher than specification, however would still suppress the third-order mixer product.

APPENDIX C

PCB MEASUREMENTS SUPERHETERODYNE NETWORK

This chapter presents the manufactured PCBs and measured results of the superheterodyne network discussed in Appendix B.

C.1 MANUFACTURED 1.5 GHZ BRANCHLINE COUPLERS

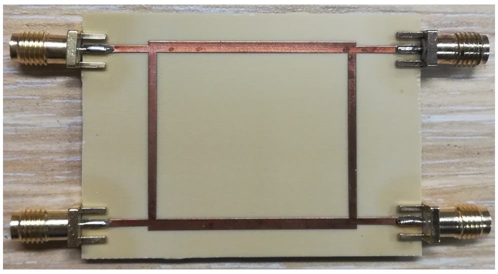

(a) Manufactured 1.5 GHz Branchline Coupler.

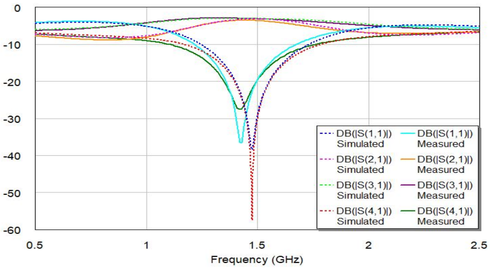

(b) Comparison of the S-parameter amplitudes between the simulated and measured 1.5 GHz branchline coupler.

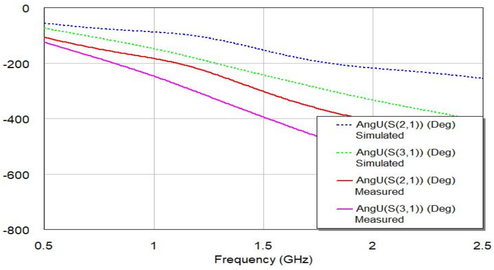

(c) Comparison of the output port phases between the simulated and measured 1.5 GHz branchline coupler.

C.2 MANUFACTURED 1.5 GHZ WILKINSON POWER DIVIDER

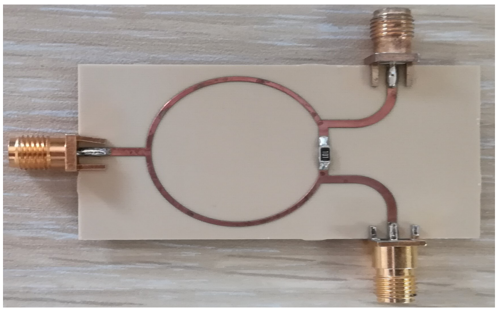

(a) Manufactured 1.5 GHz Wilkinson Power Divider.

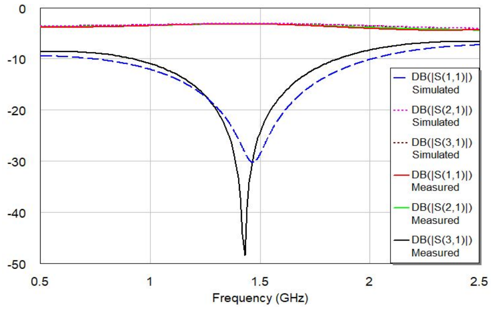

(b) Comparison of the S-parameter amplitudes between the simulated and measured 1.5 GHz Wilkinson Power Divider.

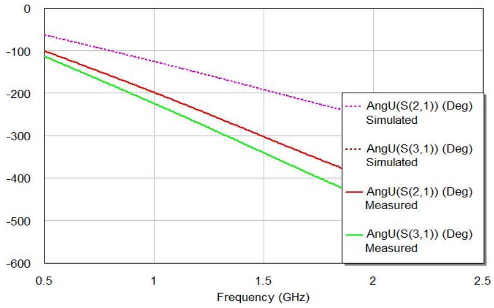

(c) Comparison of the output port phases between the simulated and measured 1.5 GHz Wilkinson Power Divider.

C.3 INTEGRATED 1.5 GHZ WILKINSON POWER DIVIDERS AND BRANCHLINE COUPLERS

Branchline-Wilkinson Power Divider

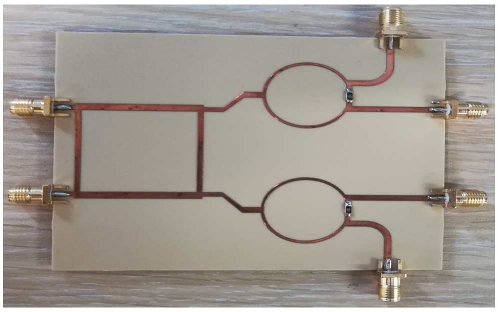

(a) Manufactured 1.5 GHz Branchline-Wilkinson Power Divider.

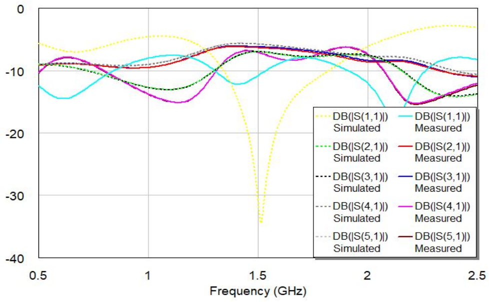

(b) Comparison of the S-parameter amplitudes between the simulated and measured 1.5 GHz Branchline-Wilkinson Power Divider.

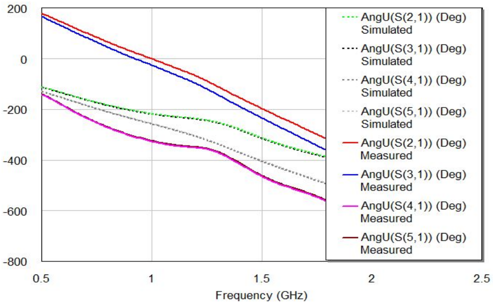

(c) Comparison of the output port phases between the simulated and measured 1.5 GHz Branchline-Wilkinson Power Divider.

Wilkinson-Branchline Power Divider

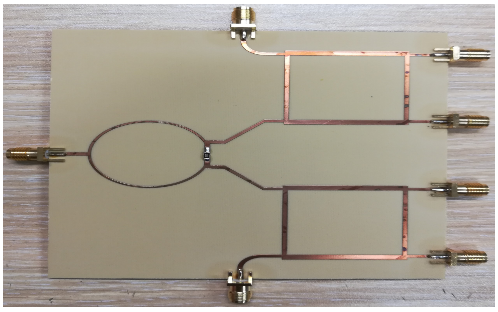

(a) Manufactured 1.5 GHz Wilkinson-Branchline Power Divider.

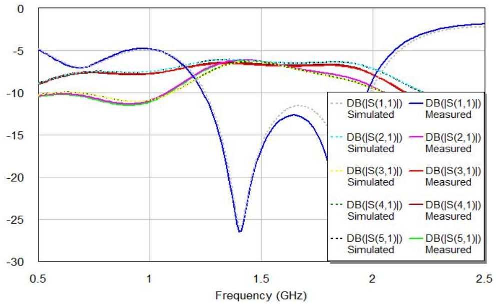

(b) Comparison of the S-parameter amplitudes between the simulated and measured 1.5 GHz Wilkinson-Branchline Power Divider.

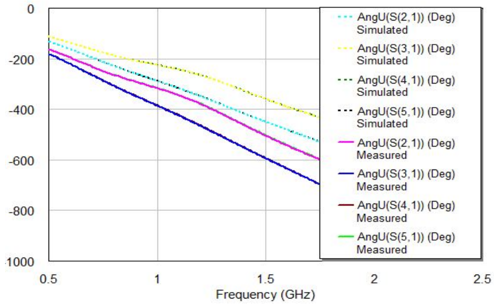

(c) Comparison of the output port phases between the simulated and measured 1.5 GHz Wilkinson-Branchline Power Divider.

C.4 LOW-PASS FILTER

(a) Manufactured low-pass filter.

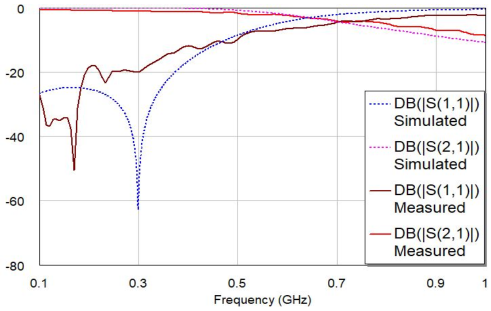

(b) S-parameter comparison between the simulated and measured low-pass filter.